Fabrication of wavy type porous triple-layer SC-SOFC via in-situ observation of curvature evolution during co-sintering

by

Indae Choi

Doctoral Thesis

Submitted in partial fulfilment of the requirements for the award of Doctor of Philosophy of Loughborough University

School of Aeronautical, Automotive, Chemical and Materials
Engineering
Loughborough University
UK

February 2015

Abstract

Wavy type Single Chamber Solid Oxide Fuel Cells (SC-SOFCs) have been shown to be conducive to improving the effective electrochemical reaction area contributing to higher performance, compared with planar type SC-SOFCs of the same diameter. This study presents a fabrication process for wavy type SC-SOFCs with a single fabrication step via co-sintering of a triple-layer structure. The monitoring and observation of the curvature evolution of bi- and triple-layer structures during co-sintering has resulted in an improved process with reduced manufacturing time and effort, as regards the co-sintering process for multi-layer structures. Investigation using in-situ monitoring helps different shrinkage behaviours of each porous layer to minimise mismatched stresses along with avoidance of severe warping and cracking. In the co-sintering of the multi-layer structures, the induced in-plane stresses contribute to curvature evolution in the structure, which can be utilised in the design of a curved multi-layer structure via the co-sintering process.

For intermediate temperature SOFCs, the materials used are NiO/CGO for anode; CGO for electrolyte; and LSCF for cathode. These materials are tape-casted with 20µm thickness and assembled for bi- and triple-layer structures by hot pressing. Sintering mismatch stresses have been analysed in bi-layer structures, consisting of NiO/CGO-CGO and CGO-LSCF. The maximum sintering mismatch stress was calculated at interface of bi-layer structure in the top layer. In order to achieve the desired wavy type triple-layer structure, flexible green layers of each component were stacked up and laid on alumina rods to support the curvature during the process. In-situ observation, to monitor the shrinkage of each material and the curvature evolution of the structures, was performed using a long focus microscope (Infinity K-2). With these values, the main factors such as viscosity, shrinkage rate of each material, and curvature rate are investigated to determine the sintering mismatch stresses. This enables the prediction of curvature for triple-layer structure and the prediction is validated by in-situ monitoring of the triple-layer structure co-sintering process. Zero-deflection condition is confirmed to

maintain initial shape during co-sintering and helps to minimise the development of undesired curvature in the triple-layer structure.

Performance testing of the wavy cell was carried out in a methane-air mixture ($CH_4:O_2$ =1:1). In comparison with a planar SC-SOFC, it showed higher OCV which might be attributed to not only macro deformation, but also microstructural distribution affecting the effective gas diffusion paths and electrochemical active sites.

Publications

1. Indae Choi, Manoj Ranaweera, Jung-Sik Kim, "Fabrication and evaluation of a novel wavy Single Chamber-Solid Oxide Fuel Cell via in-situ monitoring of curvature evolution", Journal of Power Sources, 2015 (Pending)

2. Indae Choi, Manoj Ranaweera, Jung-Sik Kim, "Fabrication of Three-Dimensional Wavy Single Chamber Solid Oxide Fuel Cell by In Situ Observation of Curvature Evolution", Int. J. Applied Ceramic Tech., 2015, in-press

3. Indae Choi, Manoj Ranaweera, Jung-Sik Kim, "Experimental observations of the co-sintering of porous triple-layer SOFCs including curvature evolution," Sintering 2014 conference, Dresden, Germany, Aug. 2014 (Poster presentation - 1st Place Poster Award)

4. Indae Choi, Jung-Sik Kim, "Fabrication of wavy type porous triple-layer SC-SOFCs via in-situ observation of curvature evolution during co-sintering," 10th International Hydrogen & Fuel Cell conference, Millennium Point in Birmingham (UK), Mar. 2014 (Oral presentation)

5. Indae Choi, Jung-Sik Kim, "In-situ investigation of curvature change induced by stress in multilayer structure during co-sintering for wavy type SOFC," Hydrogen & Fuel cell SUPERGEN conference, Birmingham University (UK), Dec. 2013 (Oral presentation)

Acknowledgements

I would like to extend my gratitude to all individuals and institutions that in various ways and capacities enabled me to pursue and complete this research work. Foremost among them, I would like to express my utmost gratitude to my supervisor, Dr. Jung-Sik Kim. With his invaluable guidance and support, I was able to engage in a broad range of research to complement the work that I performed for this dissertation. Cordial advice and continuous encouragement spurred me to think outside of the box in order to solve various technical issues that I encountered while conducting my research. I also thank him for being so kind to me and making a friendlier and comfortable environment during this entire period.

I would like to express my sincere gratitude to my co-supervisor, Dr. Andrew Watson for teaching me to develop my finite element analysis (FEA) in the early stage of the research, which helped me to predict the experimental results. He encouraged and supported me with much kindness throughout this research.

I would make this opportunity to thank my colleagues, Mr. Manoj Ranaweera, Mr. Vijay Venkatesan, and Mr. Erdogan Guk for their support and immense assistance given me in setting up the data acquisition systems and conducting the experiments. Dr. Anusha Wijewardane should specially be thanked for sharing her experiences to set up experimental equipment and giving me valuable comments during my first year. I would like to acknowledge the rest of the graduate students who worked in our research group over the year and who enriched my research and social environment.

I am very grateful for the assistance provided by all the technical staff of the Aeronautical and Automotive Engineering Department who helped me with my research. In particular, Mr. David Travis, Mr. John Cunningham, Mr. Pradip Karia, and Mr. Harshad Purohit for helping me to construct the test rigs, and Ms. Anne Matthews for her assistance with purchasing the test equipment.

I extend my gratitude to my father, mother and sister for their unfailing support of my endeavours, which motivated me to do my best all the time. They

have always shown concern about my well-being and my studies, even while they halfway around the world.

I am deeply indebted to my loved wife Mrs. Minyoung Jang and my little girl Ms. Olivia Choi for helping me in emotionally during this entire time. I feel very fortunate to have a considerable and a loving wife like her, who is always there for me, tolerating with me whenever I am stressed.

Finally, I would like to thank everyone who helped me to the successful realisation of this thesis, and I express my apology as I could not mention them all by names.

Table of Contents

Nomenclature

Latin letters

A	Constant
b	Burger's vector
D	Diffusion coefficient
d	Grain size
E	Yong's modulus
G	Shear modulus
g	Gravity
j	Isotropic parameter
K	Bulk modulus
k	Boltzmann's constant
L, l	Length
m	Thickness ratio
n	Stress component, Viscosity ratio
p	Exponent of the inverse grain size
Q	Activation Energy
R	Gas constant
R_{mix}	Mixture ratio
T	Absolute temperature
V	Volume
w	Width

Greek symbols

α	Plate modulus
Δ	Difference
ε	Strain
$\dot{\varepsilon}$	Strain rate

η	Uniaxial viscosity
κ	Curvature
ν	Poisson's ratio
ρ	Density, Radius of curvature
Σ	Sintering potential
σ	Stress

Subscripts and superscripts

c	Creep
f	Free sintering
i	Initial state
max	Maximum
p	Viscous state
s	Sample
t	Specific time
th	Theoretical condition
v	Vertical sintering
x	X-axis direction
y	Y-axis direction
z	Z-axis direction

Abbreviations

Au	Gold
BSCF	Barium Strontium Cobalt Ferrite
Ce	Cerium
CGO (GDC)	Gadolinium-Doped Ceria
DC-SOFC	Dual Chamber Solid Oxide Fuel Cell
LSC	Lanthanum Strontium Cobalt Oxide
LSCF	Lanthanum Strontium Cobalt Ferrite

LSCM	Lanthanum Strontium Manganese Chromite
LSGM	Strontium and Magnesium-doped Lanthanum Gallate
LSM	Lanthanum Strontium Manganite
LTCC	Low Temperature Co-fired Ceramic
Ni-YSZ	Nickel - Yttria Stabilized Zirconia
OCV	Open Circuit Voltage
Pd	Palladium
Pt	Platinum
TD	Theoretical Density
Ru	Ruthenium
SC-SOFC	Single Chamber Solid Oxide Fuel Cell
SDC	Samaria doped Ceria
SEM	Scanning Electron Microscope
SOFCs	Solid Oxide Fuel Cells
SSC	Strontium-doped Samarium Cobaltite
TEC	Thermal Expansion Coefficient
TPB	Triple Phase Boundary
XRD	X Ray Diffraction
YSZ	Yttria Stabilized Zirconia

List of Figures

List of Tables

Chapter 1

Introduction

1.1 Significance of Research

Solid Oxide Fuel Cells (SOFCs) have received much attention as a next-generation alternative energy device. SOFCs offer the advantages of highly efficient and non-polluting electricity generation. In recent years, rapid progress has been made on fabrication methods, materials and applications of SOFCs, such as sensors and secondary energy systems [1-6]. Their high operating temperature generates various problems regarding reliability and stability in long-term operation. Much research has recently been devoted to investigating the possibility of lowering the operation temperature range. Doing so would result in a scaling down of fuel cell systems, due to lack of auxiliaries, as well as a reduction of SOFCs fabrication costs by the use of cost effective structures [7-11]. In spite of these efforts, many of the problems remain unaddressed. This is particularly the case pertaining to the issues of mechanical and thermal stresses, which can be mainly attributed to the mismatch in thermal expansion coefficients (TEC) between each layer with respect to other layers/components, inducing a low level performance of and a decrease in stability of fuel cell systems [12]. Although complicated fabrication processes with multi-composition mixtures can be applied both to improve cell performance and to enhance electrical and mechanical properties, these may be time-consuming and costly [13].

The composition of SOFCs generally consists of three layers: anode, electrolyte and cathode layers. The electrolyte materials used in SOFCs tend to become active ionically and non-active electronically at their operating temperatures, from 500°C to 1000°C. During cell operation, oxygen gas converts into oxygen ions at the cathode. These ions then diffuse through a

solid electrolyte to the anode, where the reaction between the diffused oxygen ions and the supplied hydrogen takes place to produce water as well as heat and electricity. In this reaction, vacant oxygen lattice sites in the electrolyte layer act as charge carriers. At the anode layer which the oxidation of the fuel occurs, hydrogen and oxygen ions ($O_o{}^x$) are converted into H_2O, oxygen vacancies ($V_o{}^{\bullet\bullet}$) and electrons (e^-), given by:

$$H_2 + O_o{}^x \rightarrow H_2O + V_o{}^{\bullet\bullet} + 2e^- \tag{1.1}$$
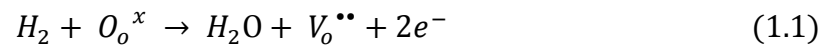
The reduction of oxygen occurs at the cathode layer, consuming the electrons which come through an external circuit from the anode. By the immigration of oxygen from the gas phase at the cathode, oxygen vacancies are removed consuming a pair of electrons, which leads to the formation of oxygen ions.

$$\frac{1}{2}O_2 + 2e^- + V_o{}^{\bullet\bullet} \rightarrow O_o{}^x \tag{1.2}$$

From the sum of reaction (1.1) at the anode and (1.2) at the cathode in Figure 1.1, the fundamental reaction process for energy conversion can be confirmed showing hydrogen reaction with water as the product:

$$H_2 + \frac{1}{2}O_2 \rightarrow H_2O \tag{1.3}$$
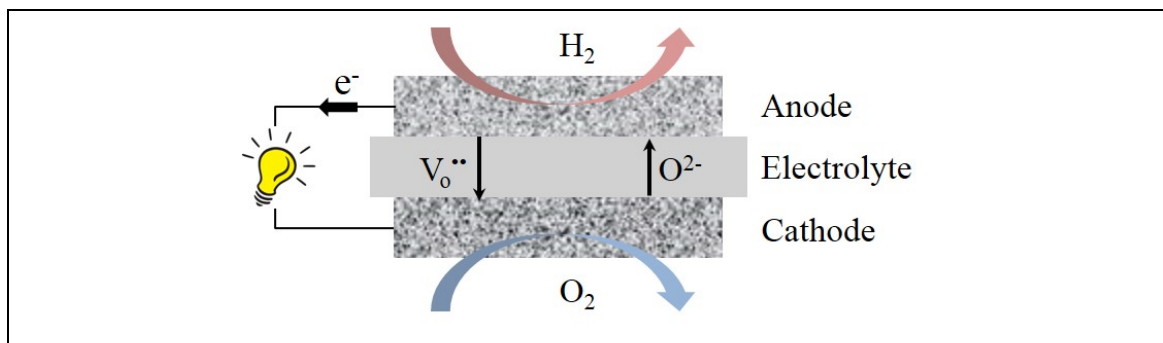
Figure 1.1 Scheme of a SOFC operated H_2 and O_2

Structural types of SOFCs can principally be divided into Dual Chamber SOFCs (DC-SOFCs) and Single Chamber SOFCs (SC-SOFCs), as shown in Figure 1.2. In DC-SOFCs, fuel gas and air have to be supplied to the respective electrodes through two separate chamber inlet pipes (or tubes) so as to prevent two reactant gases from mixing together during operation [14]. The necessity for separation of gas supplies leads to complex manifolds, followed by complicate stack assembly process. Complicated structures restrict possibilities of downsizing of the cell; in addition, they could incur stacking complications and may pose serious constraints on manufacturing methods and choice of materials. Figure 1.3 (a) shows a planar type DC-SOFC, whereby the components of a single planar cell assembly (consisting of anode, electrolyte and cathode layers) are located between two interconnectors, and repeatedly stacked for the requisite levels of power and performance. An alternative to the planar structure is the tubular type DC-SOFC, shown in Figure 1.3 (b). This type of cell is created by fabricating a hollow tubular structure for the anode, which is then consequently coated with electrolyte and cathode layers.
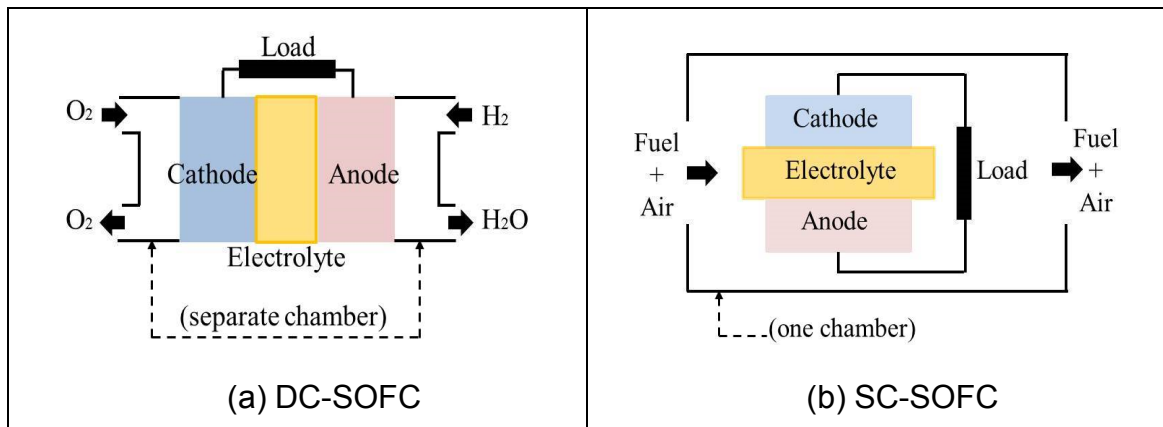
Figure 1.2 Compositions of (a) DC-SOFC and (b) SC-SOFC

SC-SOFCs consist of only one gas chamber, wherein the anode and cathode layer will react with the gas mixture at the same time [15-17]. This simplified design, shown in Figure 1.2(b), offers the possibility to reduce stack components, removing the need for gas tight sealing that is a difficult problem for DC-SOFCs during their operations. In addition, SC-SOFCs permit greater variations in geometry types that preclude conventional fuel cell designs, which are limited to planar and tubular structures. Although SC-SOFCs have plenty of

economic advantages, such as simpler structures and assembly, with no separation of gas supply, and various geometries, the performance of the cell is known to be significantly lower relative to that of DC-SOFCs. Contrary to the DC-SOFCs, the nature of SC-SOFC means that the gas mixture flows through the whole structure, which in turn imposes difficulty in simultaneously achieving high performance and cell stability [18].

In order to improve performance of SC-SOFCs, it is essential to increase the length of the triple phase boundary (TPB), where the electrochemical reaction occurs. As the reaction takes place where electrolyte, electrode and gas phase at TPB, this research focuses on fabrication of wavy type SC-SOFCs using co-sintering in which the electrolyte and two electrodes are sintered during the same heat treatment, contributing to enhancement of the effective electrochemical reaction area in the unit chamber diameter for improved performance as compared to that of planar SC-SOFCs. Some researchers suggested the use of porous electrolyte layer to take advantage of both the gas flow and electrochemical performance of the cell [19, 20]. The results indicated that a porous ion-conducting membrane provides sufficient separation of oxygen activity at the electrodes by selection of optimum operation temperature and gas flow rate. Thereby, SC-SOFCs with a porous electrolyte structure provide opportunities to design thermally and mechanically more robust stacks by utilizing hydrocarbon fuels. It also allows for processing the cells at lower temperatures using conventional processing techniques.

| (a) Planar type | (b) Tubular type |
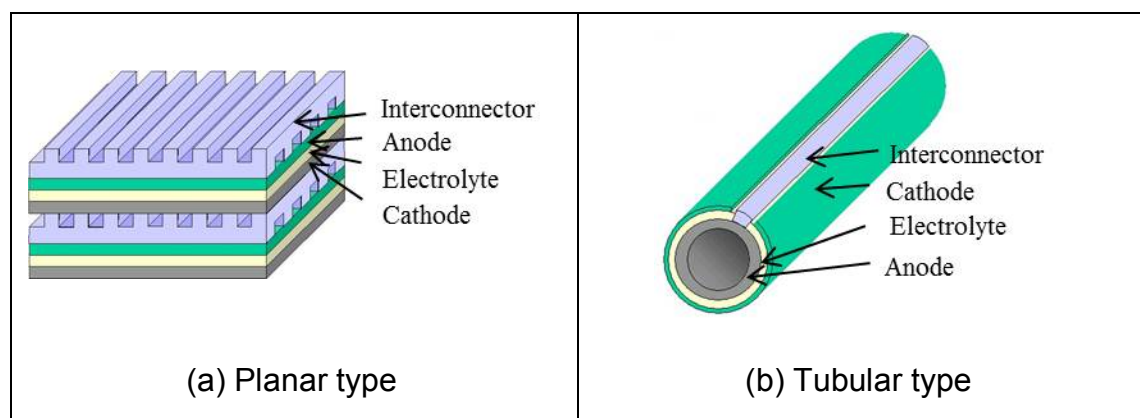
Figure 1.3 Type of DC-SOFCs: (a) planar type and (b) tubular type [21, 22]

1.2 Motivation and Goals

The goal of this work is to develop a novel design and fabrication method for wavy type SC-SOFCs. It is to be achieved by in-situ monitoring of curvature evolution derived from different sintering behaviours of layers during the co-sintering of the multilayer structure. In order to safely apply the SOFCs to portable/subsidiary devices, it is necessary not only to fabricate small structures with higher performance, but also to reduce operating temperatures. For this purpose, the use of mixture gas in SC-SOFCs allows for a simple system without complex manifolds and curved-shape influences to enlarge the effective electrochemical reaction area. This contributes to higher performance as compared to planar types in the unit diameter terms. In addition, materials for intermediate temperature operation should help to improve cell stability during long-term operation.

Another goal of this research is to investigate, via in-situ experimental observation, curvature evolution of the multilayer structure during co-sintering. Although the co-sintering process contributes to saving time and effort in the fabrication of the cell, curvature evolution induced by the mismatch of sintering behaviours in a multi-layer structure causes physical problems, like cracks or delamination. Generally, conventional fabrication allows the co-sintering of bi-layer structures consisting of the anode and electrolyte layer, so as to avoid any defects during the process [23, 24]. In the co-sintering of multi-layer structures, different shrinkage behaviour between layers is significant in determining curvature evolutions. In the co-sintering of multi-layer structures for planar type SOFCs, a loading plate was applied on the multi-layer structure during co-sintering to prevent the structure from developing undesired curvatures [25]. This method presents difficulties in practically figuring out the necessary weight in order to complete a crack-free sintering process. The weight is a dependant factor for the viscosity of the sintering material, and the viscosity is function of the sintering temperature profile where the sintering temperature profile is a function of time. Therefore the adequate weight for the suppressing method for effective crack-free co-sintering is not fixed, but varies throughout the sintering process. Hence, determining the correct weight is not a straightforward method, but often requires a number of iterative trials. Some researchers have used in-

situ curvature analysis using a profilometer or an optical dilatometer, so as to find the level of curvature evolution during co-sintering [26, 27]. In this study, the adjustment of particle size along with in-situ observation was applied to harmonise sintering behaviours between layers and reduce undesired curvatures at the final stage of the co-sintering process. A cathode material having larger particles was expected to increase sintering temperature, closer to the sintering temperature of the anode and electrolyte material. To allow the co-sintering of the triple-layer structure in a zero-deflection condition without a loading plate, in-situ monitoring can be used to analyse the deformation of the structure during the process. In addition, 3D deformation process from initially flat laminated structure is investigated to obtain a wavy structure finally. The results help to confirm the efficacy of the process and contribute to a successful fabrication process for a wavy structure to be achieved.
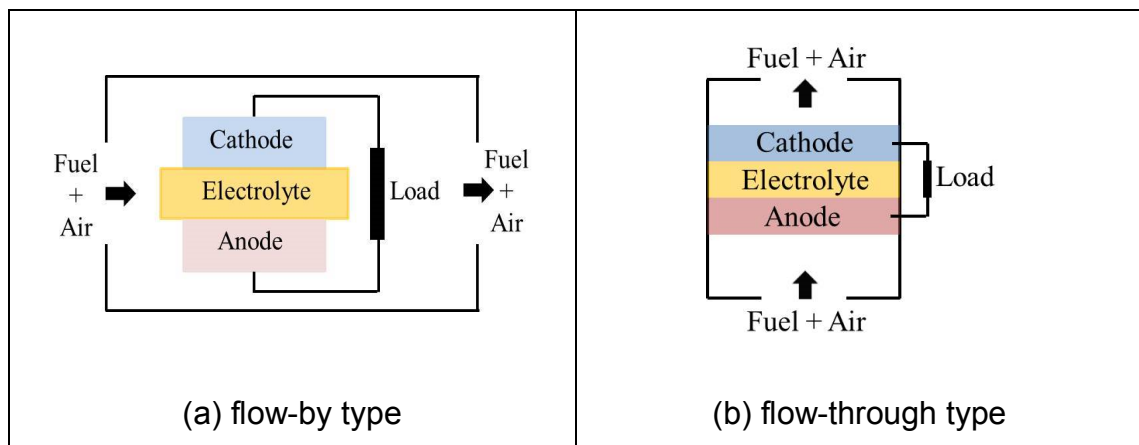
Figure 1.4 Type of SC-SOFC: (a) flow-by type and (b) flow-through type

The SC-SOFCs are commonly classified by gas flow direction, as flow-by type, Figure 1.4 (a), and flow-through type, Figure 1.4 (b). This research is concerned with the flow-through type SC-SOFC, in which the gas mixture can penetrate each layer. This is because the whole layer of the cell consists of a porous structure that can play the role of gas path as shown in Figure 1.4 (b) [28, 29]. As the gas mixture flows through the cell layers, fuel gas reacts in the anode layer for an oxidation process, while oxygen gas from the air reacts in the cathode layer for a reduction process. Through this, it is expected to enhance fuel utilisation rates and reduce mass transport loss, hence achieving better performance over the flow-by type SC-SOFC [30]. Furthermore, the

elongated effective electrochemical reaction area of the wavy type SC-SOFC is expected to help advancing the sum of total electrochemical reactions, hence delivering higher output.

Regarding the fabrication method for curved structures, a tape-casting method has been employed to prepare green layers, due to its advantage of being easy to produce each layer with variable thicknesses. The tape-casted layers are then piled up and being hot pressed in order to form multi-layer structure. The hot pressed structures are used for the SC-SOFC fabrications and related sintering research.

In-situ monitoring helps to capture the curvature deformation of the structure derived from internal stress between materials, and a zero-deflection[1] condition can be discovered so as to be applicable for fabrication of wavy type SC-SOFC. As the manufacturing process of this study suggests a simpler and easier method than the conventional method, it is expected to achieve a reduction in fabrication cost, production time, and energy consumption, along with higher performance of the SC-SOFC. The wavy structure has a larger effective electrochemical reaction area than a planar structure, as compared to the planar type for the same chamber cross sectional area [31]. Higher electrochemical reaction area in the same diameter contributes to enhanced conversion capacity, and so improves the fuel utilisation, which possibly leads to a higher cell performance [32].

---

[1] A zero-deflection condition in this study is defined as the sintering condition that retains the initial green body's shape upon completion of the sintering process. The shape might change during the process, but will restore the initial shape by the time the process finishes.

1.3 Research Objectives

The objectives of this research are firstly to investigate the sintering properties of the materials selected to fabricate a wavy SC-SOFC that will be operated in the intermediate temperature region, i.e. 500°C ~ 600°C.

The strategy applied in the present study is to measure the shrinkage rate and the uniaxial viscosity of the specimens by monitoring the resulting curvature development of the sintering layers. Therefore it is necessary to establish the free sintering and vertical sintering using single layer specimens. Prepared specimens are being sintered under free shrinkage conditions or under vertical shrinkage conditions in order to measure shrinkage and shrinkage rates along with their densities. These results are used for calculation of the uniaxial viscosities from difference of shrinkage rate between free and vertical sintering. Secondly, the curvature evolutions of the multilayer structure are observed via the in-situ observation system, where conclusions are drawn based on differing sintering behaviour of different materials during co-sintering. Based on the materials' uniaxial viscosity and curvature evolution monitoring result, particularly monitoring of the bi-layer structures, curvature evolution of a triple-layer structure is predicted. The predicted curvatures are then compared with measured curvatures from the experimental observations. A zero-deflection sintering condition is determined through in-situ curvature monitoring of the bi- and triple-layer structures plus the dedicated analysis of the curvature evolution patterns from them. The zero-deflection sintering condition is then applied for a fabrication of a wavy triple-layer structure. A specific wavy shape sintering condition is that the planar triple-layer structure is placed on pre-arranged supporters that will help shaping the structure into a wavy shape during a debinding process, after which the wavy formed structure will be sintering via the zero-deflection condition, so the shape will be retained upon the completion of the sintering process. Finally, the suggested wavy shape sintering condition will be applied to fabricate a wavy type SC-SOFC through a co-sintering process of a multilayer structure, followed by performance tests for a comparison between the wavy type cells and the planar type cells.

Objective 1 一 Understanding of the material properties

In order to understand the sintering behaviour and properties of the materials such as shrinkage, density and uniaxial viscosity during heat treatments, free shrinkage sintering conditions and vertical shrinkage sintering conditions are applied, so called free sintering and vertical sintering respectively. By in-situ observation, shrinkage measurement of the single layer specimen is carried out, followed by calculation of shrinkage rate and density. The sintering temperature can be changed in accordance with the initial condition of the material. The sintering temperature of the anode and electrolyte materials is generally higher than that of the cathode materials. It is therefore, necessary to manipulate the materials' green layer conditions in order to co-sinter them all together and to achieve a balanced final density. The employed method to obtain the harmonised co-sintering temperature for this study is using coarse green particles for the cathode material, so that its sinterability can be deteriorated to match to that of anode and electrolyte materials. Further, properties such as sintering temperature, porosity, permeability and density should be studied to identify how these influence shrinkage behaviour during the sintering processes. A number of studies have reported that a ceramic layer with a large pore size accommodates the gases flowing through it, while resisting deformation of the layers, since the large pores lessen the stress upon the layers [33-35]. Since the sintering is a densification process of the material, it is essential to confirm uniaxial viscosity of the material at specific temperatures, since this contributes to stiffness and structural flexibility for curvature evolutions during co-sintering processes.

Objective 2 — In-situ monitoring of curvature evolutions during the co-sintering

The curvature evolutions of the multilayer structure are investigated via experimental in-situ observations during the co-sintering process. During the process, features of each ceramic layer are reflected in the interaction of layers as deformations occur. Therefore, it is necessary to monitor the dimensional

change of the structure along with the temperature profile. The variables for the specimens are either variable total thicknesses with a fixed thickness ratio, or variable thickness ratios with a fixed total thickness. The experimental curvature results are analysed based on how these factors affect curvature evolution during co-sintering and compared with theoretical models. Based on these results, a zero-deflection condition is confirmed and applied to the fabrication of a wavy type SC-SOFC via a single co-sintering process.

Objective 3 — Co-sintering temperature and wavy cell fabrication

Conventional methods have proven to fabricate only anode and electrolyte through the bi-layer co-sintering process followed by a cathode fabrication [36, 37]. However, the proposed approach in this study aims to sinter all three ceramic layers — i.e. anode, electrolyte and cathode — simultaneously. For a novel design of the SC-SOFCs, in-situ monitoring research provides the zero-deflection condition that will enable to fabricate a single cell or a stack via a single co-sintering process. As such the co-sintering process requires the harmonisation of the sintering temperature of all three layers, means reducing the sintering temperature of the anode and electrolyte material whilst increasing the sintering temperature of the cathode material. One of the possible solutions is to use mismatched powder particles in order to manipulate the powders' sintering abilities. Carefully selected green powder particle sizes will match the densification behaviours at a narrow range of sintering temperature for a successful co-sintering of all the three layers. It is well known that smaller powder particles can be sintered at a lower sintering temperature range due to their higher sinterability [38] and can reduce possibility of third phase material formation at an interface of electrolyte layer and cathode layer [39].

Two sets of flat multi-layer structures, consisting of green tape-casting layers for cell's three components, are prepared. One set is placed on alumina rods for wavy shaping during a debinding process, and another is placed on a flat substrate. Both sets are then sintering under the same zero-deflection

condition, and a wavy SC-SOFC and a planar SC-SOFC are fabricated. Once the wavy & planar SC-SOFCs were fabricated via the co-sintering processes, the cells were operated in a specially designed SC-SOFC test rig, and the output of each cell was measured and compared.

1.4 Thesis Overview

This thesis presents the development of fabrication process for wavy type SC-SOFCs with a single fabrication step, namely the co-sintering of a porous multi-layer structure. Compared with planar cells, wavy type cells are believed to increase the area of effective electrochemical reaction related with Triple Phase Boundary (TPB) sites during the operation, so are expected to deliver increased performance. In addition, the triple-layer co-sintering process can bring benefits in reduced production time, effort, and energy.

This thesis is organised according to the following scheme. The current chapter (Chapter 1) provides a brief introduction into the research topic and a statement of the motivation and objectives of the research. This introduces the need to develop a novel fabrication process for wavy SC-SOFCs and the background of the problems arisen from the conventional SC-SOFCs. In Chapter 2, a theoretical framework of the research area is described through a survey of the literature on the co-sintering of porous structures. The details of the experimental procedures carried out in this work can be found in Chapter 3. The results and discussion are divided into four chapters. Chapter 4 explains how the uniaxial viscosity of each material was determined. In Chapter 5, the curvature evolution of bi-layer structures via in-situ monitoring is presented. The results enable the prediction of curvature for a triple-layer structure and the prediction is validated by in-situ monitoring of the triple-layer structure co-sintering in Chapter 6. A zero deflection condition is confirmed through the in-situ monitoring of the triple-layer structures and the fabrication process of wavy type SC-SOFCs using the zero deflection condition is presented in Chapter 7. Also, this chapter contains the results of microstructural analysis and performance comparison, compared to the planar SC-SOFC. This study is finally concluded in Chapter 8 where findings obtained from this study are emphasized. Some possible future work is also presented.

1.5 Summary

This introduction chapter acknowledges the need to develop a novel co-sintering process for wavy type SC-SOFC fabrications. Common SC-SOFCs may satisfy requirements of the reducing manifolds and miniaturisation, but show limited applicability due to their poor performance. A wavy SC-SOFC fabricated via a single step co-sintering process is expected to deliver higher effective electrochemical reaction area enhancing the cell performance. The aims and objectives of this research are outlined, followed by a structure outline of this thesis. The developed novel fabrication process for wavy type SC-SOFCs has the potential of opening up many new SOFC technologies applications and opportunities in the field of fuel cell manufacturing technologies.

References

[1] ATKINSON, A., BARNETT, S., GORTE, R.J., IRVINE, J., MCEVOY, A.J., MOGENSEN, M., SINGHAL, S.C. and VOHS, J., 2004. Advanced anodes for high-temperature fuel cells. *Nature materials,* **3**(1), pp. 17-27.

[2] WRIGHT, G.J. and YEOMANS, J.A., 2008. Constrained Sintering of Yttria-Stabilized Zirconia Electrolytes: The Influence of Two-Step Sintering Profiles on Microstructure and Gas Permeance. *International Journal of Applied Ceramic Technology,* **5**(6), pp. 589-596.

[3] GORTE, R.J. and VOHS, J.M., 2003. Novel SOFC anodes for the direct electrochemical oxidation of hydrocarbons. *Journal of Catalysis,* **216**(1-2), pp. 477-486.

[4] CHRISTENN, C. and ANSAR, S.A., 2011. Constrained and Non-Constrained Sintering of Plasma-Sprayed Zirconia Based Electrolytes for SOFCs. *Advances in Science and Technology,* **65**, pp. 263-268.

[5] SASAKI, K., TERAI, T., SUZUKI, A. and AKASAKA, N., 2010. Effect of the Y2O3 Concentration in YSZ on the Thermophysical Property as a Thermal Shielding Material. *International Journal of Applied Ceramic Technology,* **7**(4), pp. 518-527.

[6] PRABHAKARAN, K., MELKERI, A., BEIGH, M.O., GOKHALE, N.M. and SHARMA, S.C., 2007. Preparation of a Porous Cermet SOFC Anode Substrate by Gelcasting of NiO/YSZ Powders. *Journal of the American Ceramic Society,* **90**(2), pp. 622-625.

[7] TAKAHASHI, T., IGUCHI, F., YUGAMI, H., ESASHI, M. and TANAKA, S., Fabrication of GDC-based Micro SOFC with microheaters. *Fuel,* **5**, pp. 7.

[8] EVANS, A., BIEBERLE-HÜTTER, A., RUPP, J.L.M. and GAUCKLER, L.J., 2009. Review on microfabricated micro-solid oxide fuel cell membranes. *Journal of Power Sources,* **194**(1), pp. 119-129.

[9] XIA, Q. and CHOU, S.Y., 2008. Fabrication of sub-25 nm diameter pillar nanoimprint molds with smooth sidewalls using self-perfection by liquefaction and reactive ion etching. *Nanotechnology,* **19**, pp. 455-301.

[10] KANG, Y.H., OH, S.S., KIM, Y. and CHOI, C., 2010. Fabrication of antireflection nanostructures by hybrid nano-patterning lithography. *Microelectronic Engineering,* **87**(2), pp. 125-128.

[11] MUECKE, U.P., AKIBA, K., SALKUS, T., STUS, N. and LUDWIG, G.J., 2007. Electrochemical Performance of Ni-CGO Nano-Grained Thin Film Anodes for Micro SOFCs, 2007, ECS.

[12] TIETZ, F., 1999. Thermal expansion of SOFC materials. Ionics, 5(1), pp. 129-139.

[13] GHATEE, M., SHARIAT, M.H. and IRVINE, J.T.S., 2009. Investigation of electrical and mechanical properties of 3YSZ/8YSZ composite electrolytes. *Solid State Ionics,* **180**(1), pp. 57-62.

[14] HANIFI, A.R., SHINBINE, A., ETSELL, T.H. and SARKAR, P., 2011. Development of Monolithic YSZ Porous and Dense Layers through Multiple Slip Casting for Ceramic Fuel Cell Applications. *International Journal of Applied Ceramic Technology,* pp. 1-11.

[15] ZHANG, C., ZHENG, Y., RAN, R., SHAO, Z., JIN, W., XU, N. and AHN, J., 2008. Initialization of a methane-fueled single-chamber solid-oxide fuel cell with NiO + SDC anode and BSCF + SDC cathode. *Journal of Power Sources,* **179**(2), pp. 640-648.

[16] I., R., 2010. Catalysis of electrochemical processes and the suppression of chemical ones are needed in mixed reactant fuel cells — Can this be achieved? *Solid State Ionics,* **181**(17-18), pp. 790-795.

[17] YANO, M., KAWAI, T., OKAMOTO, K., NAGAO, M., SANO, M., TOMITA, A. and HIBINO, T., 2007. Single-chamber SOFCs using dimethyl ether and ethanol. *Journal of the Electrochemical Society,* **154**, pp. B865.

[18] PILLAI, M., LIN, Y., ZHU, H., KEE, R.J. and BARNETT, S.A., 2010. Stability and coking of direct-methane solid oxide fuel cells: Effect of CO2 and air additions. *Journal of Power Sources,* **195**(1), pp. 271-279.

[19] SUZUKI, T., JASINSKI, P., PETROVSKY, V., ANDERSON, H.U. and DOGAN, F., 2005. Performance of a porous electrolyte in single-chamber SOFCs. Journal of the Electrochemical Society, 152, pp. A527.

[20] AKHTAR, N., DECENT, S., LOGHIN, D. and KENDALL, K., 2008. Modelling of Gas Flow and Electrochemical Effects in a Single Chamber-Solid Oxide Fuel Cell (SC-SOFC). ECS Transactions, 13(28), pp. 107-124.

[21] http://www.aki.che.tohoku.ac.jp/~koyama/html/research/SOFC.html

[22] http://kurl.kr/QMYD5N

[23] XIA, C. and LIU, M., 2002. Microstructures, conductivities, and electrochemical properties of Ce 0.9 Gd 0.1 O 2 and GDC–Ni anodes for low-temperature SOFCs. *Solid State Ionics*, **152**, pp. 423-430.

[24] KOH, J., YOO, Y., PARK, J. and LIM, H.C., 2002. Carbon deposition and cell performance of Ni-YSZ anode support SOFC with methane fuel. *Solid State Ionics*, **149**(3), pp. 157-166.

[25] LEE, S., MESSING, G.L. and AWANO, M., 2008. Sintering Arches for Cosintering Camber-Free SOFC Multilayers. *Journal of the American Ceramic Society*, **91**(2), pp. 421-427.

[26] LI, W., HASINSKA, K., SEABAUGH, M., SWARTZ, S. and LANNUTTI, J., 2004. Curvature in solid oxide fuel cells. *Journal of Power Sources*, **138**(1), pp. 145-155.

[27] NI, D., ESPOSITO, V., SCHMIDT, C.G., MOLLA, T.T., ANDERSEN, K.B., KAISER, A., RAMOUSSE, S. and PRYDS, N., 2013. Camber Evolution and Stress Development of Porous Ceramic Bi-layers During Co-Firing. *Journal of the American Ceramic Society*, **96**(3), pp. 972-978.

[28] HAO, Y., SHAO, Z., MEDEROS, J., LAI, W., GOODWIN, D.G. and HAILE, S.M., 2006. Recent advances in single-chamber fuel-cells: Experiment and modeling. *Solid State Ionics,* **177**(19-25), pp. 2013-2021.

[29] RIESS, I., 2005. The significance of impeded reactions in solid state electrochemistry. Solid State Ionics, 176(19), pp. 1667-1674.

[30] RIESS, I., 2008. On the single chamber solid oxide fuel cells. *Journal of Power Sources,* **175**(1), pp. 325-337.

[31] SU, P.C., CHAO, C.C., SHIM, J.H., FASCHING, R. and PRINZ, F.B., 2008. Solid oxide fuel cell with corrugated thin film electrolyte. *Nano letters,* **8**(8), pp. 2289-2292.

[32] HAANAPPEL, V.A.C., MERTENS, J., RUTENBECK, D., TROPARTZ, C., HERZHOF, W., SEBOLD, D. and TIETZ, F., 2005. Optimisation of processing and microstructural parameters of LSM cathodes to improve the electrochemical performance of anode-supported SOFCs. *Journal of Power Sources,* **141**(2), pp. 216-226.

[33] LAURENCIN, J., DELETTE, G., USSEGLIO-VIRETTA, F. and DI IORIO, S., 2011. Creep bending of porous SOFC electrodes: Measurement and

application to Ni-8YSZ cermets. *Journal of the European Ceramic Society,* **31**(9), pp. 1741-1752.

[34] MALZBENDER, J., WAKUI, T. and STEINBRECH, R.W., 2006. Curvature of Planar Solid Oxide Fuel Cells during Sealing and Cooling of Stacks. *Fuel Cells,* **6**(2), pp. 123-129.

[35] SARANTARIDIS, D. and ATKINSON, A., 2007. Redox Cycling of Ni-Based Solid Oxide Fuel Cell Anodes: A Review. *Fuel Cells,* **7**(3), pp. 246-258.

[36] LENG, Y., CHAN, S., JIANG, S. and KHOR, K., 2004. Low-temperature SOFC with thin film GDC electrolyte prepared in situ by solid-state reaction. Solid State Ionics, 170(1), pp. 9-15.

[37] LIU, Q., KHOR, K., CHAN, S. and CHEN, X., 2006. Anode-supported solid oxide fuel cell with yttria-stabilized zirconia/gadolinia-doped ceria bilalyer electrolyte prepared by wet ceramic co-sintering process. Journal of Power Sources, 162(2), pp. 1036-1042.

[38] LENG, Y.J., CHAN, S.H., KHOR, K.A., JIANG, S.P. and CHEANG, P., 2003. Effect of characteristics of Y2O3/ZrO2 powders on fabrication of anode-supported solid oxide fuel cells. Journal of Power Sources, 117(1-2), pp. 26-34.

[39] MYUNG, J., KO, H.J., PARK, H., HWAN, M. and HYUN, S., 2012. Fabrication and characterization of planar-type SOFC unit cells using the tape-casting/lamination/co-firing method. International Journal of Hydrogen Energy, 37(1), pp. 498-504.

Chapter 2

Literature Review

2.1 Sintering Process

Ceramic components are being produced using its powders at a high temperature for shape forming, and the enhancement of properties such as strength and conductivity. This is called sintering, and consists in the fabrication of objects with high density through heat-treatment [1]. During the sintering process, ceramic powders are heated to a temperature that matter transfer across grain boundaries by diffusion is highly active, fusing the particles together and thereby producing a consolidated body. It is well known that sintering is an effective method for forming powders of ceramic raw materials into complex shapes.

Through understanding the ways in which the sintering variables influence the microstructural evolution, it is possible to achieve the fabrication of ceramic structures with the required properties such as porosity, microstructure, mechanical properties, etc. Microstructural evolutions are related to influential factors such as grain size, initial density, temperature and distribution of other phases including pores. It is known that the main factors that determine sinterability and the microstructure can be classified into two parts; material properties on the one hand, and variables for the heat treatment process on another [2-4]. The factors which affect the densification and grain growth of ceramic materials during the sintering process are related with the properties such as chemical composition, size, shape, and size distribution of powder and degree of powder agglomeration [5]. The variables of the heat treatment process include factors such as temperature, holding time, pressure, heating and cooling rates. These all influence the sintering behaviour of the ceramic material.

2.2 The Sintering Mechanism

Like other irreversible processes, the sintering process is accompanied by a lowering of the free energy of the system, based on matter transport derived from diffusion of atoms, ions, or other charged species [6]. It has been generally known that the reduction of the surface free energy, derived from the elimination of internal surface area, contributes to the sintering process. The driving force for densification during sintering is a change in free energy, like the decrease in surface area and lowering of the surface free energy by the replacement of solid-vapour interfaces. As this process is achieved by material transport from regions of high energy to regions of lower energy, the parameters such as surfaces, interfaces, and grain boundaries have been related with energies which depend on surface or boundary curvature during sintering. Therefore, the overall energy of the material can be reduced by eliminating these surfaces or by minimising the curvature during the process.

Various influential factors, such as the curvature of the particle surfaces, externally applied pressure and chemical reactions, provide the main motivation for the sintering process to occur. As surface curvature of a particle is inversely proportional to the surface area of the system of particles, the surface free energy associated with the system of particles by a product of the specific surface energy and the surface area can be influenced to be activated depending on the curvature of a particle. Assuming that an effective stress on the atoms under the surface is influenced by the specific energy and curvature of the particle surfaces, this stress is given by:

$$\sigma = \gamma_{rs} \left(\frac{1}{r_1} + \frac{1}{r_2} \right) \tag{2.1}$$

where principal radii of curvature are r_1 and r_2 for a curved surface, and the specific surface energy is γ_{rs}. With the diffusion potential, μ, the equation for μ is commonly used:

$$\mu = \sigma \, \Omega \tag{2.2}$$

where Ω is the atomic or molar volume. For ceramic materials where the pores are in contact with the grain boundaries, this equation is more complex. Assuming that pores are spherical in the final stage of sintering, Raj [7] proposed the diffusion equation given by:

$$\mu = \Omega \left(\frac{2\gamma_{gb}}{G} + \frac{2\gamma_{sv}}{r} \right) \qquad (2.3)$$

where γ_{gb} is the specific energy of the grain boundary, G is the diameter of the grains, and r is the radius of the pores. In this case, the conditions of the pores and boundaries are related with the diffusion potential during sintering.

Although surface curvature contributes to the driving force, its influence is much smaller than that provided by external pressure. Applied pressure can be useful through hot pressing and hot isostatic pressing [8]. A chemical reaction that aids densification occurs during the sintering process.

From the viewpoint of atomic diffusion, it is known that there are six common mechanisms. These are surface diffusion; vapour transport (evaporation/condensation); lattice diffusion from surface; grain boundary diffusion; lattice diffusion from grain boundary, and plastic flow as shown in Figure 2.1. Not all of these factors participate in the densification process during sintering. Even though these six mechanisms lead to bonding and the growth of necks between particles — thereby increasing the strength of the material compact during sintering — only certain mechanisms can participate in shrinkage and densification. The distinction is mainly drawn between densification and non-densification mechanisms. Among them, surface diffusion, vapour transport and lattice diffusion from the particle surfaces to the neck can cause neck growth and coarsening of particles without densification occurring during sintering. On the other hand, densification mechanisms such as grain boundary diffusion, lattice diffusion from the grain boundary to the neck, and plastic flow can lead not only to neck growth but also to densification. When the non-densification mechanisms dominate during the sintering process, coarsening causes the production of a porous structure, while a dense structure can be fabricated when the densification mechanisms dominate.

- Surface diffusion: Diffusion of atoms along the surface of a particle
- Vapour transport: Evaporation of atoms which condense on a different surface
- Lattice diffusion from surface: Atoms from surface diffuse through lattice
- Grain boundary diffusion: Atoms diffuse along grain boundary
- Lattice diffusion from grain boundary: Atoms from grain boundary diffuses through lattice
- Plastic flow: Dislocation motion causes flow of matter

Figure 2.1 Sintering mechanism derived from diffusion of atoms [6]

In the ceramic sintering process, grain boundary diffusion and lattice diffusion are particularly important mechanisms for densification. Generally, sintering normally occurs in three sequential stages [9, 10]. The initial stage consists of neck contacts between particles by a diffusion process. The initial difference of surface curvatures between particles is removed at this stage, and neck growth for the densification mechanisms is accompanied by the first few per cent of shrinkage. It is well known that a linear shrinkage of 3% ~ 5% occurs for a powder system with an initial density of 50% ~ 60% of the theoretical density (TD). In the intermediate stage of sintering, the pores have reached their equilibrium shape and are interconnected with each other. Densification is assumed to occur through the pores simply shrinking, thus reducing their cross section. Here the density of powdered material increases dramatically with grain growth. The intermediate stage generally involves the main part of the sintering process, up until the TD reaches a value of 90%. The final stage begins when the connections of pores pinch off and the pores become isolated from each other at the grain corners. In other words, the pores are presumed to shrink continuously and may almost disappear. This mainly

begins when the density of a compact reaches above 90% TD. This is followed by a rapid decrease in the densification rate.

As various sintering mechanisms occur together, they might lead to coarsening of the microstructure (including grain growth and pore growth) and a reduction of the sintering force, contributing to a significant reduction of the densification rate. Under a competition between densification and coarsening, the sintering condition would be chosen as shown in Figure 2.2. It is known that pore growth is driven by both grain growth and densification during sintering and is affected by the properties of powder compacts [11]. Though grain growth and densification take place at the same time, grain growth leads to size proportional pore agglomeration while densification results in pore shrinkage or the decrease of the size ratio of pores to grains. For the production of ceramics with high density, the process would require the condition which the densification mechanisms are very active during sintering. On the other hand, the production of a highly porous ceramics would be obtained under the condition which coarsening mechanisms dominate.
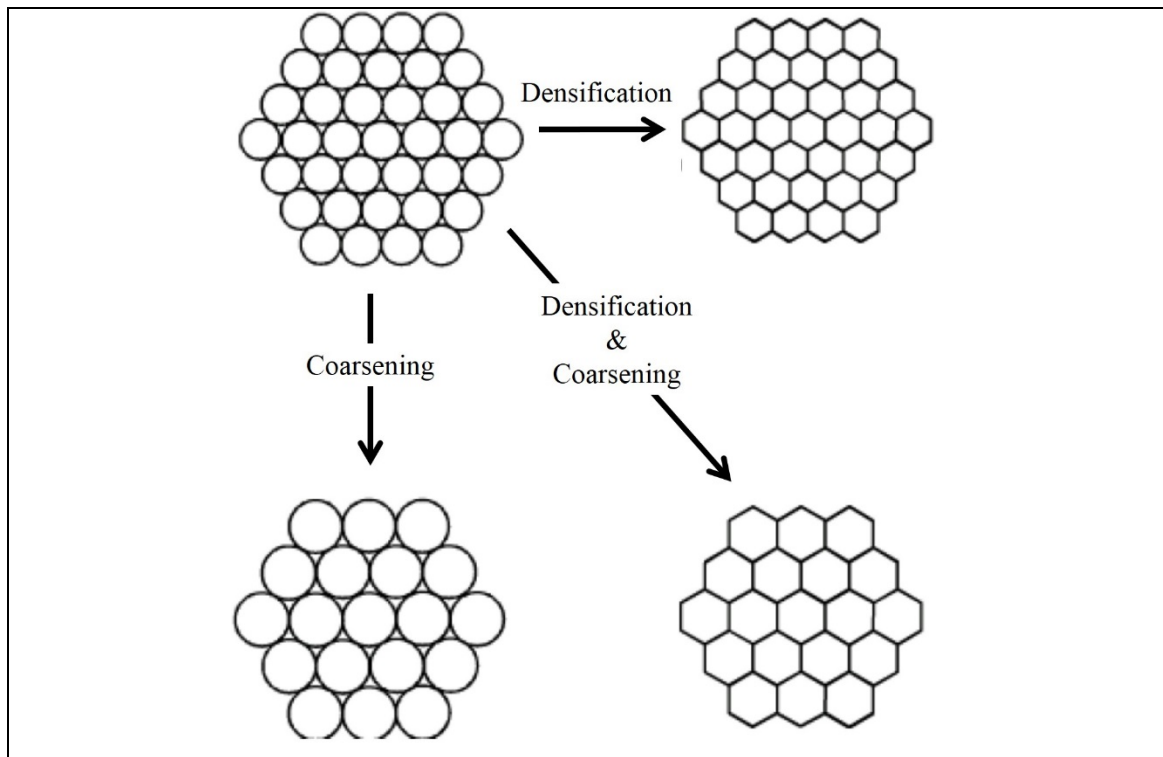
Figure 2.2 Densification and Coarsening during sintering

2.3 Sintering type

Free sintering

In a sintering process, shrinkage behaviour of green body depends on experimental conditions such as green density, sintering temperature profile, thickness of green body, etc. Sintering of a freestanding body can be carried out at its sintering temperature without application of any external constrains that may influence its natural shrinkage behaviour, in order to achieve a uniform shrinkage rate [12, 13]. Figure 2.3 shows schematically diffusional change before and after the sintering process. In this case, only one dimension needs to be monitored in order to obtain the overall volumetric changes. As a result, the diffusion of atoms — as well as the reaction between particles during sintering — can lead to shrinkage of the dimension of the sample in all three directions; D, L, W in Figure 2.3. Prior to reaching the main part of the sintering process, additives such as binders are already eliminated as part of a burnout step, in the so-called debinding process. Subsequently, the particles in the ceramic sample are rapidly activated with neck growth and pore removal. It is difficult to say where the activation range of the specimen lies between the initial and the final condition during the sintering process. That is because the activating area for densification varies according to the initial properties, even if the identical ceramic powders are used for the same process. After completing all heat treatment, including cooling down to room temperature, the dimension of the ceramic sample has shrunk in all directions as an isotropic sintered material.

| Before Sintering | After sintering |
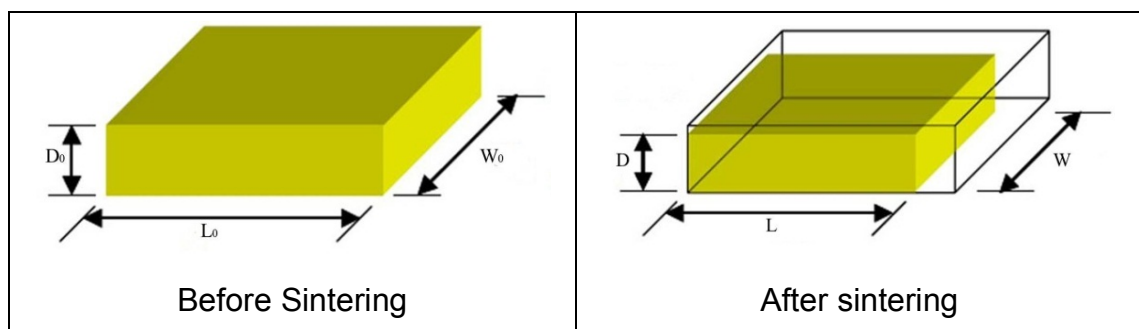
Figure 2.3 Dimensional changes in a freestanding ceramic material undergoing isotropic shrinkage

Constrained sintering

The idea of constrained sintering has been a point of interest due to the ceramic industry's need for an accurate control of shrinkage, so as to maintain the required tolerance of the final product [14, 15]. For a constrained film, a green layer is usually deposited on a relatively rigid substrate prior to a sintering process. A dominant shrinkage of the ceramic green layer occurs in its thickness direction during the sintering process, whilst the shrinkage in in-plane directions (X-Y directions) is constrained by the substrate. To sum up the distinction between a free sintering and a constrained sintering, a free sintering can be claimed that the ceramic green body normally shrinks in three dimensions during the process, whereas the green body on a rigid substrate accompanies almost zero shrinkage to in-plane directions. Thus, only thickness direction shrinkage is allowed during the constrained sintering. Figure 2.4 shows a schematic diagram for a constrained sintering process.

As lateral constraint imposed by a rigid substrate allows shrinkage only in the direction perpendicular to the film, the imposed constraint induces in-plane stress contributing to acceleration of the shrinkage in its thickness direction. In constrained sintering, it can be said that the stress in the x-direction is equivalent to that in the y-direction and that the sintering kinetic (or strain) in the x-y direction is constant to zero. It is also well known that film thickness influences the viscosity and the sintering stress of the film, since the grain size is comparable to the thickness of a thin film. As compared to free sintering, not only grain growth but also densification can be considerably retarded due to the constraint condition.

| Before sintering | After sintering |
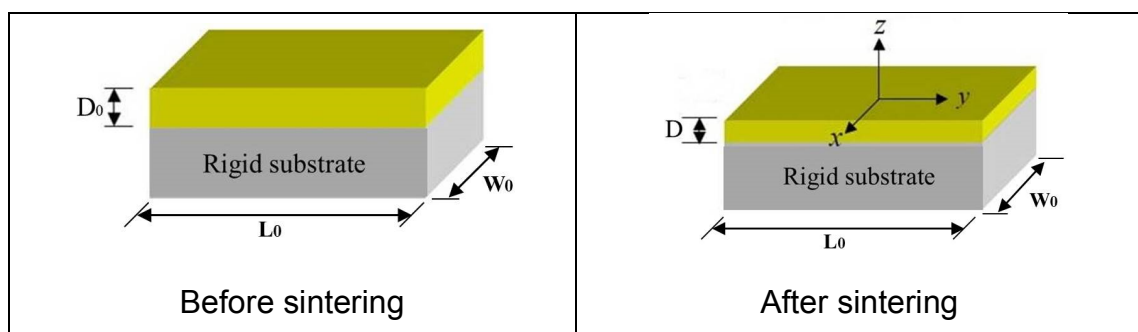
Figure 2.4 Schematic of the shrinkage of a film constrained on a substrate undergoing constrained sintering

Co-sintering

For the sintering of multilayer structures, a co-sintering process can be applied in order to achieve a sintered object via a single sintering process [16, 17]. Green layers are usually prepared by a tape casting method and then laminated together through a hot pressing method. The co-sintering process helps in reducing repeated sintering processes for fabricating a multilayer structure. However, when several porous green layers are sintered altogether as a whole, both the sintering kinetics and curvature evolutions of the layers are very important. In addition, stresses may be induced due to a mismatch of sintering kinetic between individual layers. These stresses at the interfacial surface between layers can lead to curvature development, non-uniform shrinkage, or even mechanical defects like cracking and delamination. In order to avoid the occurrence of these undesired behaviours, sintering behaviours of each layer should be understood so that level of induced stresses can be controlled within the allowable range. The layer configuration of the multilayer structure also plays an important role throughout the process for determining the allowable range for the stresses. As shown in Figure 2.5, a co-sintering process of multilayer structures is accompanied by in-plane stresses as well as shrinkages at the same time. This sintering method is widely used in the field of multilayer low temperature co-sintered ceramics (LTCC) for planar sensors, fuel cells and batteries [18, 19].

| Before co-sintering | After co-sintering |
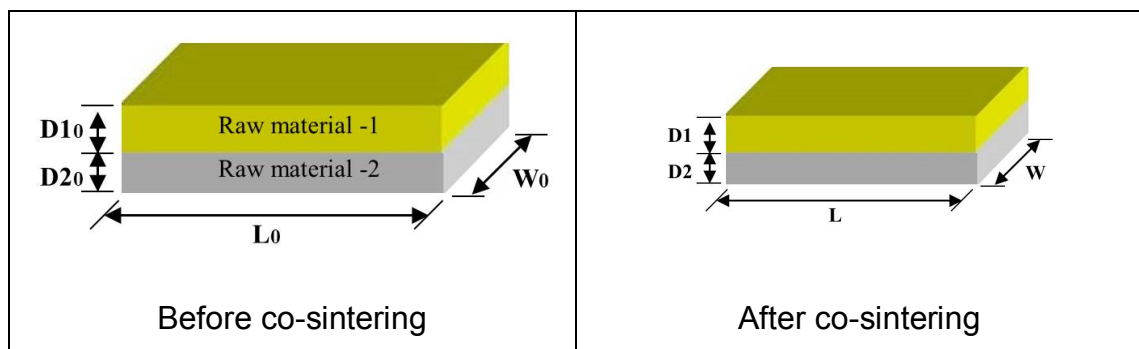
Figure 2.5 Schematic of shrinkage in a bi-layer structure during co-sintering

2.4 Elastic-viscous analogy in theoretical/experimental approaches

During free sintering of ceramics and metal power compacts, the mechanical driving force for shrinkage is generally referred to as sintering stress. This sintering stress is the combined action of the inherent stress derived from the existence of porosity in a powder compact. It is well known that the stress is a function of the powder compact geometry, powder particle size, shape, packing and the distribution and evolution of these properties [20, 21]. Also, it is an important quantity that enables the macroscopic component of shrinkage and dimensional changes during sintering. In contrast to the meaning of sintering stress, compressive or tensile stress in bi- or multilayer structures is referred to as induced stresses when the structure is treated in a constrained- or co-sintering process [22]. Experimentally measuring the stress of a multilayer structure is difficult, and any changes in powder or compact characteristics require numerous and tedious experiments. Although many analytical formulations have been conceived for measuring stress in multilayer structures, many researchers have used Stoney formula, Equation (2.4), and Extensions of Stoney formula for relations between the thin-film stresses and substrate curvatures [23-25]. And the stress (σ_f) of the film is given by:

$$\sigma_f = \frac{E_s h_s{}^2 \kappa}{6 h_f (1 - v_s)} \tag{2.4}$$

In the above, the subscripts "f" and "s" denote the thin film and substrate, respectively. E is the Young's modulus, v is the Poisson's ratio, κ is the curvature of the structure, and h is the thickness. Stoney's formula for a bi-layer structure involves the following assumptions:

i) Both the film thickness and substrate thickness are uniform, the film and substrate have the same radius, extremely small compared with radius of curvature

ii) The strains and rotations of the plate system are infinitesimal

iii) Both the film and substrate are homogeneous, isotropic and linearly elastic

iv) The film stress are in-plane isotropic or equibiaxial while the thickness direction stress and all shear stresses are removed

v) The components of curvature in the bi-layer structure are equibiaxial while the twist curvature vanishes in all directions

vi) All stresses and curvature components are spatially constant over the surface of the plate system

Under the assumptions, it is difficult to figure out the curvature evolutions in various conditions such as the non-uniformity of the stresses, the tri-dimensionality and the boundary conditions of the samples. These conditions might give rise to empirical modifications and more elaborated models including local dependence to stress distribution [26-28]. Experimentally, as the thickness is not constant and in-plane stresses are variant during co-sintering, the co-sintering of the multi-layer structures in this study does not meet the requirements proposed by Stoney. Furthermore, the thickness ratio of thin layer to thick layer is greater than that described in the assumption. Although these assumptions are limited to specific conditions and cannot reflect real situations for accurate value, they can provide a basic quantitative value for stress measurement of the film coated on a substrate.

During the sintering process, the diffusion process dominates for polycrystalline materials and viscous flow is dominant for amorphous materials. The materials exhibit properties of both viscous and elastic characteristics, called viscoelasticity. Viscoelastic materials have elements of both of these properties and exhibit time dependent strain. Since the announcement of the Stoney formula, studies such as those carried out by Bordia and Scherer [1, 5] have shown that the concept of viscous flow was systematised for deformation analysis of a sintering body, instead of linear elastic mode. In this viewpoint, the stresses and strains in the sintering body can be analysed using viscoelastic analogy. As the sintering materials do not follow linear viscoelasticity, it might be difficult to apply to the co-sintering of multi-layer structures. Although the modification of constitutive equations by Scherer [29] was developed for the study of sintering behaviour by viscous flow, it has been applied to the analysis

of densification by viscous flow and solid state diffusion. Assuming that the sintering process is viscoelastic, many studies of the stress analysis of ceramic materials have used the viscoelastic analogy with constitutive equations. It is well known that the use of the viscoelastic analogy further facilitates the analysis of stress in viscoelastic materials like ceramics. In general, shear modulus and bulk modulus describe the elastic behaviour of an isotropic material, and the constitutive equation can be used by Hook's law in terms of the principal stresses (σ) and strains (ε) in the x, y and z directions, as in Equation (2.5):

$$\varepsilon_x = \varepsilon_f + \frac{1}{E_0} \left[\sigma_x - v_0 \left(\sigma_y + \sigma_z \right) \right] \qquad (2.5)$$

where E_0 is Young's modulus, v_0 is Poisson's ratio and ε_f is strain of free sintering. With elastic-viscous analogy, this equation can be converted into a viscoelastic equation, as in Equation (2.6):

$$\dot{\varepsilon}_x = \dot{\varepsilon}_f + \frac{1}{\eta} \left[\sigma_x - v_p \left(\sigma_y + \sigma_z \right) \right] \qquad (2.6)$$

where $\dot{\varepsilon}$ is strain rate, η is the uniaxial viscosity of the porous body and v_p is viscous Poisson's ratio. The viscous components can be modelled as a time derivative form, such as stress - strain rate relationship. Although a ceramic material is not linearly viscoelastic when the elastic modulus is a function of time or strain, it is reasonable to assume that the sintering material is viscoelastic, because the materials interact to an external force with a prompt elastic strain and a continuous geometric variation controlled by viscous flow. Also, as delayed elastic strains are not important compared to the viscous strain that occurs during sintering, this relation can be applied for stress analysis of ceramic materials. In general, the strain rate of free sintering is related to the sintering potential, Σ, by Equation (2.7) with bulk modulus, K_p, given by:

$$\dot{\varepsilon}_f = \frac{\Sigma}{3K_p} \qquad (2.7)$$

$$K_p = \frac{\eta}{3\left(1 - 2\nu_p\right)} \qquad\qquad (2.8)$$

As sintering potential and free strain rate are negative due to contraction during sintering, bulk modulus has a positive value in Equation (2.7). Likewise, when viscous Poisson's ratio varies from 0 to 0.5, it is possible to utilise Equation (2.8) with positive viscosity.

The sintering behaviour of a bi-layer structure have been influenced by not only dimension of the structure but also material properties such as viscous Poisson's ratio, TEC, sintering strain, percentage theoretical density (%TD) of a green ceramic material, etc. As these parameters affect stresses and curvature evolution of the structure during sintering, many studies have been performed to figure out the relationship between these parameters and stresses.

It is highly important to measure the viscous Poisson's ratio, since this requires very precise measurements of density and shrinkage rate. There are various ways to determine the viscous Poisson's ratio of materials during the sintering process [8]. These studies help to calculate stresses and distortions of ceramic structure during sintering. This is important to do, since not much is known about the way in which this factor affects things during sintering and how it changes with specific temperature conditions. The average value has generally shown a range from 0.26 at 70%TD to 0.35 at 90%TD. With a constrained sintering experiment, this value can be determined based on elastic-viscous analogy under the assumptions in the derivation of viscous Poisson's ratio.

- During sintering, the ceramic material has linear viscous behaviour. The strain rate varies linearly with the applied stress
- The stresses in the out-of-plane direction are always constant
- The free sintering rate is irrelevant to stress derived from constrained sintering
- Radial shrinkage of the material is zero through the thickness
- The viscous Poisson's ratio is a function of density

In this condition, several equations including Equation (2.9) can be added for linear viscous material during constrained sintering. For a multilayer structure, when the shrinkage of interfacial surface (x-y direction) is isotropic, even though it is not equivalent to that in thickness direction, the strain rates of free sintering are deduced as

$$\dot{\varepsilon}_{fx} = \dot{\varepsilon}_{fy} = \frac{\dot{\varepsilon}_{fz}}{w} \tag{2.9}$$

where w is the anisotropic parameter. Also, since any external uniaxial loads do not apply to this specimen during sintering,

$$\sigma_z = 0 \tag{2.10}$$

For the case of constrained sintering, the strain in the x-y plane equals zero.

$$\varepsilon_x = \varepsilon_y = 0 \tag{2.11}$$

Through these equations, the equation for viscous Poisson's ratio can be inferred as follows:

$$\nu_p = \frac{k\left(\dot{\varepsilon}_z - \dot{\varepsilon}_{fz}\right)}{k\left(\dot{\varepsilon}_z - \dot{\varepsilon}_{fz}\right) + 2\,\dot{\varepsilon}_{fz}} \tag{2.12}$$

Depending on the value of anisotropy, it can be applicable to the analysis of shrinkage behaviour based on constrained sintering.

Many studies have been carried out using bent multilayer structures, especially regarding thermal and residual stress [9-12]. These studies have demonstrated the ways in which these stresses develop during the heating and cooling of a metal/ceramic specimen. The materials behave elastically or plastically depending on properties such as the dimensions of the structure; the mismatch of thermal expansion; stiffness, and thermal gradient. Trends of stress behaviour have been introduced in bending structures, where the concept includes the location of the neutral axis, the elastic/plastic boundary,

and the curvature. These are derived from variables such as thickness ratio, and misfit in thermal expansion coefficient.

As a result of these studies, it was emphasized that the compatibility at interfacial surfaces between layers needs to be estimated, due to the number of boundary conditions for analysis of thermal stresses increasing with the number of layers. Since a variety of investigations have been performed for stress analysis with bi-layer beam structures in constrained sintering, it is more accurate to use plate modulus, α, of the substrate rather than the Young's modulus. It is well known that in a wide cantilever beam where the width is approximately five times greater than the thickness, the beam will exhibit plane-strain conditions and the effective modulus of the beam will trend away from the Young's modulus and towards the plate modulus [10]. This can be expressed as:

$$\alpha = \frac{E_0}{1 - {v_0}^2} \qquad\qquad (2.13)$$

Further, isotropic constitutive law — as described for anisotropic behaviour — has suggested that if anisotropy develops during the sintering process then %TD is not an important factor in describing the state of the material, even though %TD and average grain size have been widely utilised to define a sintering material in isotropic constitutive laws. Following Cock's research in the interest of accurate data analysis, it has been suggested that the %TD factor could be replaced by the factor of sintering strains [14]. As it is difficult to characterise the anisotropic behaviour, these studies suggested critical density, which can divide several sections of the sintering process so as to empirically obtain extended constitutive laws.

Some studies have investigated modifications of Stoney's Equation as well as influential in terms of specific conditions, such as cylindrical bi-layers [15-18, 30, 31]. Although the original equation can be applied in the condition that thickness ratio between a film and a substrate should be satisfied to no more than 1% so that the error does not exceed 5%, modified formulae provide the extended range of thickness ratio to up to 10%. Also, if there is no in-plane

stress, the assumption of a uniform curvature is valid for small deflections, followed by determining the curvature, as derived from Young's modulus and the thickness ratio. Despite all these efforts, various investigations have been struggling to analyse the exact stresses in a multilayer structure using extended equations due to elements of uncertainty such as anisotropic behaviour [32-34]. The separate sections are transformed from an initially equibiaxial to a subsequently biaxial curvature induced by an increase in film stress beyond a certain critical value. This critical value is related to the structure aspect ratio. In particular, thin film stress depends on non-local substrate curvatures. This means that the stress components at a specific point of the film depend on both the local value of the curvature components and on the value of curvatures of all other points in the plate system. It has been shown that modified equations are valid with the result of the 3D calculation with less than 5% error, in cases where a ratio of the depth of the beam structure to thickness is greater than 11. This should be taken into account for non-uniform misfit strain distribution and for substrate thickness, as if it were a real experimental condition. In accordance with this point, analytical equations and its various extensions cannot include the non-locality of the dependence of stress and curvature.

2.5 Analysis of curvature evolution during co-sintering

Stress measurement by Cai's model

A number of studies have explored theoretical links as well as experimental verifications for stress measurement with curved structure [35-37]. It was experimentally pointed out that an increase in thickness ratio could give rise to the relative uncertainty of stress based on an accumulation of errors. Theoretical approaches should be restricted to the condition of the ratio of the substrate thickness to the film thickness being greater than 10%. Although the structure satisfies the internal stress equilibrium from the viewpoint of the mechanics, the location of a neutral axis placed to affect the structure to be bent may vary depending on differences of the elastic modulus between a film and a substrate. It should thereby be taken into account that the neutral axis

may deviate from the centroid or interface. That is because the distance from the neutral axis to the specimen surface is usually needed in order to calculate the surface strain from the measured curvature. These bending experiments show that the error derived from extended equations could be decreased when increasing the thickness ratio of substrate to film. Further, since average stress during the bending motion is a function of the thickness ratio, increasing the thickness ratio could reduce the deviation. It has also been indicated that in the state of an interfacial surface with delamination, cracks may produce an additional imbalance in stress distribution. In addition, the behaviour of ceramic material can be converted from elastic regime to viscous regime during sintering. In this process, the properties may also follow viscosity mode. It is difficult to segregate the boundaries that ceramic materials may go partially or fully beyond in their elastic deformation range during sintering. This is because different plastic zones between layers will spread simultaneously with increasing temperature. Therefore Alan et al [38] have suggested a stress measurement method that works without calculating the viscosity factor. Using extended formula with horizontal and vertical displacements of thin film during sintering, stress induced from coating on a rigid substrate can be estimated without a complicated procedure. It is, however, limited in its application to multilayer structures with different components.

$$\rho = \frac{a^2 + b^2}{2a} \qquad (2.14)$$
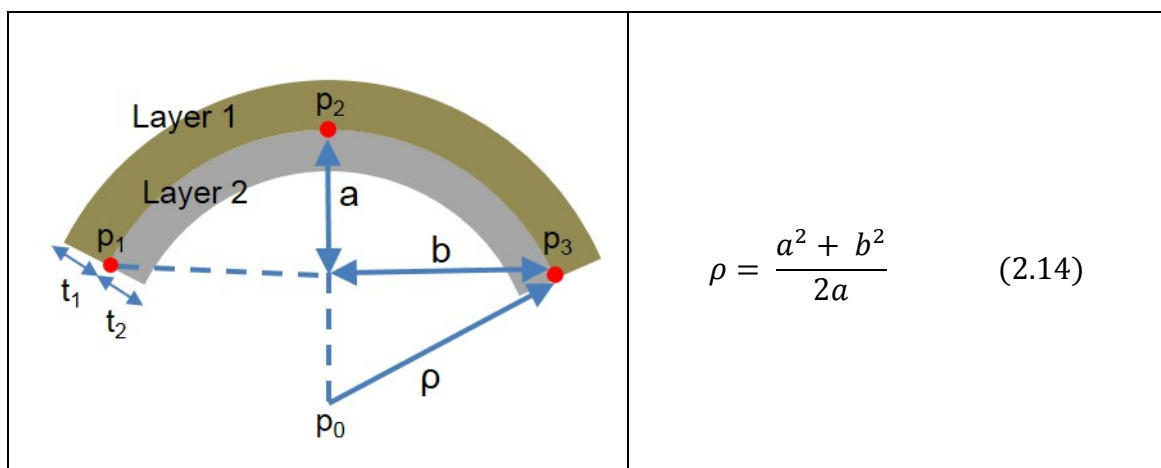
Figure 2.6 Schematic of bi-layer structure with curvatures towards layer 2

Figure 2.6 shows the schematic of experimental measurement of radius of curvature in a bi-layer structure. By in-situ monitoring of curvature evolutions

of a bi-layer structure, the radius of curvature can be calculated using Equation (2.14) with measurement of distances of P_0-P_2 and P_1-P_3. For curvature developments, Cai's model was chosen to investigate stresses of a bi-layer structure at the interface during co-sintering [30, 31]. Based on the model, the use of stresses integral and bending moments along the thickness to zero were applied to investigate stress development in bi-layer structures. This model for bi-layer structures demonstrates that curvature evolution releases the mismatch of stresses between layers during co-sintering. Assuming that the each layer in the structure can be considered as a linear viscous, the normalised curvature rate, $\dot{k}$ (thickness over radius of curvature), measured from shrinkage behaviour during co-sintering can be given by:

$$\dot{k} = \frac{d(\frac{t_1 + t_2}{r})}{dt} = \left[\frac{6(m+1)^2 mn}{m^4 n^2 + 2mn(2m^2 + 3m + 2) + 1} \right] \Delta \dot{\varepsilon} \qquad (2.15)$$

where t_1 and t_2 are the thickness of layers, r is the radius of curvature, $m = \frac{t_1}{t_2}$ is the thickness ratio, $n = \frac{\eta_1}{\eta_2}$ the viscosity ratio, $\Delta \dot{\varepsilon}$ is the difference of the shrinkage rate between layers. It is demonstrated in the equations that if properties are similar in the bi-layer structure, the values of viscosity and shrinkage rate are almost fixed; therefore, the only influential factor to affect curvature change of the structure during co-sintering is the thickness ratio. The viscous Poisson's ratio (v) can be roughly calculated by the %TD of the sintered sample (ρ).

$$v = \frac{1}{2} \sqrt{\frac{\rho}{3 - 2\rho}} \qquad (2.16)$$

The difference of strain rate in the interface of the bi-layer structure results in sintering mismatched stresses. This difference can be applied to calculate the nominal viscous mismatched stress ($\widehat{\sigma_1}$) in top layer.

$$\widehat{\sigma_1} = \left(\frac{\eta_1}{1 - \nu_1}\right) \Delta \dot{\varepsilon}_{2-1} \qquad (2.17)$$

The maximum stress in top layer, σ_1^{Max}, occurs at the interface and can be calculated by:

$$\sigma_1^{Max} = \left[\frac{m^2 n\,(4m + 3) + 1}{m^4 n^2 + 2mn(2m^2 + 3m + 2) + 1}\right] \widehat{\sigma_1} \qquad (2.18)$$

where $\widehat{\sigma_1}$ viscous mismatched stress of top layer.

As it is the main goal to find zero-deflection condition of a multi-layer structure at the final stage of the co-sintering, the analysis of curvature evolution of the structure during co-sintering should be carried out. As curvature evolutions are derived from the mismatch of sintering behaviour between layers, the properties of materials should be investigated through free sintering. Then, how these factors affect each other during co-sintering and develop curvature evolution of the bi-layer structure should be analysed.

Co-sintering of thin structures fabricated by tape-casting method

Among the fabrication methods of multilayer structure for experimental research, the tape casting method has been widely used to produce ceramic layers [39-41]. It is well known that this method can be used to laminate together green ceramic tapes with various components, thereby enabling different characteristics derived from factors such as porosity and initial density to be present during sintering. In using this method, one must ensure that the tapes have the same sintering behaviours in order to avoid delamination, warping and cracks in the sintered structure. As these behaviours are difficult to obtain using traditional processes such as the powder pressing method, numerous studies have been investigated for the purpose of demonstrating that a reduction in differential shrinkage can be accomplished by mixing ceramic powders of various sizes and shapes or by organic particulates which pyrolyse during the binder removal stage, leaving stable voids. As smaller pore networks derived from particle bridging in the green tape connect with large pores, additional voids induced by particle bridging may be the source of excess

porosity occurring in the sintering process. In bending experiment conditions, assumptions such as isotropic and linear behaviour are hardly valid during the multilayer sintering process [42, 43]. Messing's well known analysis [44] provides an appealing explanation of the curvature evolution of a ceramic multilayer structure during co-sintering. It has been shown that the relative viscosity of each layer brings about curvature evolution, although curvature is commonly affected by the mismatch of sintering shrinkage between layers.

Furthermore, these works suggested that curvature is more noticeable in cases where each component has a similar viscosity and the same thickness. On the other hand, curvature is seldom observed when the difference of relative viscosity between layers is much higher, despite the mismatch in shrinkage behaviour. In other words, it can be said that differences of viscosity makes curvature behaviour with a certain thickness ratio contribute to influence the entire curvature of the ceramic structure during co-sintering. Besides, the estimation of the curvature rate allows qualitative insight on the internal stresses that may be the reason for shrinkage behaviour. The variation of dimensions during co-sintering can be observed and recorded by an optical system. In bi-layer structure experiments, the curvature shape, i.e. whether it is concave or convex, was shown to depend on a difference of various properties as a main function of temperature. According to these results, establishment of the optimal temperature range for reduction of unnecessary modification should be considered, so that well-controlled sintering behaviours can yield the desired results.

During the sintering process, with dimensional shrinkage and bending deformation, thermally induced stress may reach beyond critical level, resulting in cracking and fracturing of the laminated ceramic structure [45-49]. It has been noted that although the fracture behaviour is normally dominated by unstable crack propagation from defects at the interfacial surface, and oriented parallel to the thickness direction, the fracture stress of the laminated layer is higher than that of a single layer. This is due to achieving good bonding between layers with microstructure improvement, which is able to cause restraint during the opening of a crack of the interfacial surface. In our laminating process, the hot-pressing method as a function of temperature, pressure and holding time can be utilised for the multilayer structure, but vacant

space between layers may occur during this process, resulting in propagation of the crack during the heating cycle. Crack growth behaviour along porous ceramic layers is very important in the fabrication of a porous multilayer structure in particular. It provides information on the microstructural mechanism since the condition of stress concentration around pores may be expected by the pore state, such as pore morphology, distribution and spacing. As thermally induced stress affects the contribution to energy release during the crack propagation process — especially in high viscosity value at dense condition — the crack has grown and extended further so that it leads to the increase of a local crack opening, or to a multilayer structure which can be broken off.

2.6 The co-sintering method

Influential parameters

Extensive constitutive equations with many parameter terms have been published for use in the simulation analysis of sintering behaviour. Some of these studies originated from micromechanical models and others were based on empirical experimental data. Recently, a combined method [50] with laws and empirical fitting has been used for the prediction of sintering deformation. As described above, it is well known that a simple method for the analysis of sintering behaviour and kinetics is the use of the dilatometer apparatus. Although this method allows for measurement of both instantaneous shrinkage rates as well as applied stress during sintering, one must take into account its inherent assumption that micro structural evolution under a certain applied loading is almost identical to that of free sintering [51, 52]. As grain growth rates and pore shapes under free sintering are different from those under applied stress, this assumption is essential. It is well known that the key parameters influencing sintering behaviour are usually divided into two parts: internal factors such as grain size, pore distribution, a ratio of additives like binder, solvent; and external factors such as sintering temperature, heating rate, dimensional ratio and structure configuration. [53].

a) Temperature

It is generally assumed that the effect of temperature is the dominant factor in promoting the entire procedure for sintering behaviour, and influences the microstructure which is subject to viscosity and activation energy for matter transport [54-57]. Also, increasing temperature leads to the activation of grain growth and pore elimination so that the ceramic structure can be made denser during sintering. As the viscosity initially decreases with temperature and increases toward the later stages of densification, microstructural deformation derived from viscosity variation is eventually dominated by temperature. All ceramic materials have their own sintering temperature range and the same materials may have different sintering temperature ranges depending on variables such as particle size and solid content in the slurry. In co-sintering processes, it is very important to determine the active sintering temperature range, since structures that consist of several layers with different sintering behaviours have to be treated by a single heating cycle. One should take into consideration both the sintering temperature of the materials as well as the uniform temperature range in which each material can be sintered.

b) Grain size

As sintering is a densification process with particles fusing together as a result of atomic diffusion, the effect of particle size plays a significant role in terms of temperature. Many studies have been examined in order to determine how the particle size varies depending on temperature and how this affects sintering behaviour [58-61]. In studies where the material is the same bar for particle size, it has been shown that the factor of particle size significantly alters sintering behaviour. The application of smaller sized material — i.e. nano-sized powder instead of micro-sized powder — has shown that the maximum shrinkage rate of smaller sized material will occur earlier rather than in micro-sized material. This implies that it is possible to apply a modification of particle size in the green body, for the sake of reducing the mismatch of sintering behaviour between layers at a specific temperature. On the other hand, too small a particle size may lead to negative problems for densification on account

of the relation between particle size and pores. It is difficult to achieve full densification under pressureless sintering conditions in the case of the densification process of a nano-sized material with low initial density. This is due to the existence of a stable large pore. Also, grain growth occurs with increasing temperature as atoms diffuse to new positions, resulting in one grain growing at the expense of another. The reason why grain growth should be considered is that the properties of ceramic material are dependent on grain size. It increases the diffusion distance, thus contributing to a reduction in the densification rate. It is also known that rapid densification in the condition of controlled grain growth takes place at lower temperatures, followed by rapid grain growth with little densification at higher temperatures.

c) Pores

It may be said that the densification process during sintering is equivalent to the pore elimination process, and so it is essential to have a proper understanding of the pore evolution. Although pores can be removed with decreasing coordination numbers due to grain growth and rearrangement during sintering, a certain sintering condition leads to pore growth and grain growth due to the coalescence of small particles into large ones [62]. It is generally noted that in order for the pore to shrink, a decrease of the free energy derived from the decrease in the pore surface area should be greater than an increase due to the increase in the grain boundary area. Also, the distribution and shape of pores may cause a decrease in the sliding or rotation on the grain boundary, contributing to energy dissipation during sintering [63]. These behaviours can influence anisotropic microstructural developments in multilayer structures [64, 65]. In co-sintering, it should be taken into account that the different densification behaviours between layers affect the properties related to pores along the thickness direction, so it may lead to a microstructural gradient, resulting in the generation of a stress gradient at the same layer during sintering.

d) Additives in suspension for ceramic tapes

The microstructural evolution during sintering has been influenced by the microstructure of the green body. For the tape casting method in particular, it is important to take into account the state of the slurry as well as the direction of casting, in determining the initial state of microstructure prior to sintering. It has been investigated how the additional components such as the binder, and the dispersants in the green body, influence the densification behaviour, and how it affects stress distribution during sintering [66-69]. Although these materials do not participate in the sintering process directly, they act on the properties of the ceramic slurry followed by changing the initial position of particle distribution or the active temperature zone for densification during sintering. When the thermal debinding process at low temperature occurs, at the interface of the binder-vapour, it is possible that the flow path of vapour breaks the connection of particles or causes the dimension of pores between particles to broaden.

e) Layer configuration

As the initial state of the microstructure of green tapes, such as particle alignment and distribution, may affect the sintering behaviour of the multilayer structure, it is important to consider the method for assembling layers, in order to reduce negative effects during co-sintering. Some studies have investigated layer configuration, considering how directional property influences the shrinkage behaviour and how to determine conditions such as pressure, temperature, time, etc. for multilayer structures [70-72]. In our research, new lamination conditions have to be taken into account as stress derived from mismatching of sintering behaviour should be minimized during the co-sintering process.

2.7 Fabrication of SC-SOFC

Fundamental

Unlike the dual chamber type, the SC-SOFC consists of only one gas compartment containing a gas mixture of fuel and oxygen [73-77]. The main principle in SC-SOFC is based on the selectivity of the electrodes for high performance. In other words, the anode has to be selective and electrochemically active for the oxidation of the fuel, as well as be inert to the reduction of the oxidant, whilst the cathode must exhibit selective reduction of oxygen and be inert to the reaction with fuel gas. Therefore, both the electrochemical activity and the selectivity of the electrodes lead to the generation of electricity in SC-SOFC.

The advantages and disadvantages of SC-SOFCs are summarised in Table 2.1. The use of gas mixture in SC-SOFC has various advantages. It is not necessary to process for the gas tight sealing by exposure of all components in the same gas condition [73]. In addition, since the cell is located in one gas compartment, several complex gas manifolds and flow structures for gas supply can be eliminated, making it possible to create a simpler and more compact cell [75]. It also becomes acceptable to have thin electrolyte layers with defects, small cracks and pores. Moreover, the effect of exothermic fuel oxidation reaction during the operation can help increase the cell temperature, enhancing the activation of gas reaction by up to 100℃ [76]. This heat release can lead to an improvement of power density at lower temperatures. A major drawback of SC-SOFCs is the low fuel utilisation and cell efficiency from insufficient selectivity of materials in the mixture gas condition. Another problem with the fuel-air gas mixture is the risk of explosion at high operating temperatures [77]. It must also be taken into account that the gas ratio and reactions can lead to low efficiency due to parasitic, non-electrochemical reactions.

Despite these disadvantages, SC-SOFCs exhibit several advantages over DC-SOFCs, making them an interesting alternative to overcome problems of DC-SOFCs.

Table 2.1 Advantages and disadvantages of SC-SOFCs

Advantages	Disadvantages
- Sealing-free structure	- Highly selective and catalytically active materials necessary
- Less complex gas manifolding	
- Simplified design	- Low efficiency and fuel utilisation than DC-SOFCs
- Easier fabrication	
- Novel cell designs	- Risk of explosion for fuel-air mixtures at high temperatures
- Easier stack assembly	

Fuel-air mixtures

For the electrochemical reactions of SC-SOFCs, partial fuel oxidation is desirable, whereas the complete fuel oxidation is not desirable. SC-SOFCs enable to use hydrocarbon gas as well as pure hydrogen. The use of a mixture of hydrocarbon and air allows for an internal hydrocarbon reforming process over a metal-based anode catalyst with the addition of steam. By chemical reaction with gases inside the chamber, hydrocarbon fuel, water, and carbon monoxide act each other and help to generate hydrogen gas for electrochemical reaction. However, carbon particles directly from hydrocarbon fuel might prevent catalysts from activating with fuel gas and reduce cell performance. It is possible to control the carbon deposition that may occur in this reforming process by adjustments of the oxygen content in the gas mixture [78].

$$CH_4 + \frac{1}{2}O_2 \rightarrow CO + 2H_2$$

$$CH_4 + O_2 \rightarrow CO + H_2 + H_2O$$

$$CO + O^{2-} \rightarrow CO_2 + 2e^-$$
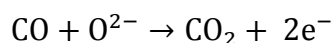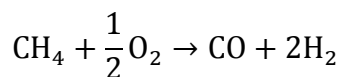
Furthermore, the water gas shift reaction converts CO into H_2, which is more easily electrochemically oxidized that CO.

$$CO + H_2O \rightarrow H_2 + CO_2$$
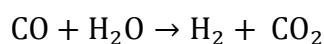
In the partial oxidation of the fuel, the anode needs to be active and selective and the cathode should not activate with any fuel reactions. Nickel-based catalysts exhibited excellent activity for processing the partial oxidation of methane within the mixture of methane and oxygen [79]. Also, Nickel was found to be active for methane cracking. In this respect, carbon deposition on the anode layer in an oxygen lean gas mixture can lead to deactivation of the catalyst. It has a negative impact, leading to low performance and reduction in long-term stability of the system. Also the ratio of methane to oxygen (Rmix) ≤2 is recommended to avoid carbon formation [80]. In general, a mixture of methane and oxygen is used with Rmix between 0.85 and 2 [73].

Various Cell Designs

The SC-SOFCs configurations are summarised in Fig 2.7 for planar anode-supported cells, planar electrolyte-supported cells, planar cathode-supported cells, fully-porous cells and co-planar cells. Planar anode-, electrolyte-, and cathode-supported cells are also used in conventional DC-SOFCs, whereas fully-porous and co-planar cells are only possible under SC-SOFCs.

Some researchers in the field of SC-SOFC have introduced and SC-SOFC is mainly divided into 4 types of cell structure. These are the planar (anode supported, electrolyte supported), tubular, co-planar and fully porous types. The first SC-SOFC was operated by Hibino et al. in 1993 [81] using a mixture of methane and air (Rmix=2) at 950℃. As a typical planar electrolyte supported type of SC-SOFC, it consisted of a Ni-YSZ (Nickel - Yttria Stabilized Zirconia) anode layer, an YSZ (Yttria Stabilized Zirconia) electrolyte and Au cathode layer and it obtained a maximum power density of 2.36mW/cm^2. The performance was later improved by the use of a mixed ionic conductor barium-based electrolyte [82]. As a result, the power output was increased to 170mW/cm^2 at 950℃. However the barium-based electrolyte fabrication method had some instability disadvantages and reacted with carbon dioxide, resulting in the prevention of long-term operation.
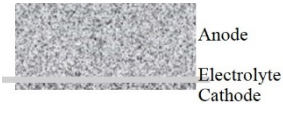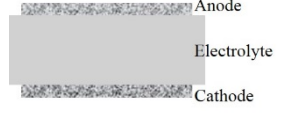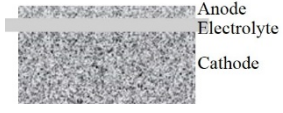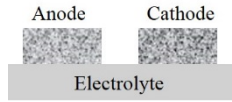
Type	Features
1. Anode supported cell	- Most popular - Need thick anode for strength - Reduce ohmic cell resistance
2. Electrolyte supported cell	- Need thick electrolyte for strength - Increase of ohmic loss
3. Cathode supported cell	- Lower cost and higher reliability - Lower power density than those of anode-supported types
4. Co-planar cell	- Dual-face design with side-by-side electrode pattern - Ohmic loss by gap size between adjacent anodes and cathodes
5. Flow by or Flow though cell	- Consist of porous structures enabling surface ionic conduction - Enhance mass transport

Figure 2.7 Designs of SC-SOFCs

In 1999, Hibino had researched an electrolyte supported SC-SOFC that consisted of Ni in anode, YSZ electrolyte and LSM cathode [83]. This cell showed much better performance rather than that of the Pt anode and Au cathode. It was attributed to the addition of MnO_2 in the cathode, leading to a decrease in electrode overpotentials and reaction resistance. In the following year, the cell performance with electrolyte of Strontium-doped Samarium Cobaltite (SSC), Lanthanum Strontium Cobalt Oxide (LSC) and Lanthanum Strontium Manganite (LSM) was studied between 350 and 900℃ in flowing mixtures of methane, ethane, propane or liquefied petroleum gas and air, where their oxidation proceeded safely without explosion [84]. It was found that a small electrode reaction resistance resulted in an increase in power density and the power density at 600℃ increased with decreasing electrolyte thickness. Among the fuel gas, excluding methane, ethane showed the best performance

and ethanol the worst. This work confirmed that the problem with transportation applications due to operation conditions at high temperatures could be settled using highly conductive solid electrolyte materials with the use of readily available hydrocarbon fuels.

To obtain high performance of the anode layer in a mixture of methane and air, Rmix=1 at reduced temperature, Samaria doped Ceria (SDC) added to nickel with palladium, and the cell consisted of a Ni-SDC anode, SDC electrolyte, SSC cathode at 550℃ [85]. The addition of a small amount of Pd to the anode promoted the partial oxidation of methane by oxygen to form hydrogen and carbon monoxide, resulting in small resistance between electrode and the reaction of anode. When using a 0.15mm thickness of SDC electrolyte, the peak power output was 644mW/cm^2 at 550℃. As the electrolyte material substituted SDC for YSZ and added a little Pd to enhance performance of anode, a high power density could be observed in spite of low temperature operation.

In 2005, Hibino's group introduced electrolyte material, BaLaIn$_2$O (BLI), which exhibited higher oxide ion conductivity than YSZ [86]. It consisted of a Nickel - Lanthanum Strontium Manganese Chromite (Ni-LSCM) anode, BLI electrolyte and SSC cathode. In a mixture of methane and air, the obtained output was 64.7mW/cm2 at 800℃. Based on results recorded over many years, SC-SOFC was examined as an energy recovery module for application on a motorcycle, as shown in Figure 2.8 [87]. The cell consisted of Ni + SDC anode, YSZ electrolyte and LSM cathode. Fuel gas derived from the engine exhaust was included with mixtures of 1000ppm CH$_4$, 1000ppm C$_2$H$_6$, 1000ppm C$_3$H$_8$, 1000ppm CH$_4$ and 1250ppm O$_2$ and was supplied to the cell at 700℃. The maximum power density was 12mW/cm$_2$. This work demonstrated that although its output was low, an SC-SOFC is capable of operating with exhaust gas from a gasoline engine.

(a) Composition of the single cell | (b) Application on bike
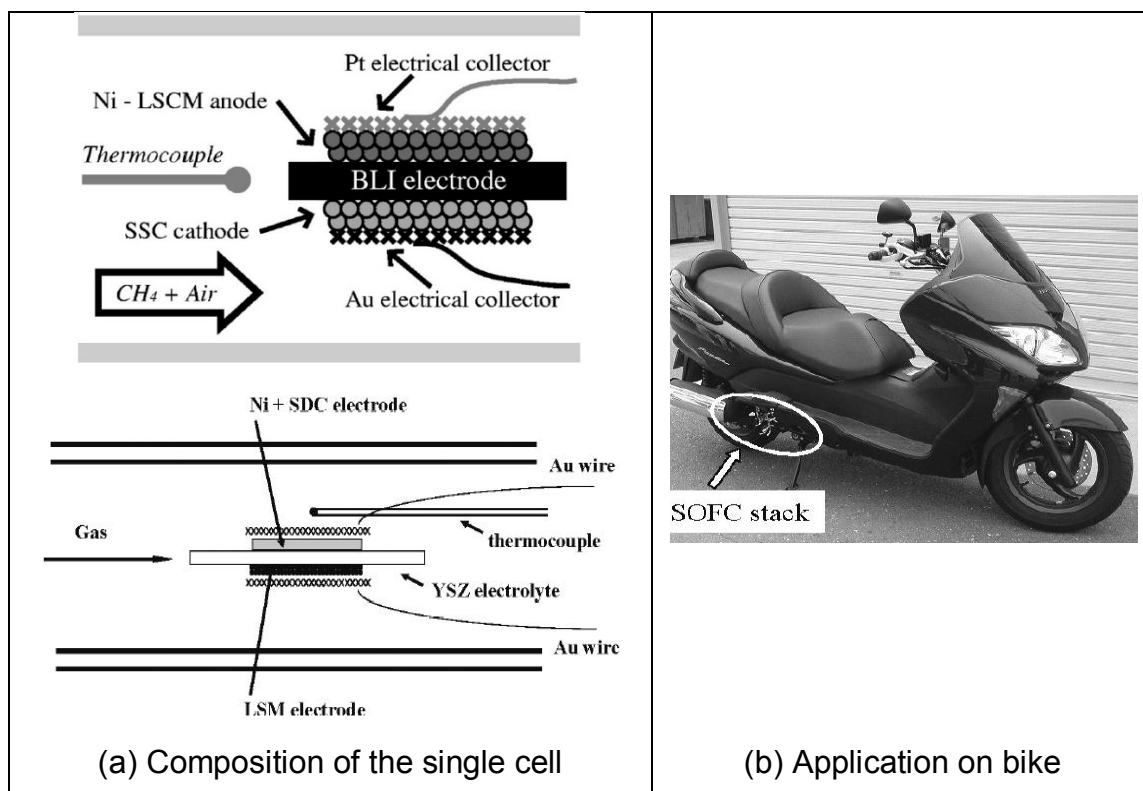
Figure 2.8 Concept of SC-SOFC in Hibino's research group

Buergler et al. [88] investigated the effects of different flow rates with doped Pd, Co in the condition of Pt-meshes that were embedded in electrode as current collectors in order to achieve low overpotential using Gadolinium-Doped Ceria (GDC) composition. In a mixture of methane and air (Rmix=1.6), the cell generated a maximum power density of 468mW/cm^2 at 600℃. It was confirmed that the power output was higher when much higher flow rates were used. Also, the use of Co doped electrolyte as well as the Pd doped anode led to improve high OCVs. Through this research, it should be considered that the effect of the addition of Pd, Co, etc. in the anode could enhance the reaction and lessen the resistance in the methane-air mixture.

As an anode supported type of SC-SOFC, Shao et al. [74] researched the thermally self-sustained micro SOFC, operating with propane fuel at 600℃. A thin film electrolyte cell was fabricated using SDC for the electrolyte, Ni + SDC for the anode, and a mixture of SDC with Barium Strontium Cobalt Ferrite (BSCF) for the cathode. Here, the addition of a porous layer with a little amount of Ruthenium (Ru) + Cerium (Ce) was coated onto the anode surface as a catalyst, to enhance catalysis of propane partial oxidation at lower temperature.

The application of the Ru + Ce layer was found to affect thermal stability and increase the conversion rate for fuel oxidation as opposed to than that of the Ni-SDC layer without the Ru + Ce layer. On top of that, in the case of the Ru + Ce treated cell, carbon deposition was not found to occur on the Ni beneath the catalyst layer, suggesting that the Ru + Ce layer was active, and the partial oxidation was completed with an exterior layer where the propane was unable to reach into the inner Ni + SDC layer.
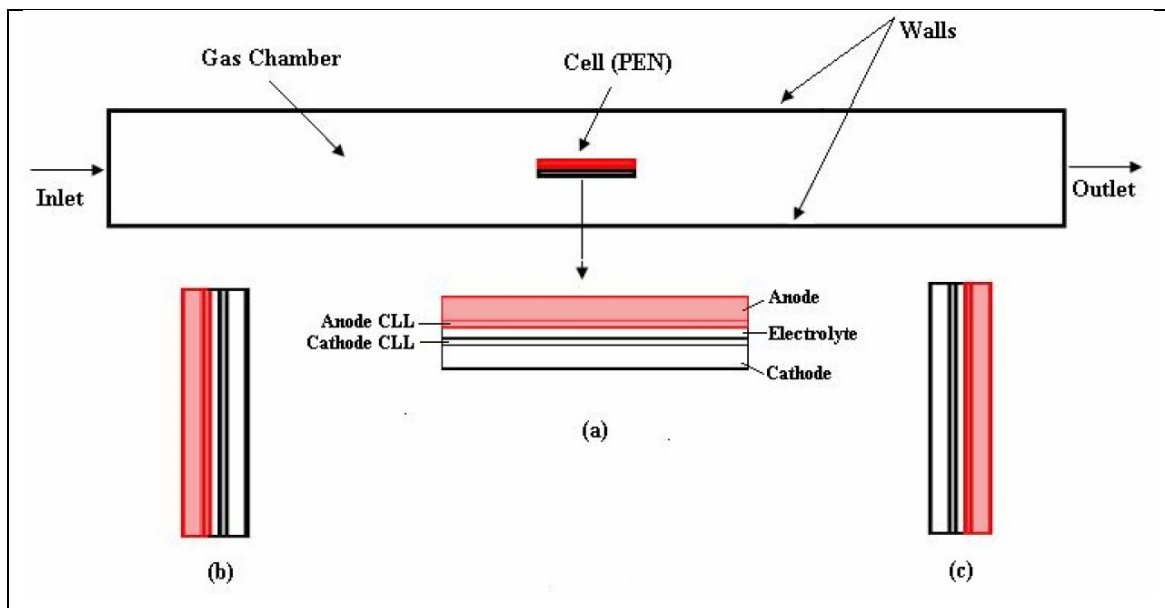
Figure 2.9 Schematic diagram of SC-SOFCs

In Fig 2.9, Naveed Akhtar et al. [89] have discussed the gas flow distribution and fuel utilisation in SC-SOFC, comparing the parallel and perpendicular flow directions with respect to the cell component, using an electrochemical fluid coupled numerical model in a five-layer assembly (anode/anode catalyst layer/dense electrolyte/cathode catalyst layer/cathode). The velocity profile showed that increasing the velocity enhanced the mass transport in the cell. This was due to forced convection and this could help to decrease diffusion losses at higher current density. As a porosity effect with the velocity profile, it was shown that low porosity provided a more active reaction area and increased residence time, contributing to improve the fuel utilisation. With the result of gas concentration depending on flow direction toward the cell, a large uniform concentration gradient was obtained in the perpendicular compared to the parallel direction. As a result of types such as parallel, anode

first perpendicular and cathode first perpendicular configurations, it was found that the perpendicular types of the cell against flow direction provided better reactant utilisation than the parallel type. In addition, the cathode first perpendicular type demonstrated the best utilisation of both electrodes. All things considered, if fully porous layers were used as a cathode first perpendicular condition, this would take advantage of both the gas flow and the electrochemical performance of the cell.

N. Akhtar et al. [90] suggested a micro tubular SC-SOFC, utilising a mixed reactant supply. This was operated with a mixture of methane and air (Rmix=1) at 750℃ with a comparison of various mixture ratios. As a comparison of effective fuel utilisation and efficiency depending on the gas ratio from Rmix=1 to 4, the lower the hydrocarbon content, the higher the efficiency. Also, in the condition of identical Rmix=1, the more gas supplied, the lower the efficiency obtained, until 700℃, after which the efficiency increases with the amount of gas supplied. In order to improve fuel utilisation and efficiency, the cell has to be operated in stacks. However, cell degradation began to show within 24 hours due to redox cycles over the nickel surface, having an adverse effect on the long-term performance. To prevent cell degradation during the redox cycles, the addition of Pd and Ru in the anode layer could be considered.

a) Co-planar SOFC

J. Fleig et al. [91] introduced a geometrical constraint of co-planar SOFC, where both electrodes are located on one side of a thin film electrolyte with 10 μm thickness. Through numerical calculation, electrode geometries and film thickness were obtained to achieve considerably low polarisation resistance. Interdigitated electrodes with a characteristic size were found to be essential for reaching low polarisation resistance. It was shown that in the co-planar type the ionic current has to flow parallel to the substrate, so that the distance and width of the electrodes become more important than the thin electrolyte which is favourable in terms of reducing ohmic resistance. It was also mentioned that the current was restricted to the vicinity of the electrochemically active area of the electrodes, and hence electrode morphology would be a more critical factor

with respect to the electrolyte resistance. Although, with an interdigitated structure, the electrode distance between the anode and cathode has to be drastically reduced to achieve low resistance, the distance becoming too small might cause a problem if the reaction product in the anode layer flows easily to the nearby cathode, thus changing the mixed cathode potential and making it unstable for an electrochemical reaction. In this study, the optimal value was examined to achieve low resistance. The resistance was stable and low when it was applied in a 2 ~ 20μm of specimen width, 0.8μm of electrolyte thickness and 2μm of specimen distance.
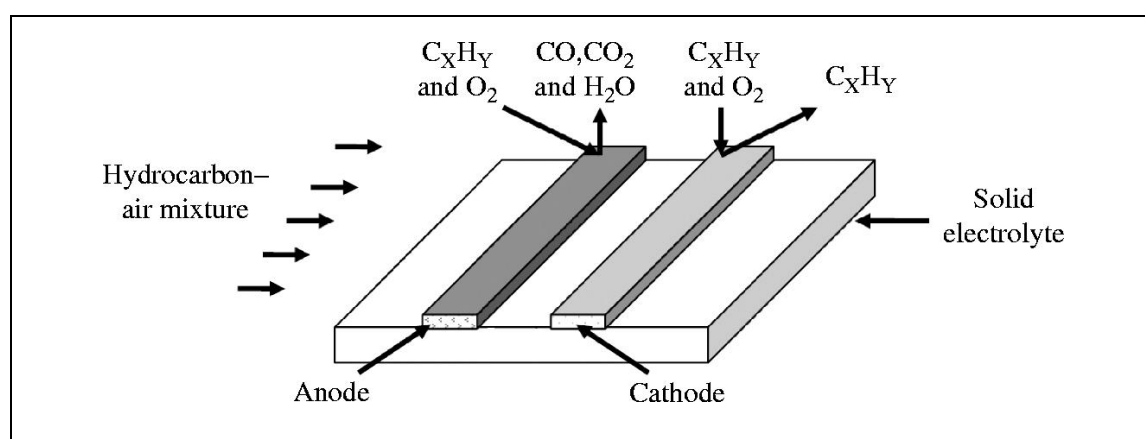
Figure 2.10 Concept of Co-planar SOFC

Ahn et al. [92] carried out co-planar SC-SOFC experiments with micro-patterned electrodes, as shown in Figure 2.10. In order to fabricate linearly patterned electrode structures on the same surface, a robo-dispensing method was used. This means that paste materials of anode and cathode were deposited onto a substrate of electrolyte by extrusion through a syringe nozzle. All variables were restricted except for the distance between electrodes as well as the power density, which was measured in a mixture of methane and air at 900°C. The distances between the anode and cathode were varied, at 255μm, 443μm and 783μm, and the corresponding power densities were achieved at 804mW/cm^2, 790mW/cm^2 and 782mW/cm^2, respectively. A comparison of multiple pairs with interdigitated electrodes was also investigated. The OCV with 2, 4 and 8 pairs was continuously decreased and a voltage drop was observed compared to the single electrode pair. This was attributed to flow geometry depending on electrode pairs affecting the output, where mixing

gases between reactant and product was influenced by convection flow or turbulence flow. In an ideal SC-SOFC, the partial oxidation of the methane has to react only on the anode, while oxygen should be reduced only on the cathode. The selective partial oxidation and reduction induce a difference in the oxygen partial pressure between the anode and the cathode. As the results of this work show, it is difficult to maintain pressure difference in the flowing of the cell.

b) Micro SC-SOFCs

Liu et al. [93] investigated micro SC-SOFC stacks with two series-wound single cells. In this research, the effects of flow rate, gas composition and furnace temperature were examined on the performance of both the single and the stack cell. It was shown that the maximum power output is about 370mW with Rmix=1. We can expect the possibility of applying the performance of these micro stacks for portable applications.

A flow-by type of fully porous SC-SOFC was investigated by Toshio et al [94]. This cell consisted of porous anode and cathode layers as well as a porous electrolyte; enabling reactant gases to flow through the whole assembly, as shown in Figure 2.11 (a). It was located in parallel toward the flow direction in a mixture of methane and air (Rmix=1) with various flow rates. It was discovered that the cell temperature was higher than the furnace set temperature due to the exothermic reaction during operation. At a cell temperature of 744$°C$, the maximum power density obtained was 660mW/cm^2. The OCV with the porous electrolyte was lower compared with the dense electrolyte in the same operating conditions. This was attributed to the reduction of oxygen partial pressure, which was due to the permeability of porous electrolyte from anode to cathode so that oxygen could react with hydrogen or carbon oxide gas at the cathode, resulting in a lower oxygen partial pressure. It was demonstrated that increasing the gas flow rate resulted in improvement of reactant diffusion through the electrode. Resistances could thereby be reduced and the OCV increased.

I. Riess [95] studied the flow-through type of fully porous SC-SOFCs to make a comprehensive survey of variables such as geometry, materials, temperature and overall reaction, shown in Figure 2.11 (b). The advantages of the flow-through type are that it is simple and much less expensive to construct than the conventional type, rendering it economically feasible. It provides a high energy density and fuel utilisation. Also, it enhances the reaction of the gas mixture with the correct catalytic activities and selectivity. Experimentally, the flat stack of the flow-through type was fabricated without an interconnector, consisted of 17 elements (one element is an assembly of an anode/electrolyte/cathode). As regards thickness of layers, it was noted that a minimum thickness should be at least 10μm in a layer to prevent contact between the anode and the cathode through the pores in the electrolyte.

The role of the interconnector was defined as a separation of the adjacent layer, eliminating the possibility that the material contact between the two electrodes could occur when stacking with single cells. With regards to material features, the possibility that catalytic property could be changed by product adsorption on reaction area or reactions through changing concentration ratio should be taken into account, as should maintenance of selectivity during the steam- or CO_2 reforming process, and danger of explosion.
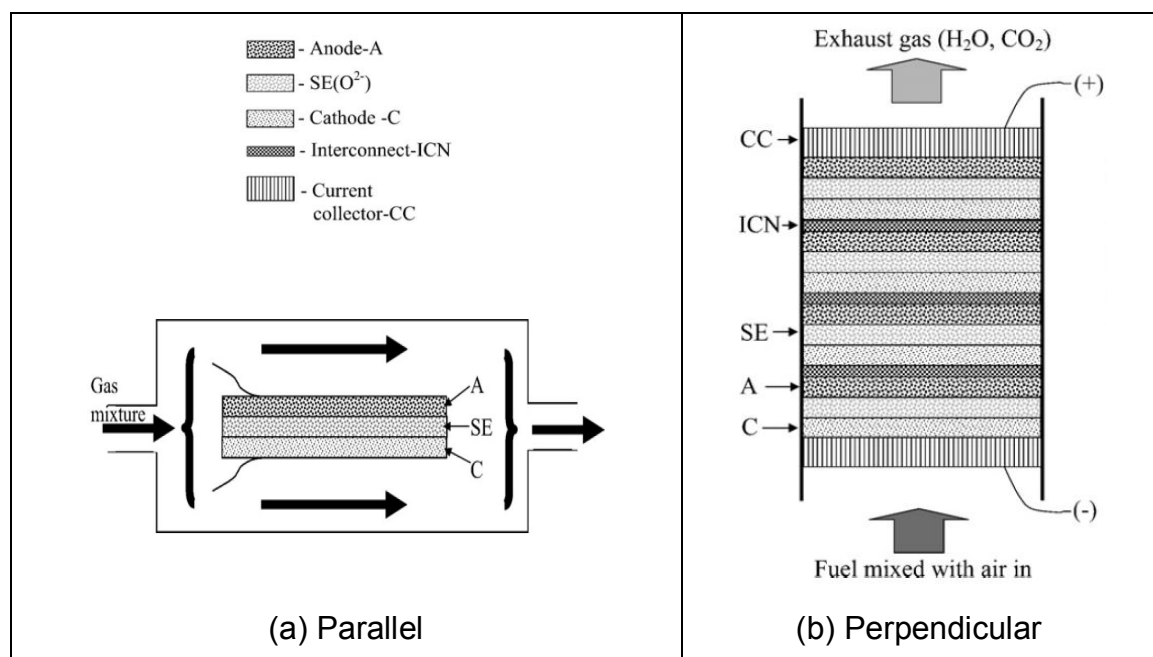

Figure 2.11 Fully porous SOFC compositions of (a) parallel and (b) perpendicular

Applicability of wavy structure using the co-sintering process

It should be necessary to discuss how to control induced stresses acting as a useful or detrimental component in a ceramic multilayer structure, so as to obtain desired shapes after the co-sintering process. The dimensional change from induced stress has a deleterious effect in the field of low temperature co-fired ceramics (LTCC), whereas the additional stresses occurring during co-sintering have a positive effect for wavy multilayer structures without external load. The investigations of Shin et al [96] have shown the way in which generated stress during co-sintering develops in the active region of the structure for the application of the ceramic capacitor. It can thereby be proved that a compressive in-plane stress component is beneficial. Likewise, for wavy forming, the effect of dissimilarities such as the initial density, particle size, and thermal expansion coefficient should be considered for different sintering behaviours between materials, since influences derived from induced stresses increase as the number of layers in the structure increases.

Some studies have raised the possibility for fabrication of wavy multilayer structures using thermally induced stress during co-sintering [97-99]. These predict that the volumetric shrinkage in response to densification and viscosity during sintering, as well as curvature due to gravity, can lead the state of a ceramic body to become flexible, achieving a wavy-shaped multilayer structure. The first task in creating a wavy structure would be to find the active temperature range at which the viscosity of the ceramic layers is at a minimum, while curvature is more active.

On the condition that a sintered ceramic structure is exposed at high temperature in a redox cycle — particularly in a SOFC operation — the effect of thermally induced stress during operation may repeatedly influence the dimensions of the multilayer structure even though there is little impact for dimensional change, as compared with the value occurred during sintering [100, 101].

As the wavy structure derives from the deformation caused by the sintering process, it has the advantage of having a large active surface area as a field for electrochemical reactions. Unlike a plain structure with the same radius, this can be utilised as a wavy cell in a SOFC field. The effective use of a

wavy multilayer structure may be applicable to a SC-SOFC, which needs a high electrochemical reaction area due to the use of gas mixture in SOFC types [102]. Although the reduction of length in the creation of the waves leaded to increase its height, geometric projected area was regarded as an effective electrochemical reaction area to compare features of cells in this study. For further investigations, it should be considered how volumetric structures affect the performance with features such as gas flow behaviour, fuel utilisation, and microscopic structure.

References

[1] BORDIA, R.K. and SCHERER, G.W., 1988. On constrained sintering—I. Constitutive model for a sintering body. Acta metallurgica, 36(9), pp. 2393-2397.

[2] ATKINSON, A., KIM, J., RUDKIN, R., TAUB, S. and WANG, X., 2011. Stress Induced by Constrained Sintering of 3YSZ Films Measured by Substrate Creep. Journal of the American Ceramic Society, 94(3), pp. 717-724.

[3] KIM, J., RUDKIN, R.A., WANG, X. and ATKINSON, A., 2011. Constrained sintering kinetics of 3YSZ films. Journal of the European Ceramic Society, 31(13), pp. 2231-2239.

[4] WANG, X., KIM, J. and ATKINSON, A., 2012. Constrained sintering of 8 mol% Y2O3 stabilised zirconia films. Journal of the European Ceramic Society, 32(16), pp. 4121-4128.

[5] BORDIA, R.K. and SCHERER, G.W., 1988. On constrained sintering—II. Comparison of constitutive models. Acta Metallurgica, 36(9), pp. 2399-2409.

[6] BORDIA, R.K. and SCHERER, G.W., 1988. On constrained sintering—III. Rigid inclusions. Acta Metallurgica, 36(9), pp. 2411-2416.

[7] RAJ, R., 1987. Analysis of the Sintering Pressure. Journal of the American Ceramic Society, 70(9), pp. C-210-C-211.

[8] MOHANRAM, A., LEE, S.H., MESSING, G.L. and GREEN, D.J., 2005. A novel use of constrained sintering to determine the viscous Poisson's ratio of densifying materials. Acta materialia, 53(8), pp. 2413-2418.

[9] HSUEH, C. and EVANS, A., 2006. Residual stresses in meta/ceramic bonded strips. Journal of the American Ceramic Society, 68(5), pp. 241-248.

[10] HSUEH, C., 2002. Thermal stresses in elastic multilayer systems. Thin Solid Films, 418(2), pp. 182-188.

[11] SHI, J., 1999. Relation between coarsening and densification in solid-state sintering of ceramics: experimental test on superfine zirconia powder compacts. Journal of Materials Research, 14(04), pp. 1389-1397.

[12] MALZBENDER, J., 2004. Mechanical and thermal stresses in multilayered materials. Journal of Applied Physics, 95(4), pp. 1780-1782.

[13] LI, F., PAN, J., GUILLON, O. and COCKS, A., 2010. Predicting sintering deformation of ceramic film constrained by rigid substrate using anisotropic constitutive law. Acta Materialia, 58(18), pp. 5980-5988.

[14] Bhushan, Bharat; Shi, Z.-C. (2006). Handbook of Nanotechnology. Springer.

[15] COCKS, A.C.F., GILL, S. and PAN, J., 1998. Modeling microstructure evolution in engineering materials. Advances in Applied Mechanics, 36, pp. 81-162.

[16] KLEIN, C.A., 2000. How accurate are Stoney's Equation and recent modifications. Journal of Applied Physics, 88(9), pp. 5487-5489.

[17] HU, Y. and HUANG, W., 2004. Elastic and elastic-plastic analysis of multilayer thin films: Closed-form solutions. Journal of Applied Physics, 96(8), pp. 4154-4160.

[18] ZHANG, Y. and ZHAO, Y., 2006. Applicability range of Stoney's formula and modified formulas for a film/substrate bi-layer. Journal of Applied Physics, 99(5), pp. 053513-053513-7.

[19] N. SCHWARZER, On the determination of film stress from substrate bending: Stoney's formula and its limits.

[20] TING, J. and LIN, R., 1994. Effect of particle-size distribution on sintering. Journal of Materials Science, 29(7), pp. 1867-1872.

[21] MA, J. and LIM, L., 2002. Effect of particle size distribution on sintering of agglomerate-free submicron alumina powder compacts. Journal of the European Ceramic Society, 22(13), pp. 2197-2208.

[22] SIMCHI, A., 2006. Densification and microstructural evolution during co-sintering of Ni-base superalloy powders. Metallurgical and Materials Transactions A, 37(8), pp. 2549-2557.

[23] STONEY, G.G., 1909. The tension of metallic films deposited by electrolysis. Proceedings of the Royal Society of London.Series A, Containing Papers of a Mathematical and Physical Character, 82(553), pp. 172-175.

[24] HUANG, Y. and ROSAKIS, A., 2007. Extension of stoney's formula to arbitrary temperature distributions in thin film/substrate systems. Journal of Applied Mechanics, 74(6), pp. 1225-1233.

[25] JANSSEN, G., ABDALLA, M., VAN KEULEN, F., PUJADA, B. and VAN VENROOY, B., 2009. Celebrating the 100th anniversary of the Stoney equation for film stress: Developments from polycrystalline steel strips to single crystal silicon wafers. Thin Solid Films, 517(6), pp. 1858-1867.

[26] TOWNSEND, P., BARNETT, D. and BRUNNER, T., 1987. Elastic relationships in layered composite media with approximation for the case of thin films on a thick substrate. Journal of Applied Physics, 62(11), pp. 4438-4444.

[27] KLEIN, C.A., 2000. How accurate are Stoney's equation and recent modifications. Journal of Applied Physics, 88(9), pp. 5487-5489.

[28] BLECH, I.A., BLECH, I. and FINOT, M., 2005. Determination of thin-film stresses on round substrates. Journal of Applied Physics, 97(11), pp. 113525.

[29] SCHERER, G.W., 1979. Sintering inhomogeneous glasses: application to optical waveguides. Journal of Non-Crystalline Solids, 34(2), pp. 239-256.

[30] CAI, P.Z., MESSING, G.L. and GREEN, D.J., 1997. Determination of the mechanical response of sintering compacts by cyclic loading dilatometry. Journal of the American Ceramic Society, 80(2), pp. 445-452.

[31] CAI, P.Z., GREEN, D.J. and MESSING, G.L., 1997. Constrained densification of alumina/zirconia hybrid laminates, II: viscoelastic stress computation. Journal of the American Ceramic Society, 80(8), pp. 1940-1948.

[32] BORDIA, R.K., ZUO, R., GUILLON, O., SALAMONE, S.M. and RÖDEL, J., 2006. Anisotropic constitutive laws for sintering bodies. Acta materialia, 54(1), pp. 111-118.

[33] FENG, X., HUANG, Y., JIANG, H., NGO, D. and ROSAKIS, A.J., 2006. The effect of thin film/substrate radii on the Stoney formula for thin film/substrate subjected to non-uniform axisymmetric misfit strain and temperature. J.Mech.Mater.Struct, 1(6), pp. 1041-1053.

[34] FENG, X., HUANG, Y. and ROSAKIS, A., 2007. On the stoney formula for a thin film/substrate system with nonuniform substrate thickness. Urbana, 51, pp. 61801.

[35] CHIU, C.C., 1992. Residual stresses in ceramic coatings as determined from the curvature of a coated strip. Materials Science and Engineering: A, 150(1), pp. 139-148.

[36] DREIER, G. and SCHMAUDER, S., 1993. T-stress related to thermal residual stresses in bimaterials. Scripta metallurgica et materialia, 28, pp. 103-103.

[37] ZHANG, X., XU, B. and XUAN, F., 2008. Residual stresses in the elastoplastic multilayer thin film structures: The cases of Si/Al bi-layer and Si/Al/SiO trilayer structures. Journal of Applied Physics, 103, pp. 073505.

[38] ATKINSON, A., KIM, J.S., RUDKIN, R., TAUB, S. and WANG, X., 2011. Stress induced by constrained sintering of 3YSZ films measured by substrate creep. Journal of the American Ceramic Society, 94(3), pp. 717-724.

[39] CORBIN, S.F. and APTÉ, P.S., 1999. Engineered porosity via tape casting, lamination and the percolation of pyrolyzable particulates. Journal of the American Ceramic Society, 82(7), pp. 1693-1701.

[40] CORBIN, S.F., LEE, J. and QIAO, X., 2001. Influence of green formulation and pyrolyzable particulates on the porous microstructure and sintering characteristics of tape cast ceramics. Journal of the American Ceramic Society, 84(1), pp. 41-47.

[41] BOARO, M., VOHS, J. and GORTE, R., 2003. SYNTHESIS OF HIGHLY POROUS YTTRIA-STABILISED ZIRCONIA BY TAPE-CASTING METHODS. J.Am.Ceram.Soc., 86(3), pp. 395-400.

[42] HSU, R.T. and JEAN, J.H., 2005. Key Factors Controlling Camber Behavior During the Cofiring of Bi-Layer Ceramic Dielectric Laminates. Journal of the American Ceramic Society, 88(9), pp. 2429-2434.

[43] COLOGNA, M., SGLAVO, V.M. and BERTOLDI, M., 2010. Sintering and Deformation of Solid Oxide Fuel Cells Produced by Sequential Tape Casting. International Journal of Applied Ceramic Technology, 7(6), pp. 803-813.

[44] LEE, S.H., MESSING, G.L. and GREEN, D.J., 2004. Warpage evolution of screen printed multilayer ceramics during co-firing. Key Engineering Materials, 264, pp. 321-330.

[45] ATKINSON, A. and SELCUK, A., 1999. Residual stress and fracture of laminated ceramic membranes. Acta materialia, 47(3), pp. 867-874.

[46] BUSSO, E.P., TKACH, Y. and TRAVIS, R.P., 2001. Thermally induced failure of multilayer ceramic structures. Philosophical Magazine A, 81(8), pp. 1979-1995.

[47] SØRENSEN, B.F. and HORSEWELL, A., 2001. Crack growth along interfaces in porous ceramic layers. Journal of the American Ceramic Society, 84(9), pp. 2051-2059.

[48] CHEN, K.S. and OU, K.S., 2002. Modification of curvature-based thin-film residual stress measurement for MEMS applications. Journal of Micromechanics and Microengineering, 12(6), pp. 917-924.

[49] HUANG, S. and ZHANG, X., 2006. Extension of the Stoney formula for film–substrate systems with gradient stress for MEMS applications. Journal of Micromechanics and Microengineering, 16(2), pp. 382-389.

[50] KIANI, S., PAN, J., YEOMANS, J.A., BARRIERE, M. and BLANCHART, P., 2007. Finite element analysis of sintering deformation using densification data instead of a constitutive law. Journal of the European Ceramic Society, 27(6), pp. 2377-2383.

[51] ZUO, R., AULBACH, E. and RÖDEL, J., 2003. Experimental determination of sintering stresses and sintering viscosities. Acta materialia, 51(15), pp. 4563-4574.

[52] ZUO, R., AULBACH, E. and RODEL, H., 2004. Shrinkage-free sintering of low-temperature cofired ceramics by loading dilatometry. Journal of the American Ceramic Society, 87(3), pp. 526-528.

[53] CARDONA, C.G., TIKARE, V., PATTERSON, B.R. and OLEVSKY, E., 2012. On Sintering Stress in Complex Powder Compacts. Journal of the American Ceramic Society, 95(8), pp. 2372-2382.

[54] CHU, M.Y., DE JONGHE, L.C. and RAHAMAN, M.N., 1989. Effect of temperature on the densification/creep viscosity during sintering. Acta metallurgica, 37(5), pp. 1415-1420.

[55] JØRGENSEN, M., PRIMDAHL, S., BAGGER, C. and MOGENSEN, M., 2001. Effect of sintering temperature on microstructure and performance of LSM–YSZ composite cathodes. Solid State Ionics, 139(1), pp. 1-11.

[56] MOHANRAM, A., MESSING, G.L. and GREEN, D.J., 2005. Densification and Sintering Viscosity of Low‐Temperature Co‐Fired Ceramics. Journal of the American Ceramic Society, 88(10), pp. 2681-2689.

[57] ZENG, P., RAN, R., CHEN, Z., GU, H., SHAO, Z., DINIZ DA COSTA, J. and LIU, S., 2007. Significant effects of sintering temperature on the performance of La0. 6Sr0. 4Co0. 2Fe0. 8O3-delta oxygen selective membranes. Journal of Membrane Science, 302(1-2), pp. 171-179.

[58] RHODES, W., 1981. Agglomerate and Particle Size Effects on Sintering Yttria‐Stabilized Zirconia. Journal of the American Ceramic Society, 64(1), pp. 19-22.

[59] LENG, Y.J., CHAN, S.H., KHOR, K.A., JIANG, S.P. and CHEANG, P., 2003. Effect of characteristics of Y2O3/ZrO2 powders on fabrication of anode-supported solid oxide fuel cells. Journal of Power Sources, 117(1), pp. 26-34.

[60] ABE, H., NAITO, M., SATO, K. and KINOSHITA, T., 2010. Nanostructured LSM/YSZ cathode for intermediate temperature solid oxide fuel cells. Transactions of JWRI, 39(1), pp. 65-68.

[61] CHRISTENN, C. and ANSAR, S.A., 2011. Constrained and Non-Constrained Sintering of Plasma-Sprayed Zirconia Based Electrolytes for SOFCs. Advances in Science and Technology, 65, pp. 263-268.

[62] VARELA, J., WHITTEMORE, O. and LONGO, E., 1990. Pore size evolution during sintering of ceramic oxides. Ceramics International, 16(3), pp. 177-189.

[63] KIM, B.N., HIRAGA, K. and MORITA, K., 2005. Viscous grain-boundary sliding and grain rotation accommodated by grain-boundary diffusion. Acta materialia, 53(6), pp. 1791-1798.

[64] ZAVALIANGOS, A., MISSIAEN, J. and BOUVARD, D., 2006. Anisotropy in shrinkage during sintering. Science of Sintering, 38(1), pp. 13-25.

[65] GUILLON, O., WEILER, L. and RÖDEL, J., 2007. Anisotropic Microstructural Development During the Constrained Sintering of Dip‐Coated Alumina Thin Films. Journal of the American Ceramic Society, 90(5), pp. 1394-1400.

[66] HOTZA, D. and GREIL, P., 1995. Review: aqueous tape casting of ceramic powders. Materials Science and Engineering: A, 202(1), pp. 206-217.

[67] NAYAK, S., SINGH, B.P., BESRA, L., CHONGDAR, T.K., GOKHALE, N. and BHATTACHARJEE, S., 2011. Aqueous Tape Casting Using Organic Binder: A Case Study with YSZ. Journal of the American Ceramic Society, 94(11), pp. 3742-3747.

[68] NICHOLAS, J.D. and DE JONGHE, L.C., 2007. Prediction and evaluation of sintering aids for Cerium Gadolinium Oxide. Solid State Ionics, 178(19), pp. 1187-1194.

[69] MORI, M., HIEI, Y. and SAMMES, N.M., 2000. Sintering behavior of Ca- or Sr-doped LaCrO3 perovskites including second phase of AECrO4 (AE= Sr, Ca) in air. Solid State Ionics, 135(1), pp. 743-748.

[70] CHIANG, M.J., JEAN, J.H. and LIN, S.C., 2011. The Effect of Anisotropic Shrinkage in Tape‐Cast Low‐Temperature Cofired Ceramics on Camber Development of Bi-layer Laminates. Journal of the American Ceramic Society, 94(3), pp. 683-686.

[71] LI, W., FEINGOLD, A., PALANISAMY, P. and LORENZ, G., 2012. Co‐sintering Zirconia Electrolyte and Insulator Tapes for Sensor Applications. Journal of the American Ceramic Society, 95(12), pp. 3815-3820.

[72] HELLE, A., EASTERLING, K.E. and ASHBY, M., 1985. Hot-isostatic pressing diagrams: new developments. Acta Metallurgica, 33(12), pp. 2163-2174.

[73] NAPPORN, T.W., JACQUES-BÉDARD, X., MORIN, F. and MEUNIER, M., 2004. Operating conditions of a single-chamber SOFC. Journal of the Electrochemical Society, 151, pp. A2088.

[74] SHAO, Z., HAILE, S.M., AHN, J., RONNEY, P.D., ZHAN, Z. and BARNETT, S.A., 2005. A thermally self-sustained micro solid-oxide fuel-cell stack with high power density. Nature, 435(7043), pp. 795-798.

[75] NAPPORN, T.W., MORIN, F. and MEUNIER, M., 2004. Evaluation of the actual working temperature of a single-chamber SOFC. Electrochemical and solid-state letters, 7, pp. A60.

[76] HAO, Y. and GOODWIN, D.G., 2008. Efficiency and fuel utilisation of methane-powered single-chamber solid oxide fuel cells. Journal of Power Sources, 183(1), pp. 157-163.

[77] MOREL, B., ROBERGE, R., SAVOIE, S., NAPPORN, T.W. and MEUNIER, M., 2009. Temperature and performance variations along single chamber solid oxide fuel cells. Journal of Power Sources, 186(1), pp. 89-95.

[78] YANO, M., NAGAO, M., OKAMOTO, K., TOMITA, A., UCHIYAMA, Y., UCHIYAMA, N. and HIBINO, T., 2008. A single-chamber SOFC stack operating in engine exhaust. Electrochemical and Solid-State Letters, 11, pp. B29.

[79] ISHIHARA, T. and TAKITA, Y., 2001. Partial oxidation of methane into syngas with oxygen permeating ceramic membrane reactors. Catalysis surveys from Japan, 4(2), pp. 125-133.

[80] BUERGLER, B.E., GRUNDY, A.N. and GAUCKLER, L.J., 2006. Thermodynamic equilibrium of single-chamber SOFC relevant methane–air mixtures. Journal of the Electrochemical Society, 153, pp. A1378.

[81] HIBINO, T. and IWAHARA, H., 1993. Simplification of solid oxide fuel cell system using partial oxidation of methane. Chemistry Letters, 22(7), pp. 1131-1134.

[82] ASANO, K., HIBINO, T. and IWAHARA, H., 1995. A novel solid oxide fuel cell system using the partial oxidation of methane. Journal of the Electrochemical Society, 142, pp. 3241.

[83] HIBINO, T., WANG, S., KAKIMOTO, S. and SANO, M., 1999. Single chamber solid oxide fuel cell constructed from an yttria-stabilized zirconia electrolyte. Electrochemical and solid-state letters, 2, pp. 317.

[84] HIBINO, T., HASHIMOTO, A., INOUE, T., TOKUNO, J., YOSHIDA, S. and SANO, M., 2000. Single-chamber solid oxide fuel cells at intermediate temperatures with various hydrocarbon-air mixtures. Journal of the Electrochemical Society, 147(8), pp. 2888-2892.

[85] HIBINO, T., HASHIMOTO, A., YANO, M., SUZUKI, M., YOSHIDA, S. and SANO, M., 2002. High performance anodes for SOFCs operating in methane-air mixture at reduced temperatures. Journal of the Electrochemical Society, 149, pp. A133.

[86] HIBINO, M., MICHIBA, D., KANATANI, K., SUZUKI, H. and YAO, T., 2006. Single Chamber Solid Oxide Fuel Cell Using BaLaln2O5. 5 Electrolyte. Advances in Science and Technology, 45, pp. 1875-1878.

[87] NAGAO, M., YANO, M., OKAMOTO, K., TOMITA, A., UCHIYAMA, Y., UCHIYAMA, N. and HIBINO, T., 2008. A Single-Chamber SOFC Stack: Energy Recovery from Engine Exhaust. Fuel Cells, 8(5), pp. 322-329.

[88] BUERGLER, B., SIEGRIST, M. and GAUCKLER, L., 2005. Single chamber solid oxide fuel cells with integrated current-collectors. Solid State Ionics, 176(19), pp. 1717-1722.

[89] NAVEED AKHTAR, STEPHEN P. DECENT, DANIEL LOGHIN and KEVIN KENDALL, 2008. Modelling of gas flow and electrochemical effects in a single chamber solid oxide fuel cell. Journal of Electrochemical Society, 13(28), pp. 107-124.

[90] AKHTAR, N., DECENT, S.P., LOGHIN, D. and KENDALL, K., 2009. Mixed-reactant, micro-tubular solid oxide fuel cells: An experimental study. Journal of Power Sources, 193(1), pp. 39-48.

[91] FLEIG, J., TULLER, H.L. and MAIER, J., 2004. Electrodes and electrolytes in micro-SOFCs: a discussion of geometrical constraints. Solid State Ionics, 174(1-4), pp. 261-270.

[92] AHN, S.J., KIM, Y.B., MOON, J., LEE, J.H. and KIM, J., 2006. Co-planar type single chamber solid oxide fuel cell with micro-patterned electrodes. Journal of electroceramics, 17(2), pp. 689-693.

[93] LIU, M., LÜ, Z., WEI, B., ZHU, R., HUANG, X., CHEN, K., AI, G. and SU, W., 2007. Anode-supported micro-SOFC stacks operated under single-chamber conditions. Journal of the Electrochemical Society, 154, pp. B588.

[94] SUZUKI, T., JASINSKI, P., PETROVSKY, V., ANDERSON, H.U. and DOGAN, F., 2005. Performance of a porous electrolyte in single-chamber SOFCs. Journal of the Electrochemical Society, 152, pp. A527.

[95] I., R., 2008. On the single chamber solid oxide fuel cells. Journal of Power Sources, 175(1), pp. 325-337.

[96] SHIN, H., PARK, J.S., KIM, S., JUNG, H.S. and HONG, K.S., 2005. Investigation of useful or deleterious residual thermal stress component to the capacitance of a multilayer ceramic capacitor. Microelectronic engineering, 77(3), pp. 270-276.

[97] BLAINE, D., BOLLINA, R., PARK, S.J. and GERMAN, R., 2005. Critical use of video-imaging to rationalize computer sintering simulation models. Computers in Industry, 56(8), pp. 867-875.

[98] CHO, H.J., PARK, Y.M. and CHOI, G.M., 2009. A Flexible Solid Oxide Fuel Cell Supported on the Thin Porous Metal. ECS Transactions, 25(2), pp. 695-699.

[99] SHIN, H., PARK, J.S., KIM, S., JUNG, H.S. and HONG, K.S., 2005. Investigation of useful or deleterious residual thermal stress component to the capacitance of a multilayer ceramic capacitor. Microelectronic engineering, 77(3), pp. 270-276.

[100] MALZBENDER, J., WAKUI, T. and STEINBRECH, R., 2006. Curvature of planar solid oxide fuel cells during sealing and cooling of stacks. Fuel Cells, 6(2), pp. 123-129.

[101] YEH, T., KUO, D. and SHIUE, R., 2008. Thermal stress simulations of SOFC membrane-electrode assembly. Advanced Materials Research, 47, pp. 1-4.

[102] RIESS, I., 2010. Catalysis of electrochemical processes and the suppression of chemical ones are needed in mixed reactant fuel cells—Can this be achieved? Solid State Ionics, 181(17), pp. 790-795.

Chapter 3

Experimental Methods

3.1 Sample Preparation

Materials Selection

The materials used for operation in an intermediate temperature range (500°C~600°C) were NiO/CGO for anode, CGO for electrolyte and Lanthanum Strontium Cobalt Ferrite (LSCF) for cathode; their specifications are listed in Table 3.1. Some research have demonstrated that the ionic conductivity of CGO is better than that of YSZ at these temperatures. The particle size of LSCF was chosen to be larger than the other materials in order to balance the final density of each material at the end of the sintering process. Each green layer was prepared with the support of Maryland Tape-casting ltd using the powders supplied by fuelcell materials ltd. The slurry compositions are shown in Table 3.2 and each slurry was tape-casted with 20 μm thickness.

Table 3.1 Specification of materials

Name	Composition	d_{50} (μm)	S_{BET} (m^{2}g^{-1})
NiO/CGO	60 wt% NiO/ 40 wt% CGO	0.3	4-8
CGO	$Ce_{0.8}Gd_{0.2}O_{2-\delta}$	0.3	5-8
LSCF	$La_{0.6}Sr_{0.4}Co_{0.2}Fe_{0.8}O_{3-\delta}$	1.0	4-8

The %TD of each green ceramic material was determined by the Archimedes method using rectangular pieces of each material and they were compared with the results of cross sectional images from SEM analysis of the material sintered at 1200°C. It was described further in Section 3.2.

To find out suitable materials with better performance and reliability, some researchers have carried out a comparative study with various cathode materials [1-4]. These have shown that LSM is not suitable for SC-SOFC due to high polarisation resistance, whilst SSC and BSCF are not stable under single chamber conditions during long time operation. In contrast, LSCF has suitable conductivity and good stability under methane-air mixtures, which makes it seem the most promising cathode material in SC-SOFCs. In addition, good ionic conductors such as Strontium/Magnesium-doped Lanthanum Gallate (LSGM) and CGO are selected as electrolyte materials, for the reduction of the operating temperature. However, LSGM may present serious issues regarding chemical reactions with electrodes and is therefore not widely used as an electrolyte. Hence, the materials NiO/CGO (anode), CGO (electrolyte) and LSCF (cathode) are deemed as suitable selections for this study. Regarding initial particle size, larger sized LSCF was used as a cathode material as it is known that the sintering temperature of LSCF is generally lower than that of NiO/CGO and CGO. To balance the final density of materials during the co-sintering process, the sintering behaviour of LSCF should be retarded.

Table 3.2 Slurry compositions for tape-casting

Anode layer		Electrolyte layer		Cathode layer	
Materials	wt%	Materials	wt%	Materials	wt%
Nickel Oxide-GDC (60 wt%NiO-40wt%GDC)	63.3	Gadolinium-Doped Ceria (20% Gd)	62.13	LSCF	62.36
Xylenes	14.22	Xylenes	14.61	Xylenes	12.74
Ethyl Alcohol (95%)	14.22	Ethyl Alcohol (95%)	14.61	Ethyl Alcohol (95%)	12.74
Polyvinyl Butyral, B-98	4.11	Polyvinyl Butyral, B-98	4.35	Polyvinyl Butyral, B-98	6.24
Triethyleneglycol bis(2-ethyl hexanoate)	1.44	Triethyleneglycol bis(2-ethyl hexanoate)	1.53	Triethyleneglycol bis(2-ethyl hexanoate)	2.18
Polyalkylene Glycol	1.44	Polyalkylene Glycol	1.53	Polyalkylene Glycol	3.12
Hypermer KD-1	1.27	Hypermer KD-1	1.24	Hypermer KD-1	0.62

Thin Layer by Tape-casting method

In conventional fabrication processes, multilayer structures have been produced by a die-pressing method with powders and the screen-printing method with material slurries [5, 6]. However, this process is not suitable for thin and curved structures that are susceptible to shrinkage and curvature evolution, resulting in cracking and delamination during co-sintering. As shown in Figure 3.1, the thickness of the single layer by die-pressing was 1 mm and cracking had occurred due to bending behaviour during sintering.
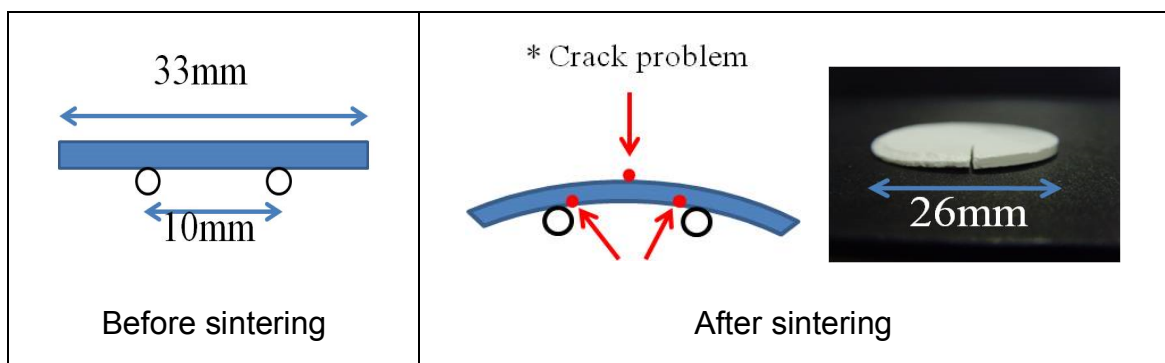

Figure 3.1 Curvature result of YSZ circular layer during sintering

The high stiffness of the materials renders them difficult to fabricate curved dimensions out of die-pressing. Since a multilayer structure should be flexible at room temperature in order for the curved shape to be maintained, the materials were prepared by the tape-casting method in Figure 3.2.
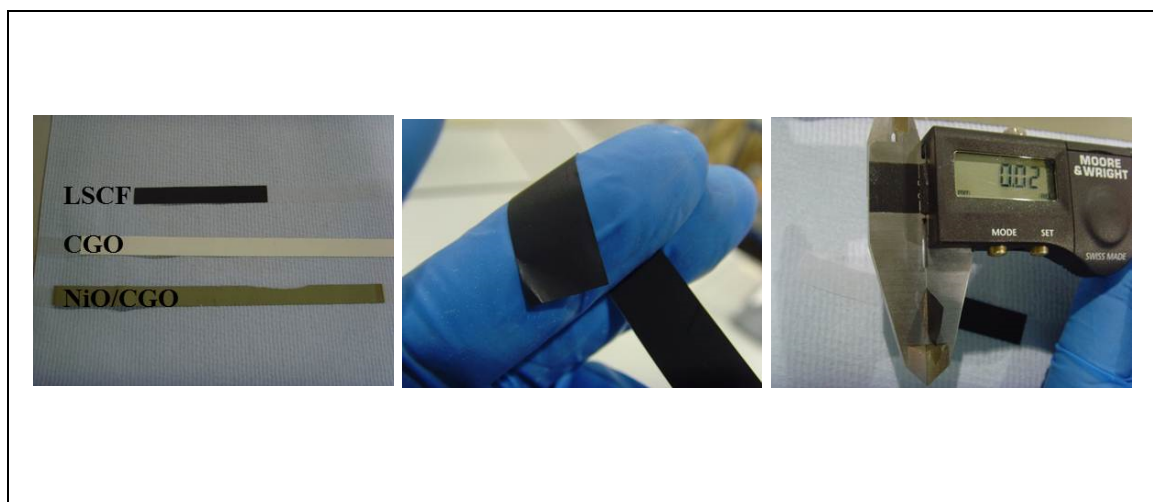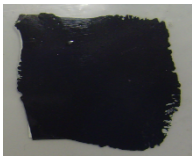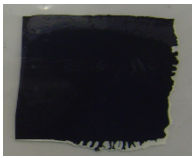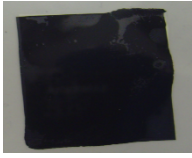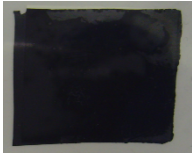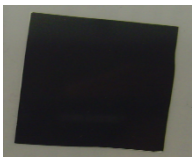

Figure 3.2 Green layers with 20 μm thickness by the tape-casting method

Lamination Procedure for the Multilayer Structure

For bi- and triple-layer structures, a hot-pressing method was used at 40ºC under 45 bar for 5 min. The multi-layer structure layout consisted of anode (NiO/CGO) | electrolyte (CGO) | cathode (LSCF) and the thickness of each material was adjusted by lamination of several sheets. For the bi-layer specimens, utilising hot pressing under various conditions resulted in some samples demonstrating symptoms of crushing, as illustrated by Table 3.3. This is believed to be due to the high temperatures and pressures involved. In addition, low pressure and temperature resulted in delamination.

Table 3.3 Bi-layer structures using hot-pressing in various conditions

	250 bar	130 bar	60 bar	45 bar	25 bar
80ºC				(crushing)	(crushing)
50ºC	(crushing)	(crushing)			(delamination)
40ºC	(crushing)	(crushing)	(crushing)		(delamination)
20ºC	(crushing)	(crushing)	(delamination)	(delamination)	(delamination)

As the slurry condition for cathode was different from others, the cathode layer during hot-pressing was more sensitive to temperature and pressure. The bi-layer structures consisted of anode-electrolyte structures and electrolyte-cathode structures, with different thicknesses and thickness ratios. Triple-layer
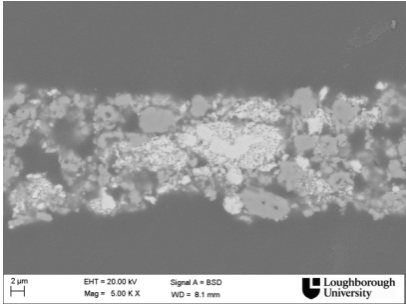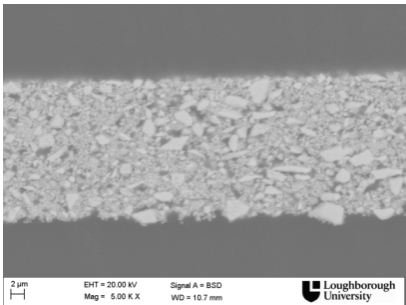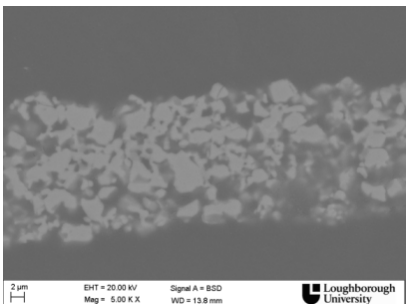
structures consisted of an anode-electrolyte-cathode composition with different thicknesses and thickness ratios.

3.2 Shrinkage Measurement by Free and Vertical Sintering

Dilatometer equipment has been widely used to measure shrinkage behaviours of samples during sintering in conventional methods for shrinkage measurement. However, as the green layers by the tape-casting method were too thin to use this equipment for shrinkage measurement, an optical method was applied to characterise the shrinkage behaviour of each material. Following the sintering process of each material, the Archimedes method was carried out to confirm the final density of the sintered samples. As the porous structures consist of one or more solid phases along with pores, pores including open and closed pores are cavities filled with air or other gas. Among open pores, there are different pores. Of particular salience are, pores which liquid may flow, and saturable pores. It was found that the water absorption was dependent on open porosity and the pore size [7]. As closed pores are not influenced by water absorption, this detail should be considered. Additionally, when immersing a porous thin structure in water, cracks might occur due to stresses from capillary action. According to these features, the type of soaking medium and other conditions must be considered. In this study, the use of the Archimedes method might provide inaccurate data due to the condition of the pores inside the structures. To compensate for the defect, SEM analysis with these samples was carried out. The cross-sectional images of the samples were analysed by SEM and the area of pores was measured by ImageJ program. Three different locations were selected in each material for SEM analysis and the results from the area of pores in cross-sectional image helped to confirm the density measured by Archimedes method. Thereby, the %TD of a green body was calculated by shrinkage data and the density sintered at 1200ºC. The data that was obtained will be discussed further in Chapter 4. Based on these measurements, %TD of each green material was calculated at 53.7% for anode, 51.8% for electrolyte, and 53.8% for cathode, as shown in Table 3.4.

Table 3.4 %TD of green materials

Material	SEM image at 1200ºC	%TD of a green compact	
		SEM analysis	Archimedes method
NiO/CGO		56.5	53.7
CGO		57.2	51.8
LSCF		54.4	53.8

Free Sintering

Each layer of materials was prepared by cutting into rectangular specimens at roughly 4 mm (W) by 3 mm (L). These samples were located in the sample holder as a freestanding structure and leaned on a vertical wall of the specimen support. The sintering experiment was carried out by heating up to 750ºC with a heating rate of 1ºC min^{-1}. This was done slowly to prevent the

standing sample from curving due to binder softening. After finishing binder burnout at 750ºC, a heating rate of 3ºC min⁻¹ was applied up to the sintering temperature. To obtain a porous structure after the sintering process, the final temperature was set at 1200ºC. During the debinding process, shrinkage occurred, but it was not considered in this study. From 900ºC and above, the shrinkage in the width direction of the sample was monitored by a long-focus camera (Infinity K-2), as shown in Figure 3.3. In accordance with the assumption of isotropic shrinkage during the sintering process, the densification profile can be obtained from linear shrinkage data measured in the width direction as follows.

$$\rho_0 V_0 = \rho_t V_t \tag{3.1}$$

where ρ_0 is the %TD of a green sample; V_0 is the initial volume; and ρ_t and V_t are the %TD and volume at a specific time. As the shrinkage behaviour of the sample occurs isotropically along each direction, the volume can be replaced by the width of the sample such that

$$\rho_t = \rho_0 \left(\frac{w_0}{w_t}\right)^3 \tag{3.2}$$

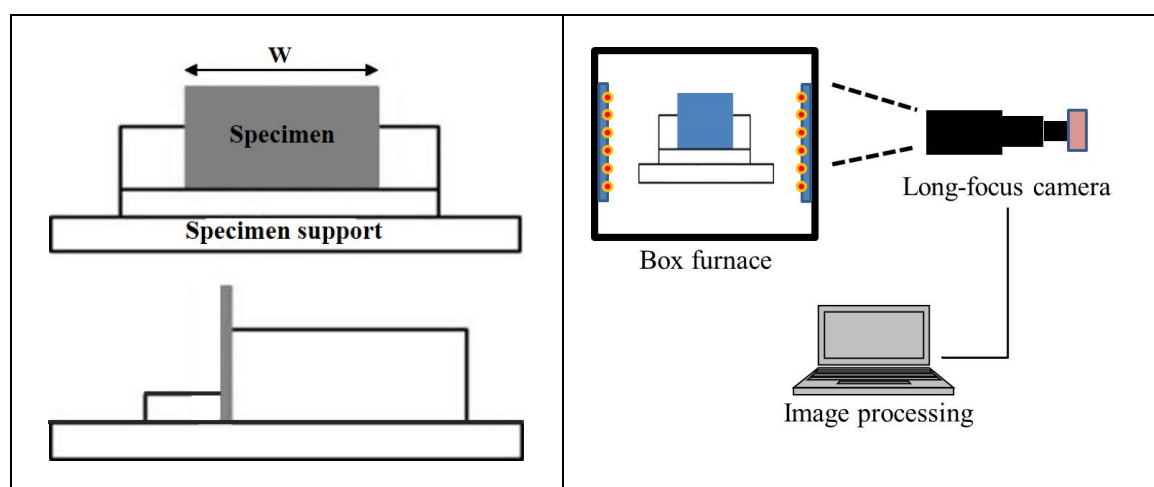The densification graph is plotted by obtaining the shrinkage change of the sample during sintering.

Figure 3.3 Schematic of sample preparation in free sintering

Vertical Sintering

T-shape samples were prepared by cutting roughly 3 mm (W) by 7 mm (L), as shown in Figure 3.4. These samples were hanging on the specimen support and shrinkage measurement was monitored along the vertical direction by the optical method. The heating condition was the same as in the free sintering process. In a vertical sintering, shrinkage behaviour was affected by the gravity effect. The applied stress in the vertical sintering was only subjected to its own weight. As this stress was very low, it did not affect the microstructure during sintering [8]. The densification process can be considered to be linearly viscous. In vertical sintering the self-weight is constant during the sintering process. However, this method cannot be used for measuring viscosity during the final stages of densification because the strain rates for vertical and free sintering are very similar.
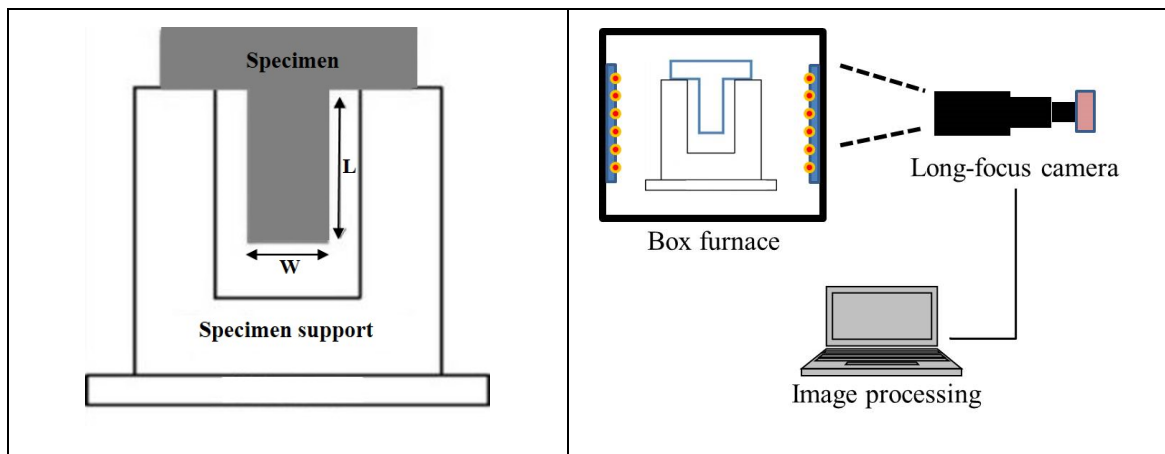
Figure 3.4 Schematic of shrinkage measurement in vertical sintering

Equation 3.3 was proposed by Cologna et al. [8] for the measurement of uniaxial viscosity; ρ density, g gravity, L sample length, $\dot{\varepsilon}_v$ strain rate in vertical sintering, $\dot{\varepsilon}_f$ strain rate in free sintering. It shows that at similar strain rates the viscosity becomes very large. Prior to the final stages there are measurable differences in the two strain rates and a viscosity can be calculated. The difference in strain rates between free sintering and vertical sintering is the key influencing factor in the determination of the uniaxial viscosity of the structure during co-sintering.

$$\eta = \frac{\rho g L}{2 \left(\dot{\varepsilon}_v - \dot{\varepsilon}_f \right)} \qquad (3.3)$$

3.3 In-situ Observation of Curvature Evolution

Curvature measurements were made using the specimens with 3 mm (W) x 1 mm (L). These samples were cut from the bi- and triple-layer structures assembled by the hot-pressing method and laid on alumina tube supports. During co-sintering, in-situ experimental observation of curvature evolution as a function of temperature was performed with the bi- and triple-layer structures. Bi-layer structures, consisting of NiO/CGO-CGO and CGO-LSCF, have the same thickness ratio with 1:3. The co-sintering profile was the same condition in free and vertical sintering. During co-sintering, the image of curvature evolution of the samples was captured at every 25ºC and the radius of the curvature using Equation (2.14). Although undesired curvature evolutions of the specimens occurred during the debinding process, this study analysed the curvature evolution that occurred from 900°C only.

3.4 Fabrication of a Wavy type SC-SOFC

The fabrication method of wavy type SC-SOFC was investigated through the co-sintering of bi- and triple-layer structures. The triple-layer structure, consisting of one layer of anode, three layers of electrolyte and nine layers of cathode, was prepared with 35 mm (W) x 35 mm (L) and laid on alumina rods. These rods helped the triple-layer structure to form a wavy shape during the co-sintering process. At 80°C, wavy-shaped triple-layer structures could be formed due to binder softening.

After completing the co-sintering of the triple-layer structure, the current collector was coated on anode and cathode using silver (silver conductive paste, Sigma-Aldrich) and cured at 150°C for 20 min. A vertical cylinder was used as a single chamber in Figure 3.5 and fabricated cells were located inside the cylinder.
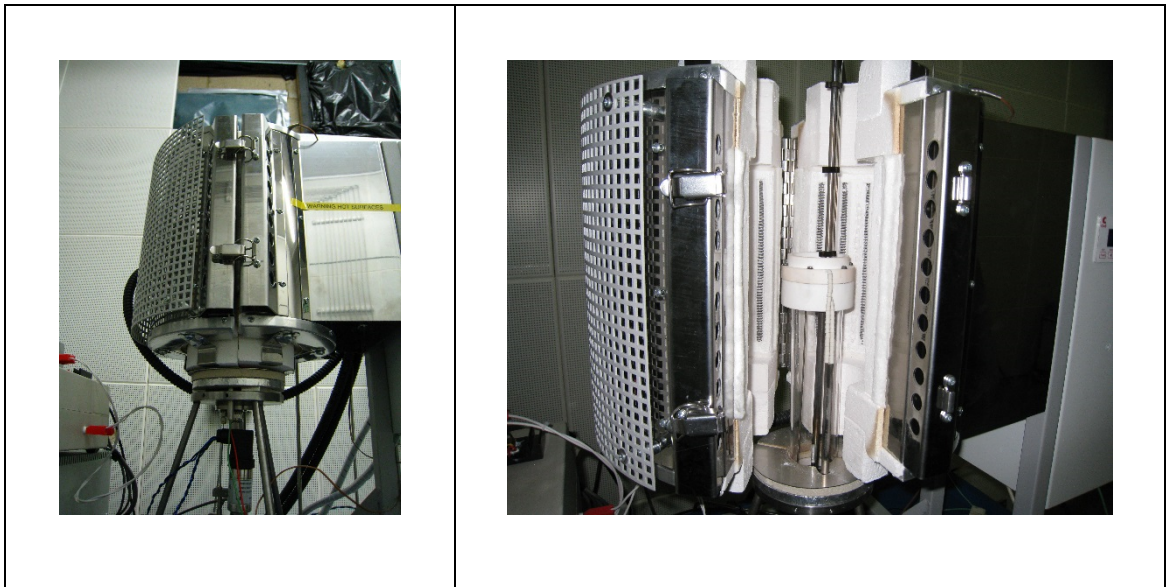
Figure 3.5 Test rig of SC-SOFCs

As shown in Figure 3.6, a methane-air mixture was passed through all the layers, allowing for electrochemical reactions to take place. As gas mixtures of methane and air at high temperature are used for SC-SOFCs, it should be of prime concern to find stable conditions for mixtures with respect to the explosion and flammability limits. It has been known that the concentration of a combustible gas in air plays significant role and methane concentrations in air between 5 and 15 vol% gives opportunity for flammability and/or spontaneous combustion/explosion [9].
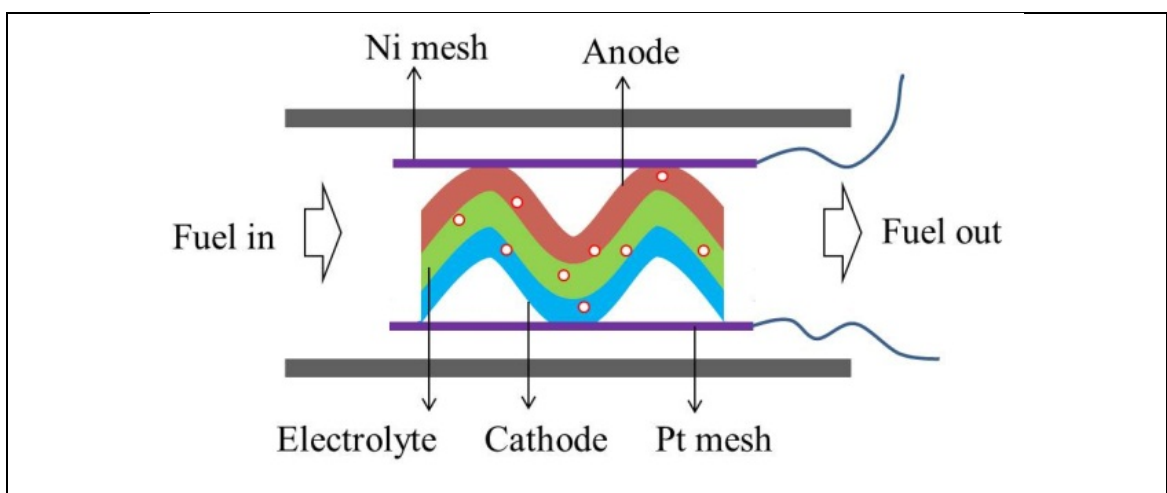
Figure 3.6 Schematic of performance test

To avoid flammability, the gas mixture was composed with a ratio of methane to oxygen (CH_4:O_2=1:1). The total gas flow rate was 0.6 Lmin^{-1}. The operating temperature was 600°C and the reduction process of the NiO was carried out at 800°C for 1h with a hydrogen-nitrogen mixture (5 vol% H_2 / 95 vol% N_2). The performance of SC-SOFCs is very sensitive to operation conditions such as mixture ratio, temperature, and materials. As this study focuses on differences of performance from different shapes between planar cells and wavy cells, all operation conditions are fixed with 600°C, 0.6 Lmin^{-1}, and CH_4:O_2=1:1.

References

[1] MORALES, M., PIÑOL, S. and SEGARRA, M., 2009. Intermediate temperature single-chamber methane fed SOFC based on Gd doped ceria electrolyte and La0.5Sr0.5CoO3−δ as cathode. Journal of Power Sources, 194(2), pp. 961-966.

[2] MORALES, M., ROA, J.J., TARTAJ, J. and SEGARRA, M., 2012. Performance and short-term stability of single-chamber solid oxide fuel cells based on La0.9Sr0.1Ga0.8Mg0.2O3−δ electrolyte. Journal of Power Sources, 216(0), pp. 417-424.

[3] SUN, C., HUI, R. and ROLLER, J., 2009. Cathode materials for solid oxide fuel cells: a review. J Solid State Electrochem, 14(7), pp. 1125-1144.

[4] SUN, L., RIEU, M., VIRICELLE, J., PIJOLAT, C. and ZHAO, H., 2014. Fabrication and characterization of anode-supported single chamber solid oxide fuel cell based on La 0.6 Sr 0.4 Co 0.2 Fe 0.8 O 3− δ–Ce 0.9 Gd 0.1 O 1.95 composite cathode. International Journal of Hydrogen Energy, 39(2), pp. 1014-1022.

[5] LENG, Y., CHAN, S., KHOR, K. and JIANG, S., 2004. Development of LSM/YSZ composite cathode for anode-supported solid oxide fuel cells. Journal of Applied Electrochemistry, 34(4), pp. 409-415.

[6] HOLTAPPELS, P., VOGT, U. and GRAULE, T., 2005. Ceramic materials for advanced solid oxide fuel cells. Advanced Engineering Materials, 7(5), pp. 292-302.

[7] KATO, T., OHASHI, K., FUJI, M. and TAKAHASHI, M., 2008. Water absorption and retention of porous ceramics fabricated by waste resources. Journal of the Ceramic Society of Japan, 116(1350), pp. 212-215.

[8] COLOGNA, M. and SGLAVO, V.M., 2010. Vertical sintering to measure the uniaxial viscosity of thin ceramic layers. Acta Materialia, 58(17), pp. 5558-5564.

[9] ZABETAKIS, M.G., 1965. Flammability characteristics of combustible gases and vapors, Bulletin 627, U.S. Department of the Interior, Bureau of Mines.

Chapter 4

Free Sintering and Vertical Sintering

4.1 Results

The shrinkage profiles of NiO/CGO, CGO and LSCF during free and vertical sintering are shown in Figure 4.1. It can be clearly seen that there is a significant difference in the shrinkage behaviour for each material between free and vertical sintering. The shrinkage change during the debinding process was subtracted and the dimensional condition of the sample at 900ºC was set as a datum reference for shrinkage measurement during sintering. In the early stage of sintering, shrinkage behaviour for the free and vertical samples was similar up to 1000ºC. After this temperature the free sintering sample shrank faster than the vertical sintering sample. During vertical sintering samples are subject to a low level of stress derived from their weight. The tensile stresses that arise from the loading cause a reduction in the amount of shrinkage that occurs during this type of sintering when compared to free sintering [1-3]. The shrinkage difference at the final temperature between free and vertical sintering was measured as: 0.11 for NiO/CGO; 0.018 for CGO; and 0.008 for LSCF. Comparing the shrinkage behaviour of each material between the NiO/CGO and CGO, it is seen that the shrinkage of NiO/CGO at 1200°C is greater than CGO. This results from a higher %TD of NiO/CGO. The LSCF sample contains particles with a dimension of 1 µm and the shrinkage pattern was different in comparison with LSCF with sub-micron-sized particles, which could achieve a fully sintered condition at 1200°C. This helps to balance final density of each material during co-sintering, so as to enable fabrication of a multi-layer structure with similar porosity throughout.
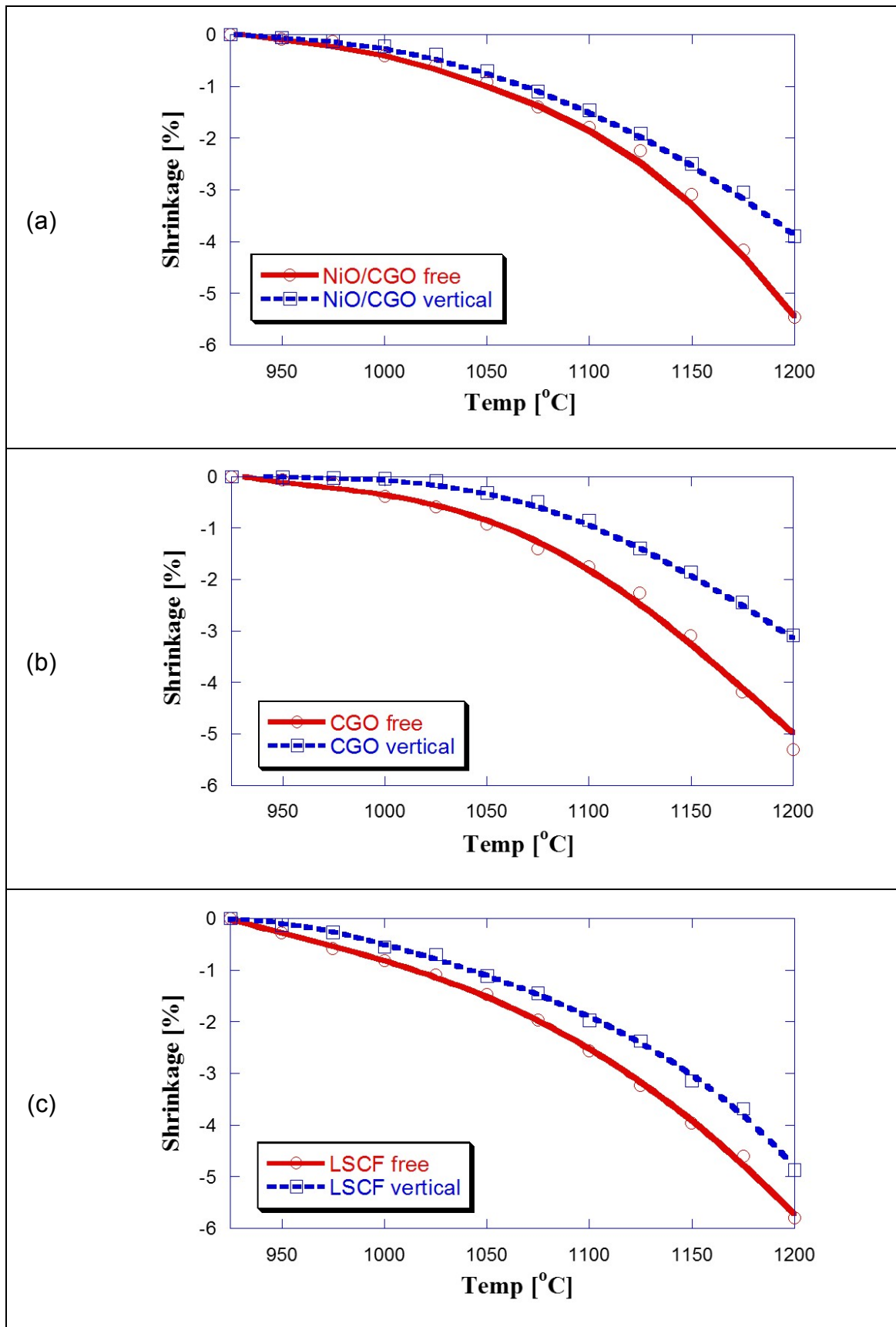
Figure 4.1 Comparison of Shrinkage in free and vertical sintering; (a) NiO/CGO, (b) CGO, and (c) LSCF

With respect to shrinkage of CGO material, Figure 4.2 shows the shrinkage differences with NiO/CGO and LSCF during the sintering process. In shrinkage, there was little difference in the NiO/CGO-CGO specimen due to the great similarity of material properties, but significant difference has occurred in the CGO-LSCF specimen. It was expected that higher shrinkage of LSCF would lead the curvature evolution of bi- and triple-layer structures at the early stage of co-sintering.

The densification profiles calculated from shrinkage of free sintering are shown as a function of temperature in Figure 4.3. The final density of sintered samples was measured using the Archimedes method and the results were confirmed through comparison with cross sectional images of the sintered samples using SEM [4, 5]. After finishing the sintering process, the %TD of samples were measured as: 63.9% for NiO/CGO; 61.1% for CGO; and 64.2% for LSCF (again using the Archimedes method). The densification graphs show that onset point of densification process for the LSCF sample was earlier than the other samples by approximately 50°C. However, since the initial particle size of LSCF was larger than others, the sintering process was entirely retarded and the final density of LSCF was similar to other materials after finishing the sintering process [6-8].
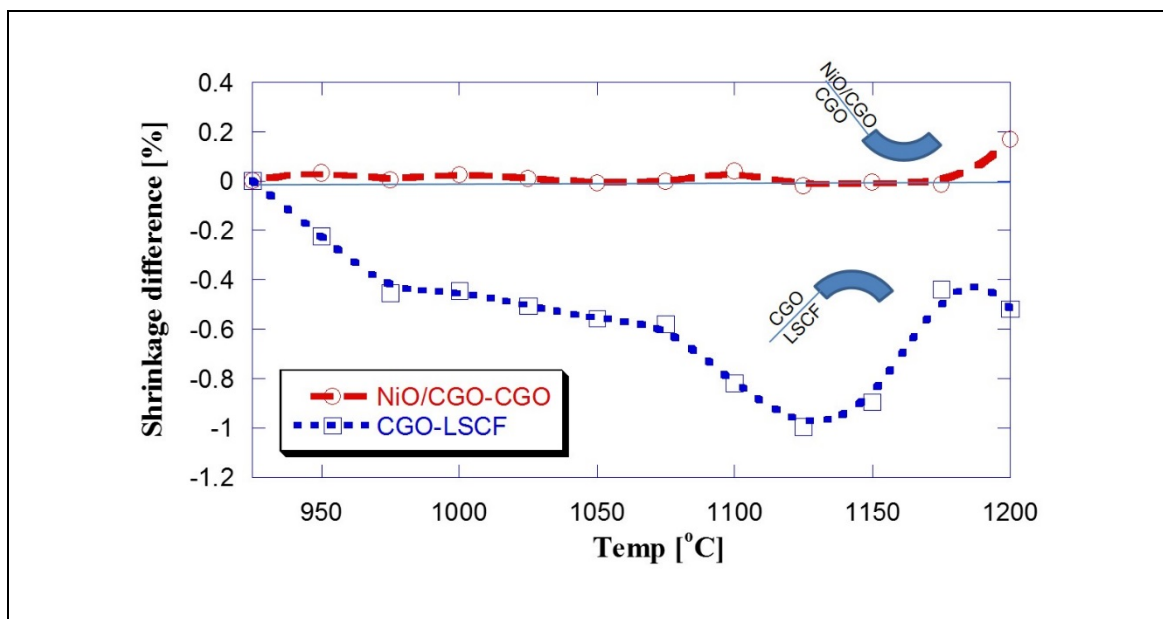
Figure 4.2 Shrinkage differences of NiO/CGO-CGO and CGO-LSCF
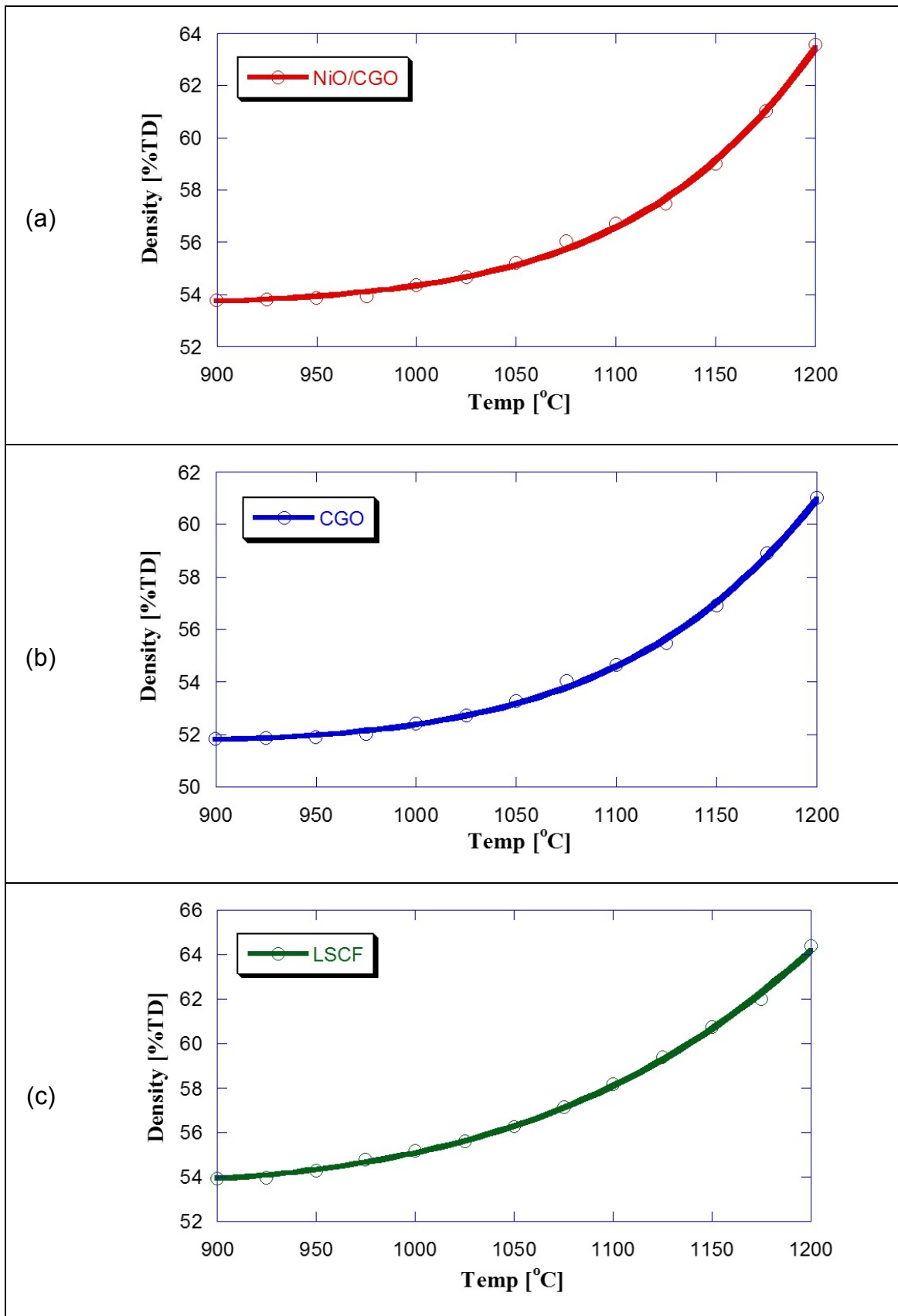
Figure 4.3 Densification of each material during sintering; (a) NiO/CGO, (b) CGO, and (c) LSCF

Figure 4.4 shows cross sectional SEM images of each material that was sintered at 1200°C. From the SEM analysis, the porosity of each specimen was measured. The measured porosity values were 33.2% for NiO/CGO; 36.9% for CGO; and 34.8% for LSCF using the porous area mapping by imageJ program. This is consistent with the final densities measured by Archimedes method, as shown in Table 4.1. The microstructure of the NiO/CGO and LSCF shows larger pores and particle sizes as compared to that of CGO. In addition, the sintered samples at 1200°C show overall interconnectivity of the particles and partially coarser microstructures. In Figure 4.4 (a), the NiO and CGO were well-distributed in the anode layer, contributing to interconnection with the electrolyte layer during the co-sintering of multi-layer structure. During sintering, third phase formation might occur, which influences ionic conductivity and thermo-mechanical properties during cell operation. To confirm phase changes during sintering, XRD analysis of sintered materials was carried out; the results are discussed in Chapter 6.

Table 4.1 Comparison of %TD of sintered samples

	Archimedes method (%TD)	SEM analysis (%TD)
NiO/CGO	63.9	66.8
CGO	61.1	63.1
LSCF	64.2	65.2

Figure 4.4 Cross sectional images of sintered samples using SEM; (a) NiO/CGO, (b) CGO, and (c) LSCF

The shrinkage rates of each material in free and vertical sintering are shown in Figure 4.5. These graphs were derived from the data presented in the shrinkage graphs shown Figure 4.1. The shrinkage rates for samples NiO/CGO and CGO show a differ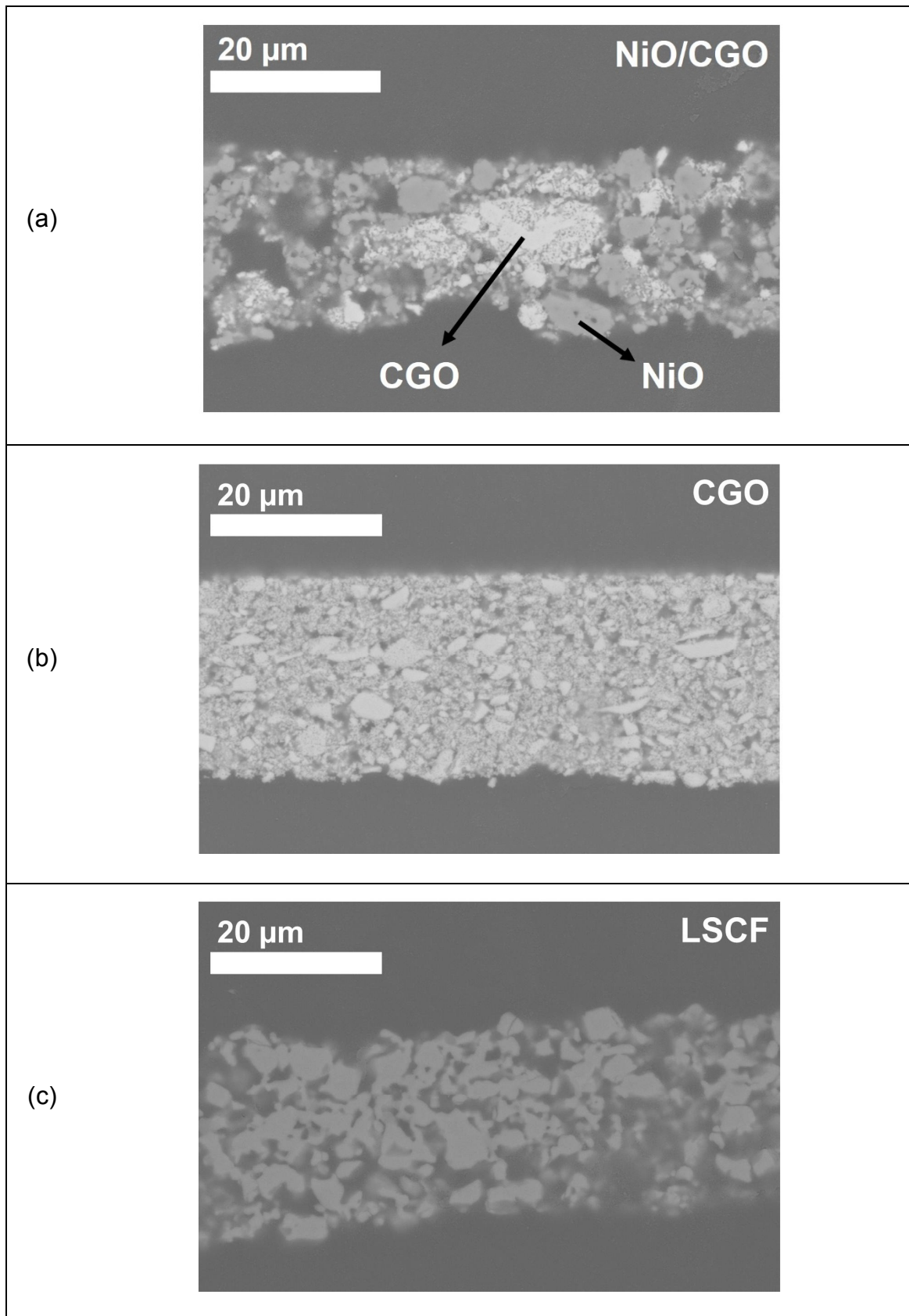ent behaviour for free sintering compared to vertical sintering as shown in Figure 4.5 (a) and (b), whereas the LSCF sample shows a similar behaviour for the two sintering methods. In the case of NiO/CGO, the difference of shrinkage rate increased until 1200°C, resulting from the fact that NiO particles prevented CGO particles from fusing together during sintering. It means that the existence of NiO particle leads to retarded shrinkage behaviour of vertical sintering and that the shrinkage behaviour had been influenced by the applied stress (due to self-weight) up to the final temperature [9, 10]. For the CGO sample as the temperature neared 1200°C the difference in shrinkage rates reduced slightly. Possible reasons could include the uniformity of particle size and the evolution of the grain structure. As CGO had higher sinterability than NiO/CGO at the same temperature, the influence of self-weight was decreased in the vertical sintering, resulting in reduction of the difference at 1200°C.

In the shrinkage rate of LSCF, a small difference is observed up to 1075°C and then decreases up to the final temperature. Small tearing of hanging tapes during vertical sintering had occurred, due to different ratio of additives in LSCF slurry, compared to those of anode and electrolyte tapes. To sort out this problem, the sample was reduced to a third of the initial length, but the aspect ratio was maintained with respect to anode and electrolyte tapes. Overall, there was not a significant difference of shrinkage rate between free sintering and vertical sintering. This is attributed to higher sinterability of LSCF, compared to CGO at the same temperature [11, 12]. At final temperature, it showed that shrinkage rate in free and vertical sintering was almost similar. This can be explained with reference to the sample's own weight no longer acting as an applied stress in vertical sintering from 1200°C. In other words, as the stress derived from its self-weight in the vertical sintering is too small to influence shrinkage retardation, the difference of shrinkage rate is close to zero when the %TD of the sample is increased over 70% with higher viscosity.
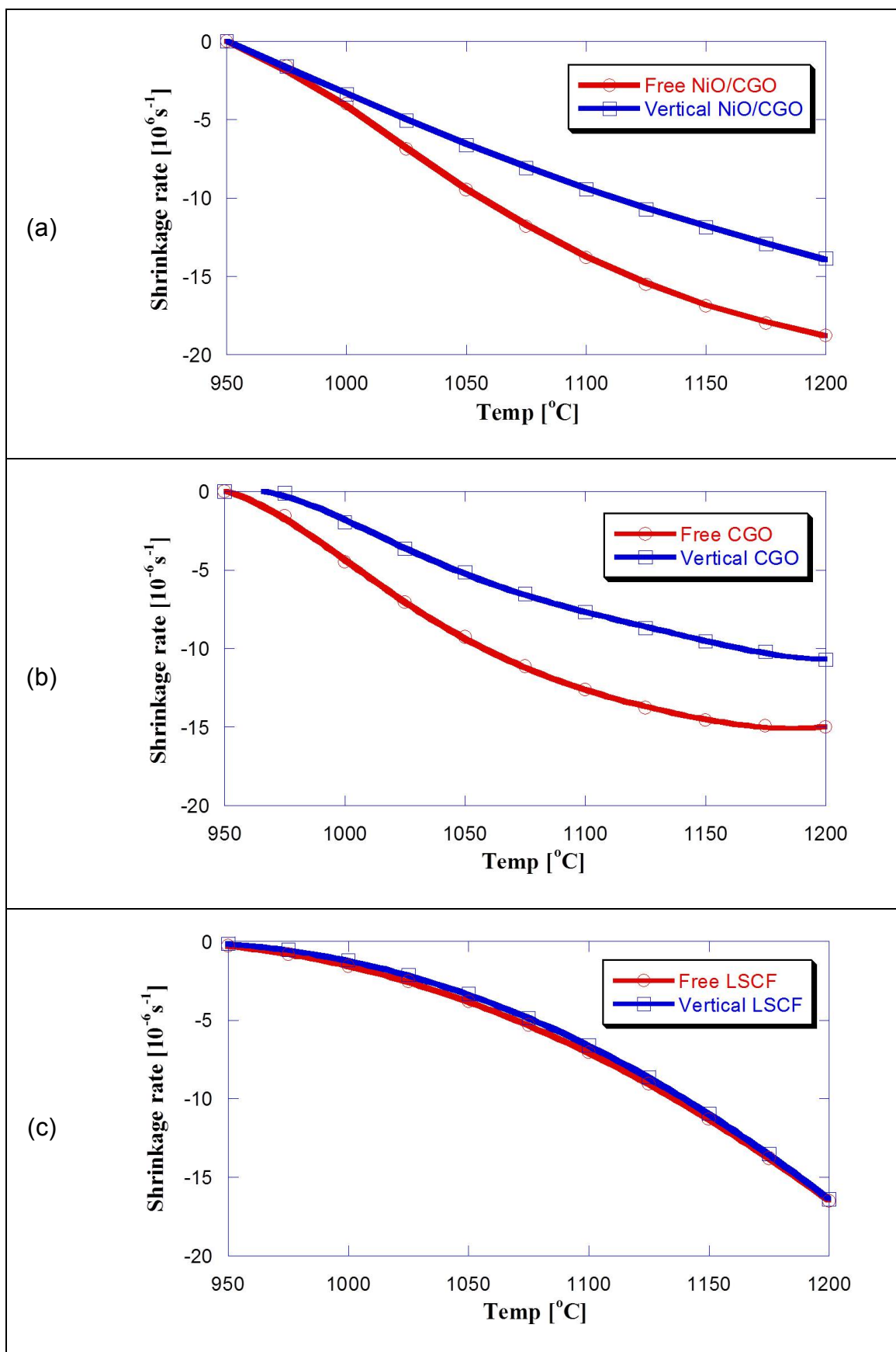
Figure 4.5 Shrinkage rates of samples; (a) NiO/CGO, (b) CGO, and (c) LSCF

In the elastic-viscous analogy, the parameters such as Young's modulus, Poisson's ratio and shrinkage can be replaced with the uniaxial viscosity, the viscous Poisson's ratio and shrinkage rate respectively. Using Equation 3.3 proposed by Cologna [13], the uniaxial viscosity of the material can be measured. During the vertical sintering process, the self-weight acts only as an applied stress contributing to the shrinkage behaviour. As it is noted that the applied stress results in a very low tensile stress and does not affect the microstructure during sintering, this densification process can be considered as linearly viscous. Though this stress is constant and continuously applied to the sample through the whole sintering process, the method is unable to accurately measure the uniaxial viscosity at high density, which results from similarity of shrinkage rate between free and vertical sintering. The difference of shrinkage rate between free and vertical sintering is the main influential factor that determines the uniaxial viscosity of the structure.

As shown in Figure 4.6, the uniaxial viscosity of each material as a function of %TD was calculated from shrinkage rate difference between free and vertical sintering. In the early stages of sintering, the viscosity is relatively high and then decreases with increasing temperature. In the latter stages of sintering the viscosity increases with increasing density in the high temperature range. In this method, the viscosity corresponds to the applied stress over the difference of shrinkage rate between free and vertical sintering. But the very low applied stress does not affect significant differences in the shrinkage rate at very high viscosities (in low temperature or high density). Therefore, initial viscosity values in the early stage of sintering can be regarded as an error. The uniaxial viscosity of NiO/CGO and CGO shows similar trend depending on density. In case of LSCF, the viscosity was low at the early stage of sintering, but its rate was high with increasing density due to more active sintering behaviour compared to NiO/CGO and CGO.

For co-sintering bi-layer structures, Cai's equation was used for measurement of stresses and curvature evolution with factors such as thickness ratio, viscosity ratio and the difference of strain rate. These were calculated by Cologna's equation and in-situ monitoring of shrinkage behaviours. However, these parameters are not fixed during co-sintering. In order to ascertain which of the prior factors is dominant in determining stresses

and curvature, each of the factors is given a weighting on a scale of 0.8 to 1.2. The results are discussed along with curvature evolution of bi-layer structures in Chapter 6.
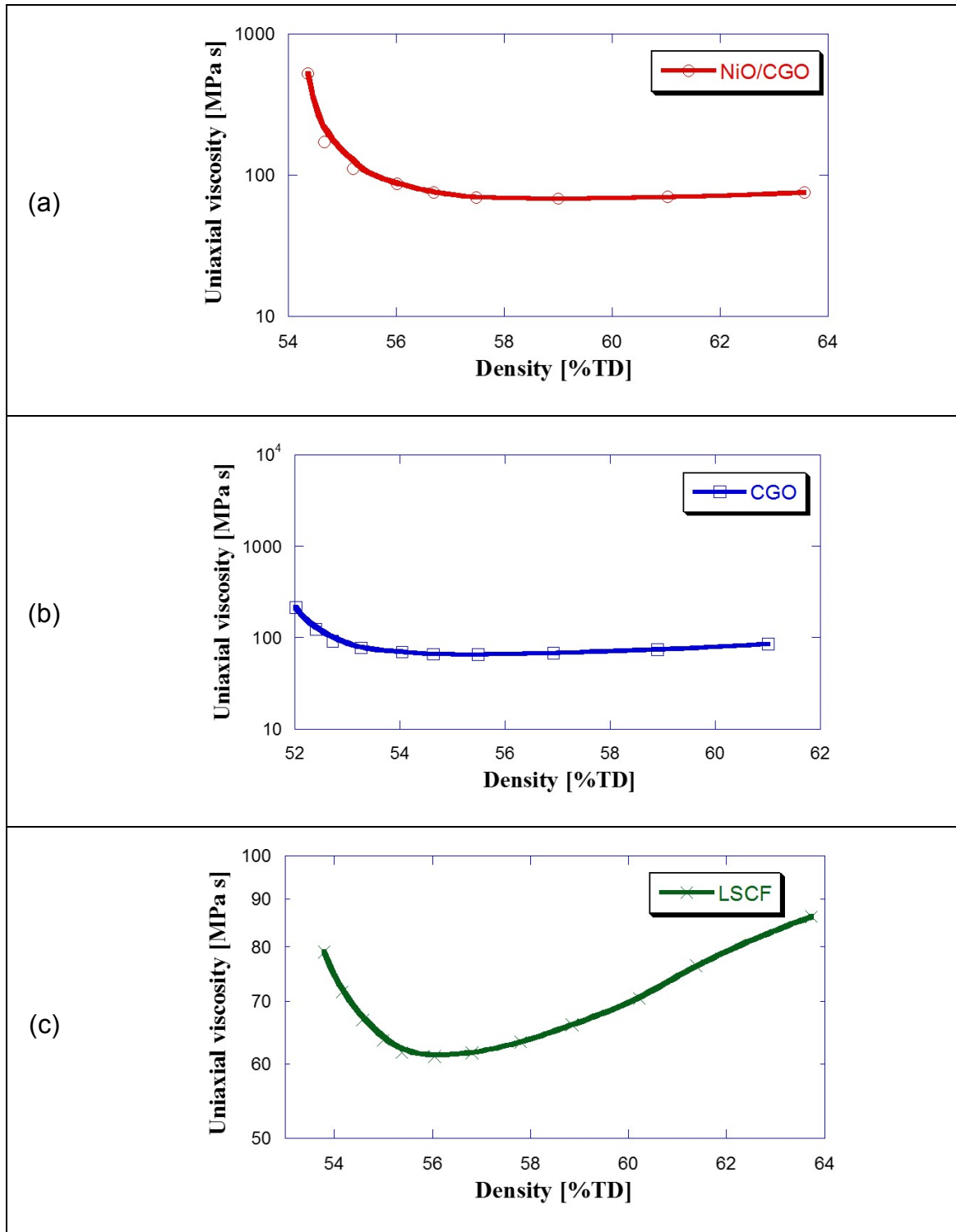

Figure 4.6 Uniaxial viscosity of each material; (a) NiO/CGO, (b) CGO, and (c) LSCF

4.2 Discussion

Shrinkage behaviour measured by non-contact method

In conventional research, shrinkage behaviour of materials during sintering has been measured by using a uniaxial pushrod dilatometer as shown in Figure 4.7 [14, 15]. Assuming uniform densification, zero creep and no mass loss, the %TD can be calculated using the Equation 4.1.

$$\% \text{ theoretical density} = \frac{\rho_i * 100}{\rho_{th}(T) * \left(1 + \frac{l_s(T)}{100}\right)} \qquad (4.1)$$

Where: ρ_i is the initial density; $\rho_{th}(T)$ is the theoretical density as a function of temperature; and $l_s(T)$ is the percent linear change of the sample in the axial direction of the pushrod as a function of temperature. Small displacement of the thin layer during sintering results in an increased level of difficulty in the use of a pushrod dilatometer for shrinkage measurement.

The shrinkage behaviour of CGO was investigated by pushrod dilatometer (NETZSCH dilatometer 402E), prior to the non-contact method. Figure 4.8 shows the result of CGO for uniaxial shrinkage measurement during sintering. Figure 4.8 (a) shows the measurements without a CGO layer and the Figure 4.8 (b) shows the measurements with a CGO layer. As the thin layer of CGO had a 20 µm thickness. As the space for samples was too big to fix the thin layer in sample holder, additional alumina spacers were applied for fitting the layer in sample holder. A control test without a CGO sample was performed four times up to 1440°C with heating rate of 10°C/min, as shown in Figure 4.8 (a) to eliminate thermal behaviour of the alumina spacers in the test with CGO layer. Figure 4.8 (b) shows shrinkage behaviour of CGO layer with spacers during sintering. Dash line is temperature profile with linear strain and black line is strain variation of the sample during heat treatment. Graph (a) showed thermal behaviour of alumina spacer and it was used as a base line to determine sintering behaviour of CGO layer from graph (b). In the comparison between (a) and (b), it is seen that there is not a significant variation between

the layer present and the layer not present. Although the shrinkage behaviour of the CGO layer with spacers was detected less than 1 value of strain during the process, it was difficult to figure out the shrinkage behaviour and it did not seem to be as valid. Hence it is not possible to establish the shrinkage property of the thin layer. It was attributed that this was beyond the capability of the equipment with a sample of this thickness. A well-known limit of the conventional pushrod dilatometers is that they work in contact with the sample to analyse. Thereby, the pressure derived from the mechanical system influences the deformation of the materials, following that the shrinkage analysis is affected and the thin sample is damaged, when the materials soften during sintering. This is the reason why non-contact measurement using a long-focus camera was established in order to investigate the shrinkage behaviour of the samples during sintering.
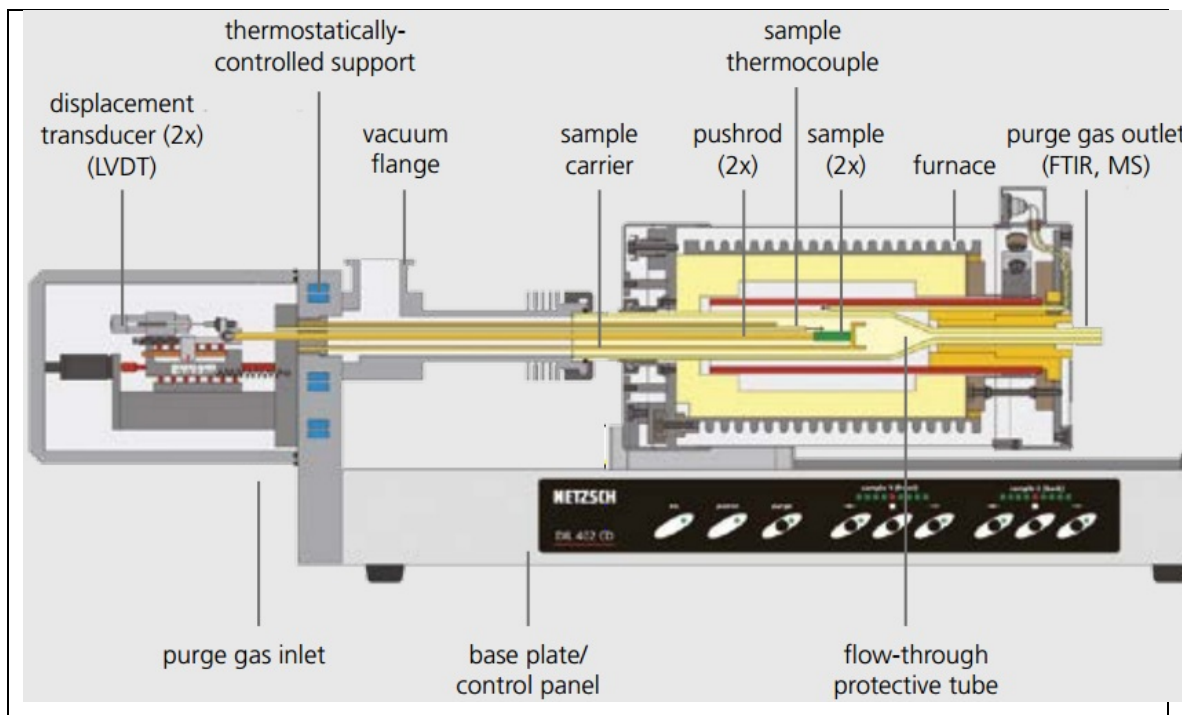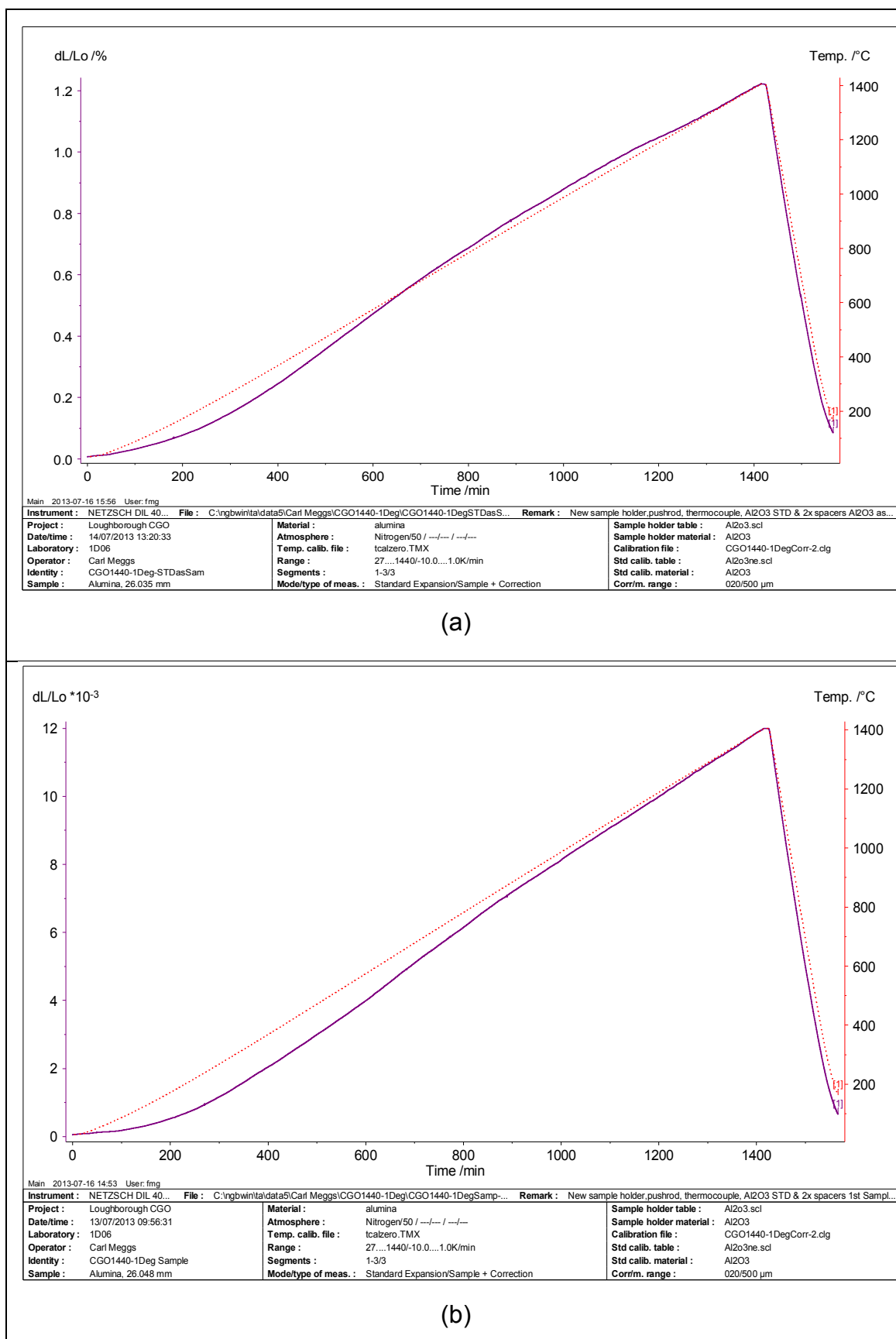

Figure 4.7 Pushrod dilatometer

(a)

(b)

Figure 4.8 Shrinkage behaviour of CGO measured by Pushrod dilatometer; (a) without CGO layer and (b) with CGO layer

Cross sectional images using SEM

The electrolyte layer consisting of smaller particles shows a narrow particle size distribution and well-dispersed porous structures. NiO particles in the anode layer prevent CGO particles from fusing together during sintering, resulting in larger pore size distribution as shown in Figure 4.4. This then would impact the connectivity of the particle network causing it to be disconnected and isolated, contributing to a reduction of TPBs in a cell. In addition, this may also impact the gas mixture flowing through large pores with low probability of electrochemical reaction [16-18]. The rough surface of the anode layer is shown compared with the electrolyte and cathode. This may influence cracking and delamination within the electrolyte layer during the co-sintering of the triple-layer structure. Compared to the image of NiO/CGO, the cross sectional image of LSCF shows larger particles with well-distributed pores. As gas mixture can flow through the whole layers, the catalytic selectivity and gas composition near TPBs will be very important factors in determining the conversions for electrochemical reaction.

Shrinkage Rate

On the basis of shrinkage rate results, the anode and electrolyte materials reach to their maximum shrinkage rate at 1200°C, while the cathode material showed a rapid declining shrinkage rate at its final stage of sintering. As mentioned earlier, the LSCF with larger particles was used to reduce final density at 1200°C, resulting in similar porous condition in sintered materials. Due to coarse particle size of LSCF, initial shrinkage rate was retarded compared to other materials [19, 20]. As the sintering temperature of LSCF is lower than other materials, a rapid decreasing pattern is shown along increasing temperature. In addition, the gap of shrinkage rate in free and vertical experiment shows different behaviours among materials. The pattern of shrinkage rate in the anode and electrolyte is similar, but shrinkage process of the anode seems to be more active than the electrolyte at 1200°C. It was attributed to the fact that NiO particles in the anode affected the sintering process to be shifted to higher temperature, resulting in shrinkage retardation.

On the other hand, there is not a significant difference between free and vertical experiment in the shrinkage rate of cathode layer. The largest difference in LSCF was measured between 1050°C and 1100°C. After that, the shrinkage rate of LSCF seems to be almost same during the final stage. It means that the applied stress from its weight did not affect shrinkage behaviour of the specimen during the vertical sintering at a high temperature. It seemed that there still remained strong compressive stress of LSCF at lower temperature against the gravity in the vertical sintering, compared with other materials.

Characterisation of Uniaxial Viscosity

Various approaches have been developed for determination of necessary viscosity parameters through sinter forging, cyclic loading method and bar-bending test under the application of external load [21-23]. In order to overcome the restrictions of these methods including limited time to avoid undesired anisotropy in the microstructure of the sample, uniaxial viscosities of the materials were experimentally characterised by in-situ observation of shrinkage measurement using optical microscope [24]. In the vertical sintering experiment for measurement of the uniaxial viscosity of thin ceramic layers, it is demonstrated that the stress magnitude of tensile load derived from its own weight with a few tens of millimetres in length during the vertical sintering is the order of 0.1 kPa in Cologna's experiment. Therefore, it can be regarded that the self-weight does not affect any microstructural change during sintering.

The difference of shrinkage rate in free and vertical sintering plays a significant role to determine uniaxial viscosity of the material. However, as shown in Figure 4.5 (c), the difference was close to zero at later stage of the sintering process, resulting in very high viscosity as an error. In this study, as final densities were measured less than 70%, this method could be considered to determine the uniaxial viscosity of the materials.

In comparison of uniaxial viscosities, the graphs of NiO/CGO and CGO showed slightly increased trend during sintering, while the rate of LSCF was rapidly changed as a function of density. It was attributed to higher sinterability of LSCF over others at a lower temperature region.

4.3 Summary

For fabrication of wavy type SC-SOFC operating in intermediate temperature, the materials chosen were NiO/CGO for anode, CGO for electrolyte, and LSCF for cathode. To analyse properties of these materials, in-situ monitoring experiments had been carried out using optical microscope. The shrinkage behaviour of the materials was investigated via shrinkage measurement along horizontal and vertical direction of the sample up to 1200°C during sintering. As the cathode material has a lower sintering temperature than others, the material with larger particles was selected to retard densification during sintering, so as to balance final density of each material. After finishing the sintering process, the final densities were measured using Archimedes method. The results were confirmed from image analysis using SEM. The porosities calculated from cross sectional images were good agreement with the densities measured experimentally. The sintered samples obtained 61%TD ~ 64%TD, and their microstructural conditions were analysed. Based on shrinkage behaviour data that associated to the temperature profile, the graphs of shrinkage rate could be drawn and the differences of the rate between free and vertical sintering were utilised for calculation of the uniaxial viscosity. The pattern of shrinkage rate in the anode and electrolyte material seemed to be alike, while the shrinkage rate of cathode material for free and vertical sintering were noticeably different. It could be considered that higher sinterability of cathode material leads to faster shrinkage behaviour during sintering compared to others, although particles of the cathode material were larger than that of other materials.

References

[1] GREEN, D.J., GUILLON, O. and RÖDEL, J., 2008. Constrained sintering: A delicate balance of scales. Journal of the European Ceramic Society, 28(7), pp. 1451-1466.

[2] KIM, J., RUDKIN, R.A., WANG, X. and ATKINSON, A., 2011. Constrained sintering kinetics of 3YSZ films. Journal of the European Ceramic Society, 31(13), pp. 2231-2239.

[3] ATKINSON, A., KIM, J., RUDKIN, R., TAUB, S. and WANG, X., 2011. Stress induced by constrained sintering of 3YSZ films measured by substrate creep. Journal of the American Ceramic Society, 94(3), pp. 717-724.

[4] WU, W., ZHANG, G., KAN, Y., WANG, P., VANMEENSEL, K., VLEUGELS, J. and VAN DER BIEST, O., 2007. Synthesis and microstructural features of ZrB–SiC-based composites by reactive spark plasma sintering and reactive hot pressing. Scripta Materialia, 57(4), pp. 317-320.

[5] COSENTINO, I., MUCCILLO, E. and MUCCILLO, R., 2003. Development of zirconia-titania porous ceramics for humidity sensors. Sensors and Actuators B: Chemical, 96(3), pp. 677-683.

[6] RHODES, 1._.H., 1981. Agglomerate and Particle Size Effects on Sintering Yttria-Stabilized Zirconia. Journal of the American Ceramic Society, 64(1), pp. 19-22.

[7] RAHIMIAN, M., EHSANI, N. and PARVIN, N., 2009. The effect of particle size, sintering temperature and sintering time on the properties of Al–Al$_2$O$_3$ composites, made by powder metallurgy. Journal of Materials Processing Technology, 209(14), pp. 5387-5393.

[8] OH, I., NOMURA, N., MASAHASHI, N. and HANADA, S., 2003. Mechanical properties of porous titanium compacts prepared by powder sintering. Scripta Materialia, 49(12), pp. 1197-1202.

[9] WILKENHOENER, R., VASSEN, R., BUCHKREMER, H. and STÖVER, D., 1999. Mechanically alloyed Ni/8YSZ powder mixtures: preparation, powder characterization and sintering behavior. Journal of Materials Science, 34(2), pp. 257-265.

[10] KLEMENSØ, T., THYDÉN, K., CHEN, M. and WANG, H., 2010. Stability of Ni–yttria stabilized zirconia anodes based on Ni-impregnation. Journal of Power Sources, 195(21), pp. 7295-7301.

[11] HWANG, H.J., MOON, J., LEE, S. and LEE, E.A., 2005. Electrochemical performance of LSCF-based composite cathodes for intermediate temperature SOFCs. Journal of Power Sources, 145(2), pp. 243-248.

[12] MUCHTAR, A., HAMID, N.A., NORHAMIDI, M. and WAN DAUD, W.R., 2010. Sintering effects on LSCF cathodes for intermediate temperature solid oxide fuel cells (IT-SOFCs). Advanced Materials Research, 139, pp. 141-144.

[13] COLOGNA, M. and SGLAVO, V.M., 2010. Vertical sintering to measure the uniaxial viscosity of thin ceramic layers. Acta Materialia, 58(17), pp. 5558-5564.

[14] DE JONGHE, L. and RAHAMAN, M., 1984. Loading dilatometer. Review of scientific instruments, 55(12), pp. 2007-2010.

[15] BOCCACCINI, A.R., 1998. Shrinkage anisotropy of glass powder compacts sintered in dilatometers. Journal of Materials Research, 13(06), pp. 1693-1697.

[16] KENNEY, B., VALDMANIS, M., BAKER, C., PHAROAH, J. and KARAN, K., 2009. Computation of TPB length, surface area and pore size from numerical reconstruction of composite solid oxide fuel cell electrodes. Journal of Power Sources, 189(2), pp. 1051-1059.

[17] WILSON, J.R. and BARNETT, S.A., 2008. Solid oxide fuel cell Ni–YSZ anodes: effect of composition on microstructure and performance. Electrochemical and Solid-State Letters, 11(10), pp. B181-B185.

[18] KENNEY, B. and KARAN, K., 2007. Engineering of microstructure and design of a planar porous composite SOFC cathode: a numerical analysis. Solid State Ionics, 178(3), pp. 297-306.

[19] COBLE, R.L., 1973. Effects of Particle-Size Distribution in Initial-Stage Sintering. Journal of the American Ceramic Society, 56(9), pp. 461-466.

[20] BORDIA, R. and RAJ, R., 1985. Sintering behavior of ceramic films constrained by a rigid substrate. Journal of the American Ceramic Society, 68(6), pp. 287-292.

[21] OLLAGNIER, J., GUILLON, O. and RÖDEL, J., 2006. Viscosity of LTCC Determined by Discontinuous Sinter-Forging. International journal of applied ceramic technology, 3(6), pp. 437-441.

[22] MOHANRAM, A., MESSING, G.L. and GREEN, D.J., 2004. Measurement of Viscosity of Densifying Glass-Based Systems by Isothermal Cyclic Loading Dilatometry. Journal of the American Ceramic Society, 87(2), pp. 192-196.

[23] LEE, S., MESSING, G.L. and GREEN, D.J., 2003. Bending creep test to measure the viscosity of porous materials during sintering. Journal of the American Ceramic Society, 86(6), pp. 877-882.

[24] NI, D., ESPOSITO, V., SCHMIDT, C.G., MOLLA, T.T., ANDERSEN, K.B., KAISER, A., RAMOUSSE, S. and PRYDS, N., 2013. Camber Evolution and Stress Development of Porous Ceramic Bi-layers During Co-Firing. Journal of the American Ceramic Society, 96(3), pp. 972-978.

Chapter 5

In-situ Observation of Curvature Evolution during Co-sintering of Bi-layer Structures

5.1 Results

Experimentally, during the co-sintering of bi-layer structures, the curvature evolution of structures has occurred due to the different shrinkage behaviour and the viscosity variations between the two layers [1-5]. The results of curvature observations of bi-layer structures, whilst the total thickness varies, but the same thickness ratio was maintained, are shown in Figure 5.1. In-situ observation, to monitor the shrinkage of each material and the curvature evolution of the bi-layer structures, was carried out using a long focus microscope at specific temperatures up to 1200°C. The thickness of the bi-layer structures after the hot pressing was approximately 15% less than the sum of each green layer. Although some curvature evolutions occurred during the debinding stage (up to 700°C), this deformation was not considered in this study and only the curvature evolutions were investigated from 700°C to 1200°C. As the driving force of the deformation during the debinding process is only rearrangement of particles by burnout of additives without interactions between particles through mass transport, the mechanism of the deformation during the process was different from that during the sintering process. Furthermore, the deformation during debinding depends on various conditions of additives, so it should be investigated separately. From 700°C to 900°C, there was little change of curvature in all structures. The use of a curvature at 900°C as a zero point helped the understanding of curvature evolutions derived from sintering mechanisms. As the deformation from the debidning process was not considered in Cai's model, it was reasonable to compare curvature evolutions measured experimentally with the theoretical model. A positive curvature (which was defined for the curvatures towards the top layer of bi-layer structures) was developed from 900°C, when a bi-layer of NiO/CGO (top)-CGO

(bottom) was tested. After that, the curvature rate reduced while the maximum positive curvature was achieved at 1080°C ~ 1180°C. Then the curvature became negative as the bi-layer was curving towards bottom layer for the structure with 1:1 ratio. On the other hand, a bi-layer of CGO (top)-LSCF (bottom), developed negative curvature in the early stage, then rapidly formed a positive curvature after reaching the maximum curvature at 1020°C ~ 1120°C. The structures of with 1:1 and 3:3 ratios were severely warped, prior to reach the final temperature. So, their curvatures could not be totally included in the graph. In both experiments, it is seen that curvature evolution changed gradually towards CGO layer when temperature increases. That was because the higher shrinkage rate of the CGO layer during the later stage of sintering overwhelms the shrinkage rate of another layer. In addition, the peak point (maximum or minimum value) of each curvature was increased and shifted towards a higher temperature when overall thickness increases. It was attributed to the thinner structure in which the residual stress could be expressed easily through macro-deformation and the effect of gravity would be less than that of thicker structures, contributing to curvature evolution during the co-sintering process. The level of shrinkage mismatch of CGO-LSCF was higher than that of NiO/CGO-CGO, and so the curvature rate of CGO-LSCF was higher that cause quicker curvature developments as the temperature increases.

The curvature images of the bi-layer structures at 1000°C and 1200°C are shown in Figure 5.2. In NiO/CGO-CGO structures, the curvature with 1:1 layer shows rapid curvature change to bottom layer due to activation of shrinkage behaviour in CGO layer between 1000°C and 1200°C. Though other structures with 3:3 and 5:5 layers were maintained the curvature towards CGO layer at 1200°C, curvature behaviour had been already changed to NiO/CGO layer from 1150°C. In case of CGO-LSCF structures, the curvature evolutions were occurred towards CGO layer, and then changed to LSCF layer in the later stage of co-sintering. As the difference of shrinkage mismatch in CGO-LSCF was larger than NiO/CGO-CGO, some samples of CGO-LSCF were rolled at 1200°C.
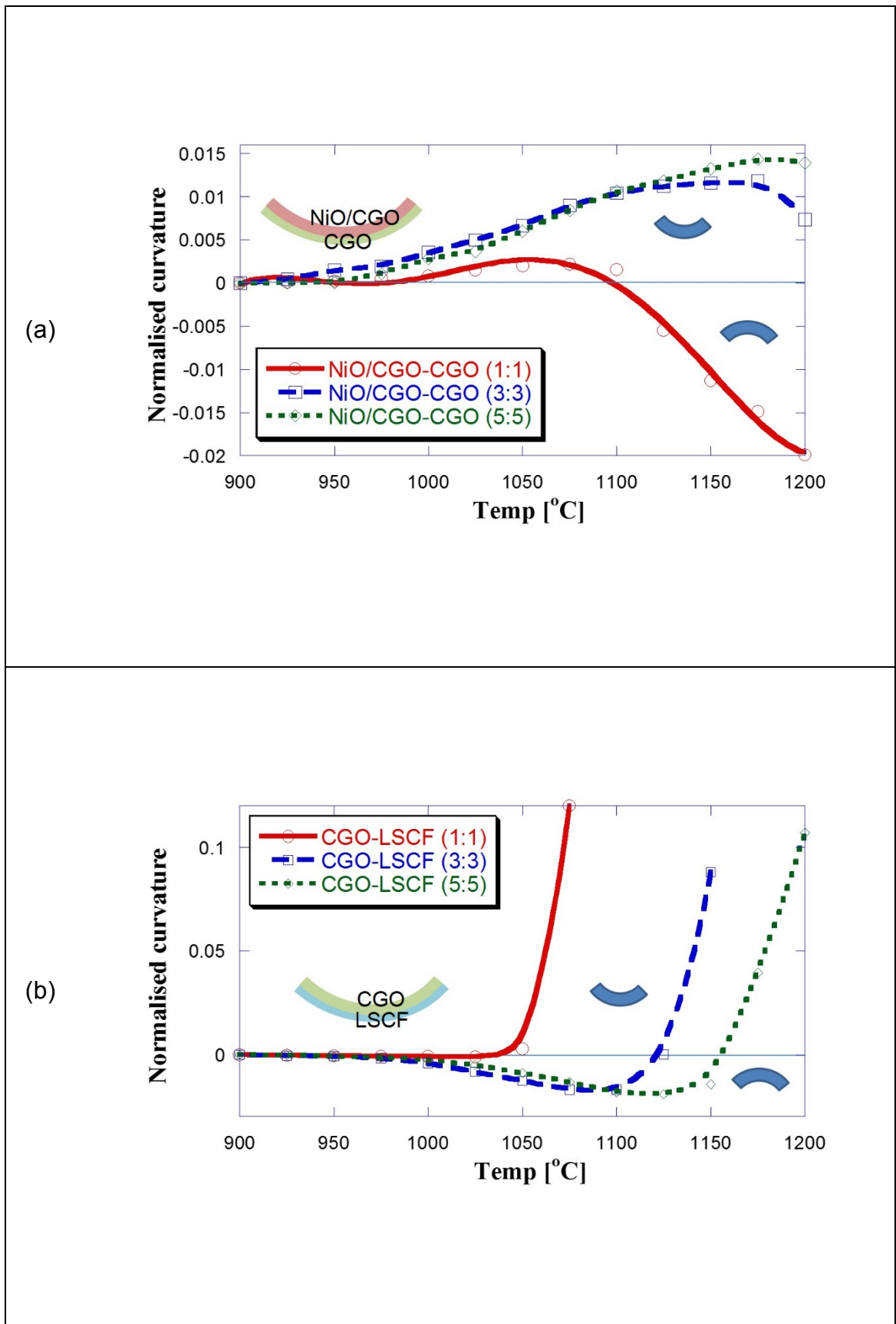
Figure 5.1 Normalised curvature of bi-layer structure: (a) NiO/CGO-CGO, (b) CGO-LSCF
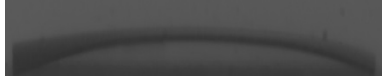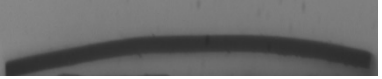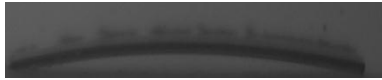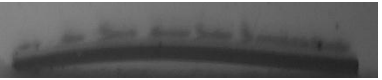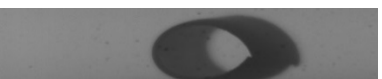
	Layers	1000°C	1200°C
(a) **NiO/CGO-CGO**	1:1		
	3:3		
	5:5		
(b) **CGO-LSCF**	1:1		
	3:3		
	5:5		

Figure 5.2 Normalised curvature images of bi-layer structure; (a) NiO/CGO-CGO and (b) CGO-LSCF

In the comparison of the normalised curvature rates between Cai's model and experimental results shown in Figure 5.3, it can be seen that the curvature rate of bi-layer structures showed similar trends (positive to negative rate for NiO/CGO-CGO and vice versa for CGO-LSCF). In case of the structures of CGO-LSCF with 1:1 and 3:3 ratios, normalised curvature rate could not be calculated due to severe warping. These results describe that total thickness as well as thickness ratio should be considered to predict the curvature evolution during co-sintering. In the structures of NiO/CGO-CGO, higher shrinkage of the NiO/CGO layer led to increased curvature rate of the bi-layer structures up to 1050°C, then decreased with increasing temperature.
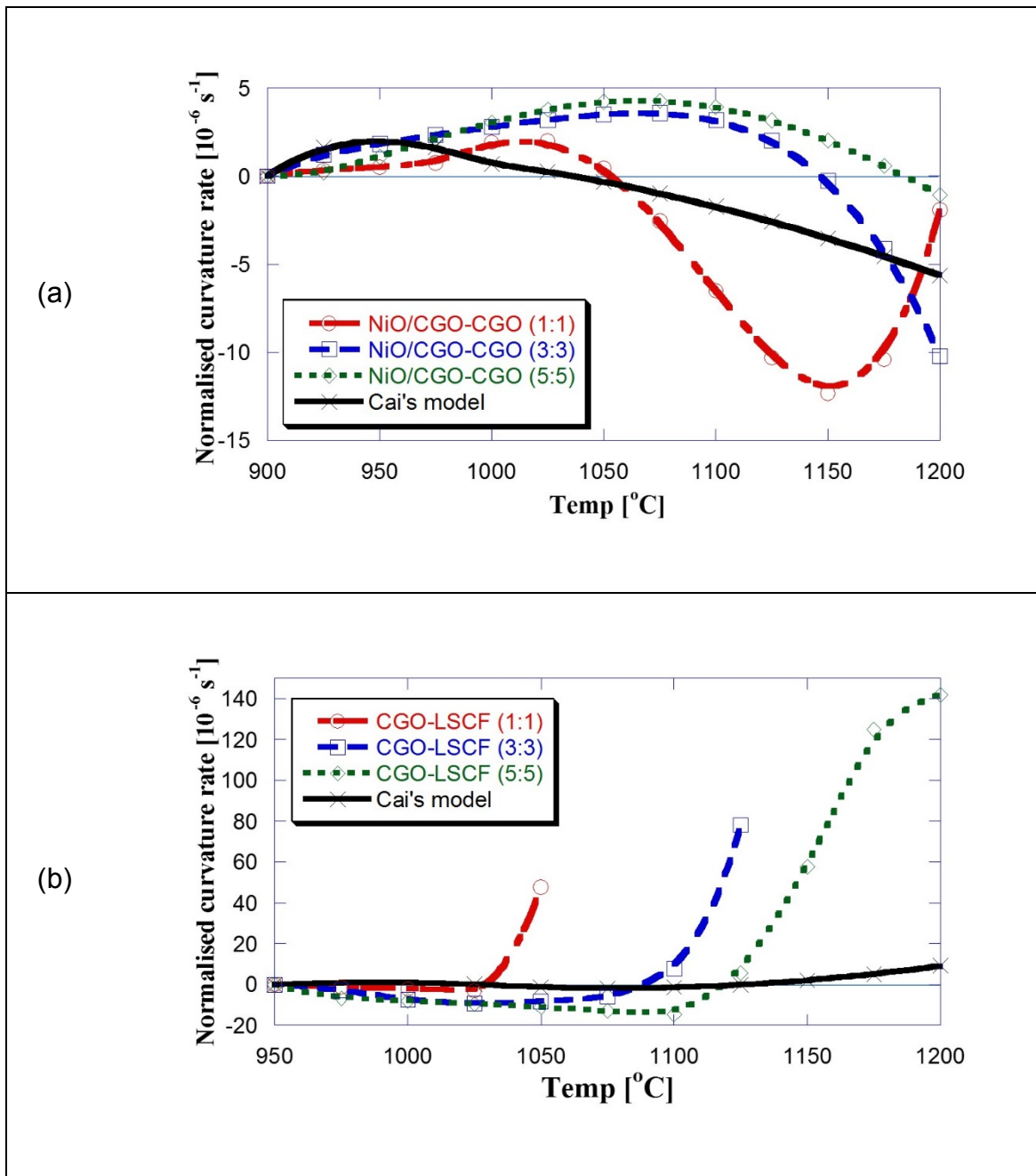
Figure 5.3 Normalised curvature rate: (a) NiO/CGO-CGO, (b) CGO-LSCF

Likewise, in CGO-LSCF structures, LSCF layer led initial curvature rate, then it was overwhelmed by the sintering behaviour of CGO layer. As the total thickness of structure increased, maximum curvature rate was shifted to higher temperatures. It is noticeable that some level of discrepancy has developed between the theoretical approach using Cai's model and the experimental results by in-situ observation. Different curvature rates were observed for thicker samples of the same bi-layer material which had the same thickness ratio. This could be attributed to residual stresses at the interface of thicker

structures might be different from that of a thin structure, even using the same materials with the same thickness ratio [36-38]. In addition, effects due to gravity with increasing thickness on the retardation of curvature evolution should be considered [9, 10]. Macro-scale deformation can be easily expressed in thin structure due to its low stiffness, whereas thicker structures have higher tolerance against the deformation. [11, 12]. This effect was not regarded in Cai's model. In the experimental approach, each factor might not be constant during co-sintering. For instance, when a curvature occurred, the thickness of the layer under compression was respectively thicker than the layer under tension. Likewise, the difference of strain rate changed depending on curvature evolution state during the co-sintering of the bi-layer structure. So, three correlation factors, variable from 0.8 to 1.2, were applied to Cai's data, shown in Equation (5.1), to compare with experimental data. The normalised curvature rate in Cai's model consists of thickness ratio, m, viscosity ratio, n, and strain rate difference, $\Delta\dot{\varepsilon}$. Using three correlation factors, α, β, γ with a range of 0.8~1.2, the influence of each factor can be investigated on the determination of normalised curvature rate, so as to compare experimental data. Three corresponding factors in Equation (2.10) is now replaced with αm, βn, and γ$\Delta\dot{\varepsilon}$. The modified equation is

$$\dot{k} = \left[\frac{6(\alpha m + 1)^2 \alpha m \beta n}{(\alpha m)^4 (\beta n)^2 + 2\alpha m \beta n (2(\alpha m)^2 + 3\alpha m + 2) + 1} \right] \gamma \Delta\dot{\varepsilon} \qquad (5.1)$$

The effect of correlation factors is shown in Figure 5.4 along with experimental curvature plots. The influence of a correlation factor to the thickness ratio is investigated first. The correlation factor α is variable from 0.8 to 1.2 with a 0.1 increment whilst the β, γ are fixed as 1. A comparison to the NiO/CGO-CGO bi-layer structures with their variable total thicknesses (1 ~ 5) is given in Figure 5.4a. The factor on thickness ratio influences to increase the maximum normalised curvature rate. But, the factor affects little to the behaviour of curvature rate after reaching to the maximum point. Similarly, a variable β is calculated and shown in Figure 5.4b. The variable β has brought only little impact to the curvatures. When the γ is applied with the same variable range, the calculated curvatures show not only the increase of the maximum

rate, but also faster curvature rate in Figure 5.4c. In summary, the influence of correlation factors shows that normalised curvature evolutions in experimental data are sensitive to each individual factor which can be variable depends on curvature evolution state, whereas all they are constants in Cai's model.

As a result, the curvature rate was increased when higher correlation factors were applied on thickness ratio and strain rate difference, shown in the Figure 5.4. In summary, in the comparison with experimental results, the curvature rate of the structure consisting of thicker layers would be vulnerable to variation of thickness ratio and strain rate. In case of shift action to higher temperature, it depends on the strain rate mismatch between layers and the stiffness of each layer (functions of viscosity, viscous Poisson's ratio and thickness).

A sintering process gives rise to different stress levels in each layer. Hence there is a mismatch of stresses between layers and the maximum sintering mismatched stress occurs at the interface of the bi-layer structure. Maximum sintering mismatched stress at the interface of bi-layer structures was calculated using Equations 5.1 and 5.2 with experimentally obtained shrinkage and curvature rates respectively.

The results are as shown in Figure 5.5. In the structure of NiO/CGO-CGO, positive mismatched stress (tensile stress) occurred in the early stages of co-sintering and then reversed to become negative stress (compressive stress) later in the co-sintering process. Likewise, compressive stress was observed in the CGO-LSCF structure and then reversed to tensile stress with increasing temperature. Both graphs show that stress switching points (from tensile to compressive or vice versa) are consistent with the peak of the shrinkage graphs. As macro-deformation of the structure with increasing thickness was reduced during co-sintering, stress variation at the interface was small compared with thin structure. During co-sintering the stress mismatch between layers of the bi-layer structures did not give rise to any significant defects such as cracking or delamination. That's because the driving force of free sintering, called sintering stress, was greater than the mismatched sintering stresses occurred during the co-sintering process [13].

(a)

(b)

(c)
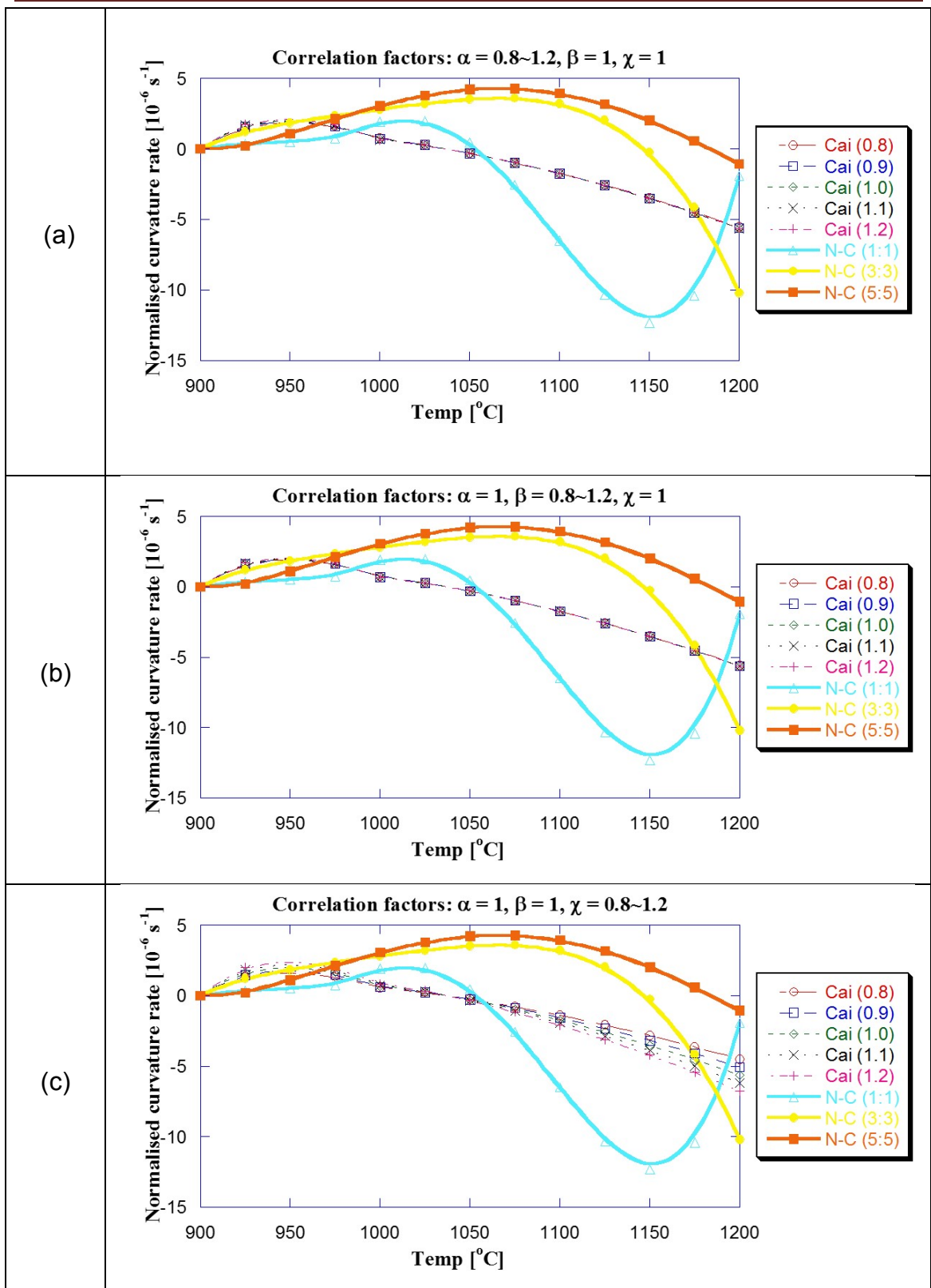
Figure 5.4 Comparisons of normalised curvature rate between experimentally observed results and the calculated results applying correlation factors to the Cai's model
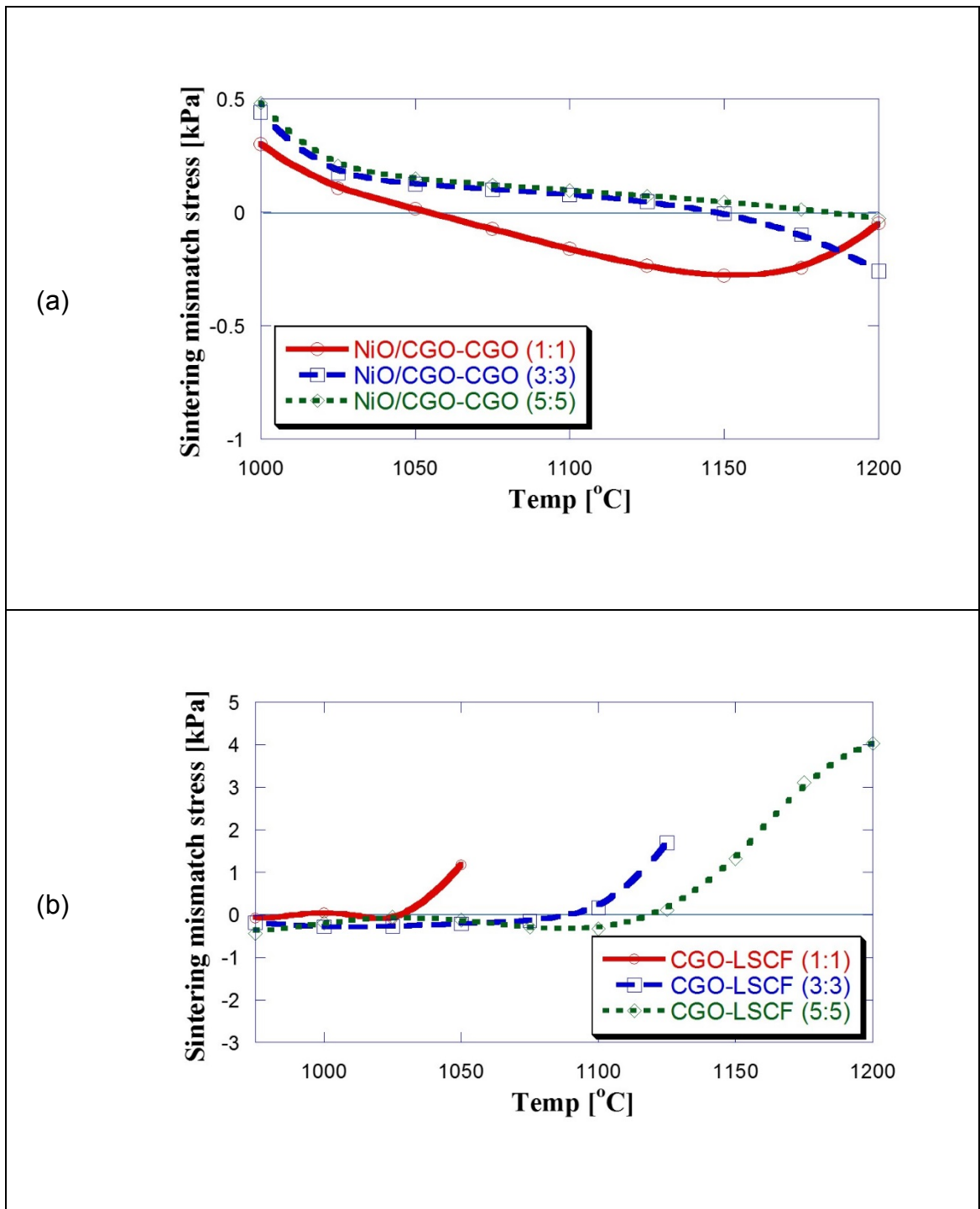
Figure 5.5 Sintering mismatch stress of bi-layer structure: (a) NiO/CGO-CGO,
(b) CGO-LSCF

A total thickness of 4 and 12 layers with different thickness ratio values for the bi-layer structure are further investigated for curvature evolution versus co-sintering temperature with the results shown in Figures 5.6. The graphs

shown in Figure 5.6 (a) for NiO/CGO-CGO structure are for material thickness ratios of 1:3; 2:2; and 3:1 with Figure 5.6 (b) showing a tripling of these values.
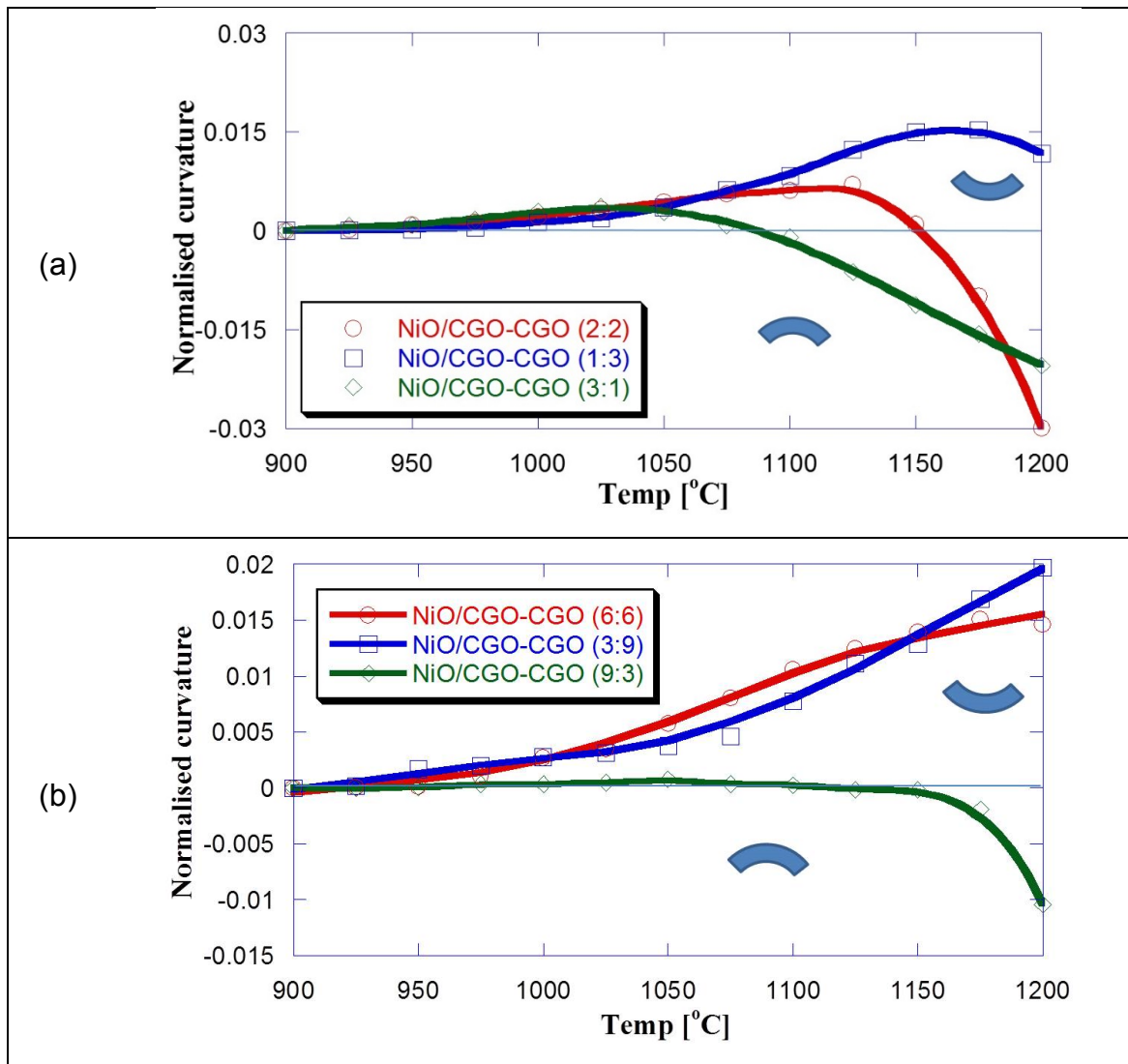
Figure 5.6 Curvature evolution of NiO/CGO-CGO bi-layer structures

When one layer is thicker in a bi-layer structure, the through thickness shrinkage stress increases, contributing to a reduction of the in-plane shrinkage stress during co-sintering. The curvature of the bi-layer structure with a larger thickness (Figure 5.6 (b)) is be influenced by the relatively higher in-plane shrinkage stress of the thin layer [14, 15]. The thicker bi-layer structures with different thickness ratios show a similar trend when compared to Figure 5.6 (a). As the total thickness of the bi-layer structures increased the curvature evolution behaviour shifted to a higher temperature. The comparison of curvature images at 1000°C and 1200°C is shown in Figure 5.7. It should be

noted that the debinding process from room temperature to the start of co-sintering results in a small amount of curvature. The start of co-sintering is considered to be 900°C.
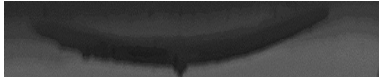
Layers	1000°C	1200°C
NiO/CGO-CGO (1:3)		
NiO/CGO-CGO (3:1)		
NiO/CGO-CGO (3:9)		
NiO/CGO-CGO (9:3)		

Figure 5.7 Curvature images of NiO/CGO-CGO bi-layer structure at 1000°C and 1200°C

Figure 5.8 shows a similar set of results with CGO-LSCF structure. Considering the NiO/CGO-CGO structures the shrinkage of the NiO/CGO layer was faster than the CGO layer in the early stages of co-sintering which led to the positive curvature of the bi-layer structure i.e. curving towards the NiO/CGO layer, regardless of thickness ratios. In the later stages of co-sintering the bi-layer structures reduced in curvature and eventually were reversed and began curving towards the CGO layer for thickness ratios 1:3 and 3:1. The graph plotted for the thickness ratio 2:2 was in fact obtained from interpolating the experimental results with thickness ratios 1:1 and 3:3 (see Figure 5.1). These numerical results suggest that the shrinkage of the NiO/CGO layer is greater than the CGO layer up to 1125°C whereupon the shrinkage of CGO layer increases rapidly which leads to a significant curvature change of the bi-layer structure towards the CGO layer. On the basis of the results of this structure,

consisting of 2 layers NiO/CGO and 2 layers CGO led to experimental investigation into the curvature evolution of bi-layer structures with the thickness ratios 1:3 and 3:1. When comparing to the 2:2 thickness ratio the structure, consisting of 3 layers NiO/CGO and 1 layer CGO, exhibited different behaviour with the curvature reducing at a lower temperature. On the other hand, the curvature reduction point for the structure, consisting of 1 layer NiO/CGO and 3 layers CGO was shifted to a higher temperature. This leads to the corollary that the shrinkage of the thinner layer in bi-layer structure is significant in determining curvature evolution.
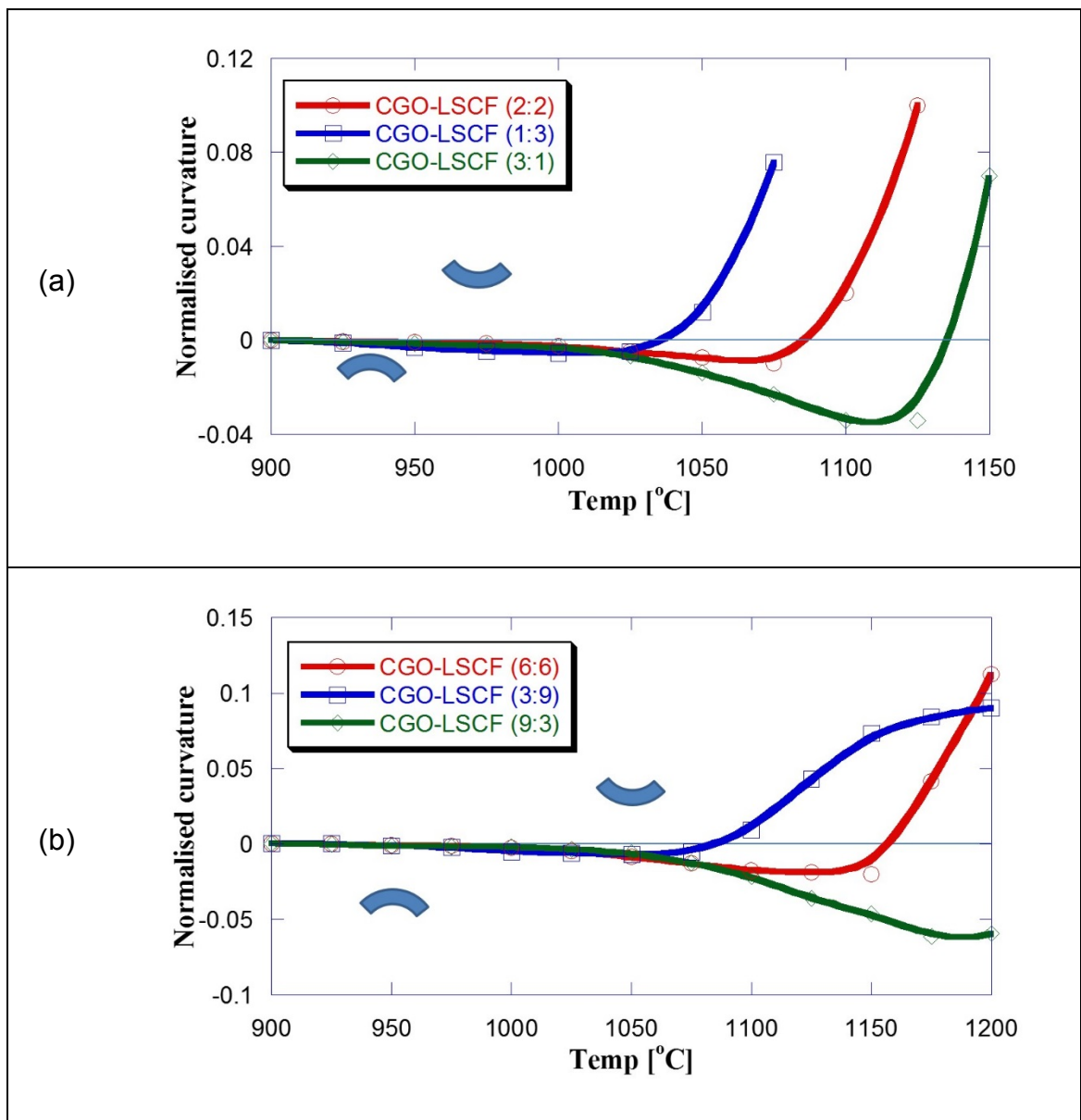
Figure 5.8 Curvature evolution of CGO-LSCF bi-layer structure

In the CGO-LSCF structures, the in-plane shrinkage stress of the thin layer in the bi-layer structures was dominant so that curvature evolution towards the thin layer was more active during co-sintering. The curvatures of CGO-LSCF structures had higher magnitudes than the NiO/CGO-CGO structures due to significant differences in the material properties [16]. In the case of curvature evolution of the structures with a total of 12 layers, a definite trend from different thickness ratio in bi-layer structure is seen in Figure 5.8 (b). In all samples, the curvature evolutions were towards the LSCF layer in the early stages of co-sintering. The structure, consisting of 3 layers CGO and 9 layers LSCF, was curved towards the CGO layer from 1050°C and showed a curvature change point at 1200°C. In contrast to this the curvature of the structure, consisting of 9 layers CGO and 3 layers LSCF, had curvature towards the LSCF layer until 1200°C. Figure 5.9 shows curvature images of CGO-LSCF structures at 1000°C and 1200°C. The final shapes of CGO-LSCF structures with total 4 layers were severely warped or rolled, compared with the NiO/CGO-CGO structures.
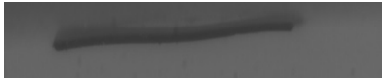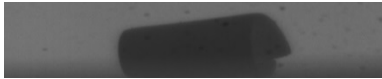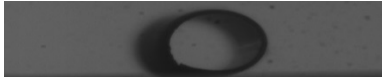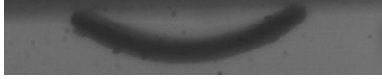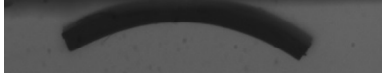
Layers	1000°C	1200°C
CGO-LSCF (1:3)		
CGO-LSCF (3:1)		
CGO-LSCF (3:9)		
CGO-LSCF (9:3)		

Figure 5.9 Curvature images of CGO/LSCF bi-layer structure at 1000°C and 1200°C

5.2 Discussion

Curvature Evolution of Bi-layer Structures

The difference in shrinkage behaviour between layers during co-sintering stems from the materials being chemically different or having different physical characteristics that affect the shrinkage behaviour such as initial particle size and green density. Therefore, modification of the shrinkage behaviour due to the existence of another material in physical contact should be performed to meet the compatibility conditions [17]. In the geometrical approach, the shrinkage behaviour of the films or multi-layer structures during co-sintering is characterised by the much larger in-plane dimensions than the thickness. Compared to unconstrained shrinkage behaviour of the two layers, the different shrinkage behaviour of the two layers in a bi-layer structure put under the constraint of deformation which leads to a variety of defects and shape distortion including warping, growth of cracks and delamination.

Prior to curvature evolution of the bi-layer structure during co-sintering, the stress is constant through the thickness direction. The larger the difference in shrinkage behaviour between layers results in a higher stress occurred. To reduce a higher stress distribution for avoidance of other defects, curvature of the bi-layer structure is generated, leading to non-homogeneous stress distribution through the thickness direction in the structure (i.e. compressive stress at the top surface and tensile stress at bottom surface).

Unlike the constrained sintering in which high Young's modulus of the substrate and thin layer on the substrate are applied, the geometry including the relative thickness of the different layers is an important factor in the co-sintering process. At the early stage of co-sintering, a low Young's modulus and thicker layer could easily lead the bi-layer structure to cracking or delamination by curvature evolution.

Thickness Effect

The co-sintering process with the anode and electrolyte has been widely utilised in a variety of SOFC research, due to similar characteristic features of the materials [18, 19]. In this study, the curvature evolution of the bi-layer structure — consisting of the anode and electrolyte — was developed upon the co-sintering process. As mentioned previously, various components including powder material, binder and dispersant in the tape-casting slurries could induce different shrinkage behaviour in the bi-layer structure during co-sintering, although similar materials were used. As the thin bi-layer structure had lower stiffness than bulky samples, it appeared that the curvature evolution was very sensitive depending on the difference of shrinkage behaviour. This derived from the fact that the presence of NiO powder in the anode slowed down the shrinkage rate. Some experimental results indicate that adding a fraction of fine powders to coarser powder helps to reduce the curvature evolution and the difference in shrinkage behaviour [20].

Comparison with Cai's model

On the basis of the properties measured via the optical method, the shrinkage rate of bi-layer structures was compared to the results calculated by Cai's model using Equation 5.2. The curvature rate of a bi-layer structure depends on the sintering rate mismatch between layers and the stiffness of each layer as functions of viscosity, viscous Poisson's ratio, and thickness. Although the inversion of the curvature rate showed a similar pattern, it did not express curvature behaviours depending on total thicknesses. This was attributed to the different shrinkage behaviour derived from different thicknesses under the thickness ratio of 1. It was related to uniaxial viscosity and different curvature rates were finally measured. As viscosity does not depend on thickness but only on density and temperature, different green densities may occur during fabrication of bi-layer structures using the hot-pressing method [21, 22]. Under the same pressure and holding time, the thicker the structure, the higher green density might be reached, due to a rearrangement of microstructural compositions. Therefore, a higher green

density allowed for a strong sinterability of the materials, resulting in enhanced curvature evolution during co-sintering. The mismatched sintering stress was calculated using Equation 5.1. It was shown that the stress at the interface in the bi-layer structures depended on thickness: usually the thinner the layer, the higher the stress.

Thickness Ratio Effect

Different thickness ratios mainly affect differences in viscosity and stiffness of the bi-layer structure being tolerant to the deformation derived from curvature evolutions [23]. Under the same total thickness condition, the curvature evolutions of the bi-layer structure showed improvement of bending behaviour, during co-sintering, as compared to thin layer. It was reconfirmed that the thinner layer on a substrate with low stiffness had higher stress and acted as a considerate determinant for curvature evolution. In comparison to thicker bi-layer structures with same thickness ratio, it was found that the curvature evolutions shifted to high temperatures due to enhancement of stiffness.

5.3 Summary

The curvature evolutions in bi-layer structures, as functions of thickness and thickness ratio, were investigated. It is well known that the curvature behaviour of the structure is influenced by the difference of viscosities between layers, as well as over stiffness. Beyond a critical point during co-sintering, the structures may begin to crack or exhibit delamination. Below this point, the mismatched stresses derived from the differences of properties between layers induce curvature evolution to relax the stresses. The optical observation has been carried out to identify macro-deformation behaviour under the conditions of thickness and thickness ratios in the structure. The thicker the bi-layer structure, the higher the stiffness of the structure. A curvature change point was thereby increased and shifted to a high temperature. In addition, compared to Cai's model, a similar curvature rate pattern was shown. However, different curvature evolutions depending on total thicknesses developed due to increased initial green density caused by the hot-pressing method. In the graphs of mismatched sintering stress, it was definitely shown that the thinner structure showed higher stress at the interface. In the results comparing different thickness ratios, the shrinkage stress of the thinner layer was a main factor for determining the curvature behaviour of the bi-layer structure. The characteristic of curvature evolution in thin structures was similar to the curvature results found in thicker structures.

References

[1] CAI, P.Z., MESSING, G.L. and GREEN, D.J., 1997. Determination of the mechanical response of sintering compacts by cyclic loading dilatometry. Journal of the American Ceramic Society, 80(2), pp. 445-452.

[2] CAI, P.Z., GREEN, D.J. and MESSING, G.L., 1997. Constrained densification of alumina/zirconia hybrid laminates, II: viscoelastic stress computation. Journal of the American Ceramic Society, 80(8), pp. 1940-1948.

[3] LI, W. and LANNUTTI, J.J., 2005. Curvature evolution in LTCC tapes and laminates. Components and Packaging Technologies, IEEE Transactions on, 28(1), pp. 149-156.

[4] LANKIN, M.K. and KARAN, K., 2009. Effect of Processing Conditions on Curvature of Anode/Electrolyte SOFC Half-Cells Fabricated by Electrophoretic Deposition. Journal of fuel cell science and technology, 6(2), pp. 021001.

[5] LI, W., HASINSKA, K., SEABAUGH, M., SWARTZ, S. and LANNUTTI, J., 2004. Curvature in solid oxide fuel cells. Journal of Power Sources, 138(1), pp. 145-155.

[6] WANG, W., FU, Z., WANG, H. and YUAN, R., 2002. Influence of hot pressing sintering temperature and time on microstructure and mechanical properties of TiB2 ceramics. Journal of the European Ceramic Society, 22(7), pp. 1045-1049.

[7] YANG, J., ZHANG, G. and OHJI, T., 2001. Porosity and microstructure control of porous ceramics by partial hot pressing. Journal of Materials Research, 16(07), pp. 1916-1918.

[8] PARK, J., LEE, Y., KOH, Y., KIM, H. and SU BAEK, S., 2000. Effect of Hot-Pressing Temperature on Densification and Mechanical Properties of Titanium Diboride with Silicon Nitride as a Sintering Aid. Journal of the American Ceramic Society, 83(6), pp. 1542-1544.

[9] FRANDSEN, H.L., OLEVSKY, E., MOLLA, T.T., ESPOSITO, V., BJØRK, R. and PRYDS, N., 2013. Modeling sintering of multilayers under influence of gravity. Journal of the American Ceramic Society, 96(1), pp. 80-89.

[10] MOLLA, T.T., NI, D.W., BULATOVA, R., BJØRK, R., BAHL, C., PRYDS, N. and FRANDSEN, H.L., 2014. Finite Element Modeling of Camber Evolution

During Sintering of Bi-layer Structures. Journal of the American Ceramic Society.

[11] LEE, S., MESSING, G.L. and GREEN, D.J., 2004. Warpage evolution of screen printed multilayer ceramics during co-firing. Key Engineering Materials, 264, pp. 321-330.

[12] CHANG, J., GUILLON, O., RÖDEL, J. and KANG, S.L., 2008. Characterization of warpage behaviour of Gd-doped ceria/NiO–yttria stabilized zirconia bi-layer samples for solid oxide fuel cell application. Journal of Power Sources, 185(2), pp. 759-764.

[13] CHIANG, M., JEAN, J. and LIN, S., 2011. Effects of green density difference on camber development during the cofiring of a bi-layer glass-based dielectric laminate. *Materials Chemistry and Physics,* **128**(3), pp. 413-417.

[14] HAGYMÁSI, M., ROOSEN, A., KARMAZIN, R., DERNOVSEK, O. and HAAS, W., 2005. Constrained sintering of dielectric and ferrite LTCC tape composites. Journal of the European Ceramic Society, 25(12), pp. 2061-2064.

[15] LEE, W. and SU, C., 2007. Improvement in the Temperature Stability of a BaTiO3-Based Multilayer Ceramic Capacitor by Constrained Sintering. Journal of the American Ceramic Society, 90(10), pp. 3345-3348.

[16] NAGAMORI, M., SHIMONOSONO, T., SAMESHIMA, S., HIRATA, Y., MATSUNAGA, N. and SAKKA, Y., 2009. Densification and Cell Performance of Gadolinium-Doped Ceria (GDC) Electrolyte/NiO–GDC Anode Laminates. Journal of the American Ceramic Society, 92(s1), pp. S117-S121.

[17] BORDIA, R.K., ZUO, R., GUILLON, O., SALAMONE, S.M. and RÖDEL, J., 2006. Anisotropic constitutive laws for sintering bodies. Acta materialia, 54(1), pp. 111-118.

[18] CHENG, T. and RAJ, R., 1989. Flaw Generation During Constrained Sintering of Metal-Ceramic and Metal–Glass Multilayer Films. Journal of the American Ceramic Society, 72(9), pp. 1649-1655.

[19] LEE, S., MESSING, G.L. and AWANO, M., 2008. Sintering Arches for Cosintering Camber-Free SOFC Multilayers. Journal of the American Ceramic Society, 91(2), pp. 421-427.

[20] COLOGNA, M., SGLAVO, V.M. and BERTOLDI, M., 2010. Sintering and deformation of solid oxide fuel cells produced by sequential tape casting. International Journal of Applied Ceramic Technology, 7(6), pp. 803-813.

[21] RAVI, D. and GREEN, D.J., 2006. Sintering stresses and distortion produced by density differences in bi-layer structures. Journal of the European Ceramic Society, 26(1), pp. 17-25.

[22] KANTERS, J., EISELE, U. and RÖDEL, J., 2001. Cosintering simulation and experimentation: case study of nanocrystalline zirconia. Journal of the American Ceramic Society, 84(12), pp. 2757-2763.

[23] HSU, R. and JEAN, J., 2005. Key Factors Controlling Camber Behavior During the Cofiring of Bi-Layer Ceramic Dielectric Laminates. Journal of the American Ceramic Society, 88(9), pp. 2429-2434.

Chapter 6

In-situ Observation of Curvature Evolution during Co-sintering of Triple-layer Structures

6.1 Results

The curvature evolutions of triple-layer structures are shown in Figure 6.1. The total number of tape-casting layers used for the structures were from 5 layers (NiO/CGO-CGO-LSCF with 1:3:1 layers) to 21 layers (NiO/CGO-CGO-LSCF with 9:3:9 layers). Through the comparison of graphs, it is observed that a definite curvature trend of triple-layer structures occurred from 1025°C. As with the curvature patterns of bi-layer structures, the onset points of curvature evolution in thicker triple-layer structures were shifted towards a higher temperature range due to the increase of stiffness against curvature development [1, 2]. Considering the curvature evolutions of the bi-layer structures with NiO/CGO (top) – CGO (bottom) or CGO (top) – LSCF (bottom), they were mostly biased towards the top layer at 1200°C. The magnitude of curvatures of CGO-LSCF structures was higher than NiO/CGO-CGO structures. This was attributed to the fact that the mismatch of shrinkage behaviour at the interface in CGO-LSCF structures was larger than that of the NiO/CGO-CGO structures. This followed from the final curvature shapes of the triple-layer structures (NiO/CGO (top) | CGO | LSCF (bottom)) being formed at the top layer, especially towards NiO/CGO layer. In various thickness compositions, only the structure, consisting of 1 layer for NiO/CGO, 3 layers for CGO, and 9 layers for LSCF, was significantly curved towards the LSCF layer at the final temperature. In the case of curvature evolutions of bi-layer structures, such as NiO/CGO-CGO with 1:3 layers, and CGO-LSCF with 3:9 layers, both structures demonstrated curvature evolution towards the LSCF layer at 1200°C. This trend was reflected to the curvature pattern of the triple-layer structure, consisting of NiO/CGO-CGO-LSCF with 1:3:9 layers during co-sintering. Although the

curvature evolution of the electrolyte layer was affected at the same time by the anode and cathode layer during the co-sintering of the triple-layer structure, and total stiffness was increased compared to bi-layer structures, there were no barriers to determine the final curvature biased to the cathode layer. This shows behaviour paralleling that of the bi-layer structure curvature directions, depending on temperatures during co-sintering.

The thickness effect for curvature development during the co-sintering of triple-layer structure was clearly demonstrated in Figure 6.1 (a, b, d) and (f, g, h). The number of NiO/CGO layers was used as an important variable for comparison. As the thickness of the NiO/CGO layer increased in the triple-layer structure, the stress for curvature towards the NiO/CGO layer decreased, contributing to the increase of curvature evolution to the LSCF layer at the final temperature. In addition, high stiffness caused by a thicker structure reduced the magnitude of curvature evolution. As discussed in Chapter 5, it was shown that a thin layer among three component layers acted as a dominant factor for the determination of the curvature evolution of a triple-layer structure [3, 4].

In Figure 6.1 (c) and (e), different thickness of the electrolyte layer was applied to decide curvature evolution of the triple-layer structure. Under these conditions, the curvature evolution of bi-layer structures was reflected and conflicted with each other during the co-sintering of the triple-layer structure. As the stress for curvature of the CGO-LSCF structure was larger than that of NiO/CGO-CGO structure, the entire curvature pattern of the triple-layer structure was obligated by a dominant curvature evolution of CGO-LSCF bi-layer structures. The CGO-LSCF structure showed severe curvature evolution during co-sintering, although its curvature pattern was not directly reflected to the curvature of the triple-layer structure due to an increase in overall stiffness and the interaction with the electrolyte layer [5, 6].

In comparisons of the triple-layer structures having same thickness with different thickness ratios, Figures 6.1 (c, g), (b, e), and (d, f) show the effect of thickness ratios for curvature evolution of triple-layer structures. It was clearly shown that if the thickness of one layer was already fixed among three component layers, the thickness ratio of the other layers played an important role for curvature evolution of the triple-layer structure. In other words, the

thinnest layer in a triple-layer structure played a significant role for determining curvature evolution during co-sintering [7, 8].
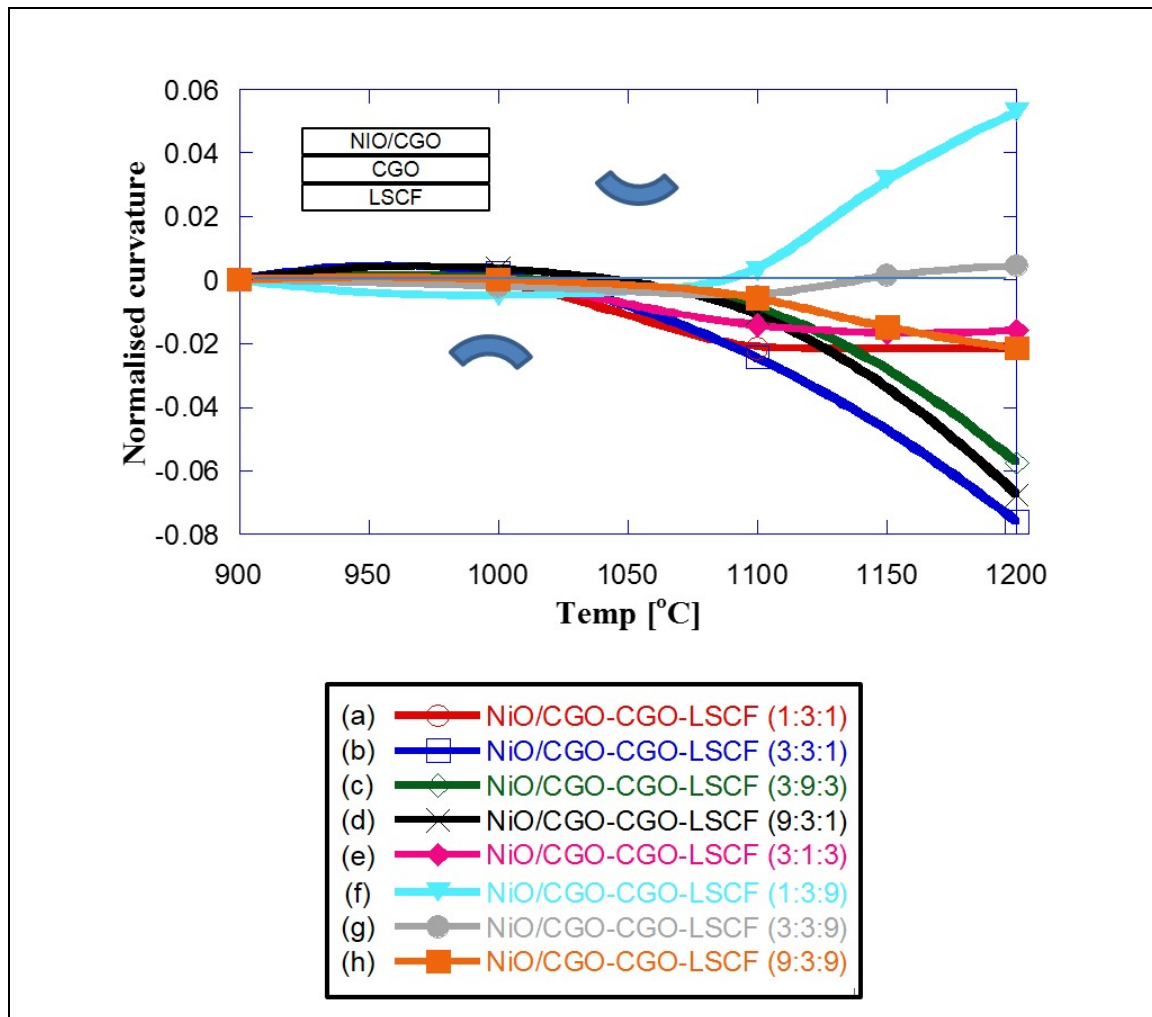
Figure 6.1 Curvature evolutions of triple-layer structures under different thickness (ratio) conditions

Prediction of Curvature Evolution of a Triple-layer Structure based on Bi-layer Curvatures

The curvature prediction of triple-layer structures was calculated based on the sum of bi-layer structure curvatures, described in Chapter 5. These results were compared with experimental curvature observations of triple-layer structures, consisting of the same structural conditions as in bi-layer structures. Figure 6.2 ~ 6.9 show comparisons of curvature evolution between calculated prediction and experimental observation of the triple-layer structure.

Case I – Thickness ratio (1:3:1)

The curvature comparison of NiO/CGO | CGO | LSCF with 1:3:1 layers is shown in Figure 6.2. The curvature prediction derived from bi-layer structures and the experimental observation of the triple-layer structure show similar trend up to 1100°C, showing curvature towards the LSCF layer. After 1100°C, the prediction line was significantly curved to the NiO/CGO layer due to a higher curvature evolution of the CGO-LSCF structure with increasing temperature. Although the stiffness of the bi-layer structure against curvature development during co-sintering was different from the triple-layer structure, the curvature evolution of the triple-layer structure was nevertheless predicted to curve towards the NiO/CGO layer at the final temperature. In the experimental result of curvature evolution for triple-layer structures, the changing point of curvature direction occurred at 1100°C, in accordance with the curvature prediction. However, the curvature of the triple-layer structure did not rapidly change towards the NiO/CGO layer and remained constant up to 1200°C. A possible reason for the curvature evolution of triple-layer structure showing different a pattern as compared to the sum of bi-layer structures may be the increase of total thickness, relating to mechanical stiffness, interaction of the CGO layer and stress distribution derived from different microstructures in the thicker structure [9-11].

Figure 6.2 Curvature prediction calculated from bi-layer structures and experimental results of triple-layer structure, consisting of NiO/CGO-CGO-LSCF with 1:3:1 layers

Case II – Thickness ratio (3:3:1)

Figure 6.3 shows curvature results of NiO/CGO | CGO | LSCF with 3:3:1 layers. In the curvature evolution of the NiO/CGO-CGO structure with 3:3 layers, the thickness ratio and increased total thickness leaded to reduce curvature evolution towards the NiO/CGO layer as compared to that of the NiO/CGO-CGO with 1:3 layers. As there was little influence of the NiO/CGO-CGO for determination of curvature evolution of the triple-layer structure, curvature prediction of the triple-layer structure was shown to be similar up to 1100°C and severe curving of the CGO-LSCF structure from 1100°C was shown in Figure 6.2. On the other hand, experimental results showed continuous curvature evolution to the NiO/CGO layer with increasing temperature. The stress derived from the shrinkage behaviour of the LSCF layer in the triple-layer structure acted as a leading factor for curvature evolution. Even though the triple-layer structure with 3:3:1 layers had higher stiffness than that of the triple-layer structure with 1:3:1 layers, it showed a higher curvature evolution with increasing temperature. As discussed above in curvature evolution of the bi-layer structures, the thinner layer in the triple-layer structure had higher stress, contributing to curvature development of the structure during co-sintering. In addition, as material properties of the NiO/CGO layer were almost similar to the CGO layer, increased thickness of the NiO/CGO layer made an effect that a ratio of the thickness of the LSCF layer to total thickness was relatively reduced. The stress of the LSCF layer was thereby increased, resulting in curvature evolution toward the LSCF layer with increasing temperature.

Figure 6.3 Curvature prediction calculated from bi-layer structures and experimental results of the triple-layer structure, consisting of NiO/CGO-CGO-LSCF with 3:3:1 layers

Case III – Thickness ratio (3:9:3)

The curvature evolution of NiO/CGO | CGO | LSCF with 3:9:3 layers is shown in Figure 6.4. This structure consisted of a total of 15 layers and 3 times the thickness condition as compared to the structure with 1:3:1 layers in Figure 6.2. As the thickness of the bi-layer structures increased with the same thickness ratio, the curvature evolution of the triple-layer structure initiated at a higher temperature and had a slightly increased magnitude. As the thickness of the bi-layer structures consisting of the triple-layer structure increased, a severe curvature change was not found, as compared to the curvatures of bi-layer structures shown in Figure 6.2. The curvature prediction of the triple-layer structure from the sum of curvatures of bi-layer structures was shown to curve towards the LSCF layer during co-sintering. The experimental observations of the triple-layer structure displayed good agreement with the predicted values in this thickness condition. The curvature prediction increased its curvature behaviour towards the LSCF layer up to 1175°C and then reduced due to curvature evolutions of the bi-layer structures. However, experimental results of the triple-layer structure showed curvature behaviour towards the LSCF layers up to 1200°C. Even though there was quantifiable difference at the final temperature, both graphs show similar curvature evolution during co-sintering. Given that the graphs for the predictions show close correlation with the experimental results, this may indicate that moderate stress distribution occurred, resulting in less vulnerability to radical microstructural change during the co-sintering process.
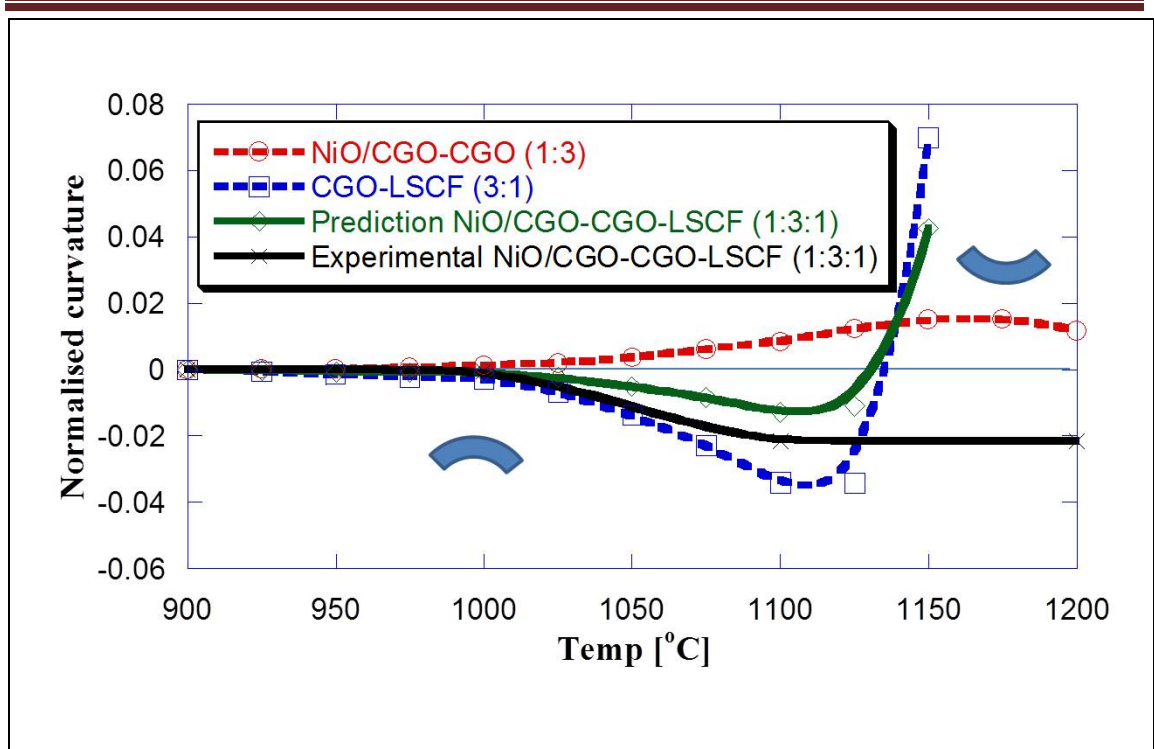
Figure 6.4 Curvature prediction calculated from bi-layer structures, and experimental results of the triple-layer structure, consisting of NiO/CGO-CGO-LSCF with 3:9:3 layers

Case IV – Thickness ratio (9:3:1)

Figure 6.5 shows curvature evolution of a triple-layer structure, consisting of NiO/CGO | CGO | LSCF with 9:3:1 layers. On the basis of the effect of the thickness ratio in bi-layer structures, curvature evolution of the triple-layer structure was expected to curve towards the NiO/CGO layer at the final temperature, while the curvature change in the prediction graph occurred at 1125°C. However, in the experimental observations, the curvature evolution developed towards the LSCF layer until 1200°C, without change of curvature direction. This was attributed to the thin LSCF layer and to a higher stiffness of the thicker structure, allowing the curvature change point to shift to a high temperature. In the case of severe curvature patterns occurring in the bi-layer structures, the prediction derived from curvatures of bi-layer structures did not match up with the experimental result of the triple-layer structure due to increased stiffness and thickness ratio in the triple-layer structure.
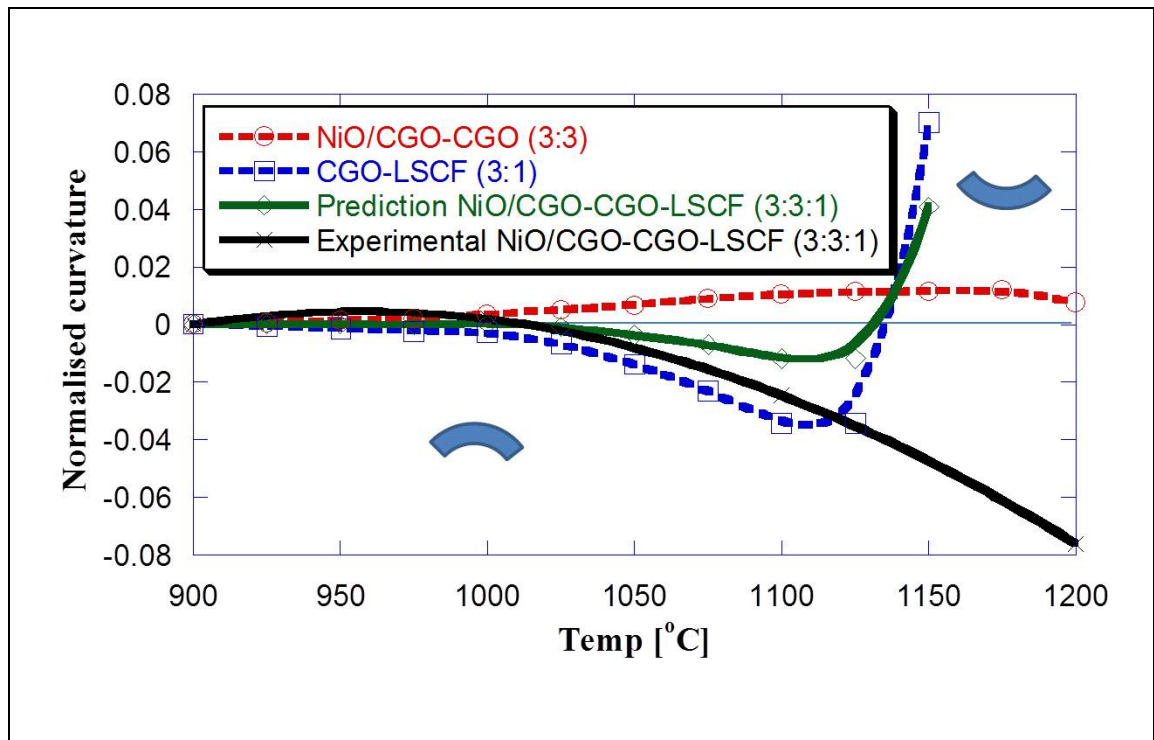

Figure 6.5 Curvature prediction calculated from bi-layer structures and experimental results of the triple-layer structure, consisting of NiO/CGO-CGO-LSCF with 9:3:1 layers

Case V – Thickness ratio (3:1:3)

The curvature evolution of NiO/CGO | CGO | LSCF with 3:1:3 layers is shown in Figure 6.6. Prior to curvature observations of the triple-layer structure, it could be ascertained that the prediction graph for the triple-layer structure would not be available due to severe curving point occurring at 1050°C. Although the opposing curvature direction of the bi-layer structures compensated for each other in the triple-layer structure during co-sintering, the curvature of the triple-layer structure from 1000°C was curved towards the NiO/CGO layer due to the curvature evolution of the CGO-LSCF structure. However, in the experimental result of the triple-layer structure, there was no significant curvature change of the structure, maintaining the curvature towards the LSCF layer until the final temperature. It was attributed to increased stiffness and non-homogenous stress distribution of the CGO layer behaviour interacting with both layers (NiO/CGO and LSCF) during co-sintering [12, 13].

Figure 6.6 Curvature prediction calculated from bi-layer structures and experimental results of the triple-layer structure, consisting of NiO/CGO-CGO-LSCF with 3:1:3 layers

Case VI – Thickness ratio (1:3:9)

In the triple-layer structure with 1:3:9 layers shown in Figure 6.7, the prediction result was in excellent agreement with the experimental observations during co-sintering. The thicker LSCF layer was applied to avoid severe curvature evolution towards the LSCF layer during co-sintering. As a result, the prediction was able to closely follow the experimental result. Regarding the effect of the thickness ratio, the curvature of the triple-layer structure was expected to be curved towards the NiO/CGO layer, corresponding to the prediction calculated from the bi-layer structures. In addition, since the experimental result was well matched to the prediction, moderate stress distribution of the triple-layer structure during co-sintering may have a minimal impact on microstructural deformation during curvature change.   In this experiment, it was attributed that the thin NiO/CGO layer caused the structure to be entirely curved to the LSCF layer. Although the curvature rate between the prediction and the experimental result at 1200°C was slightly divergent, due to shift in motion of the thicker structure, it could still be demonstrated that the curvature behaviour of the prediction was similar to that of the experimental results of the triple-layer structure during co-sintering.
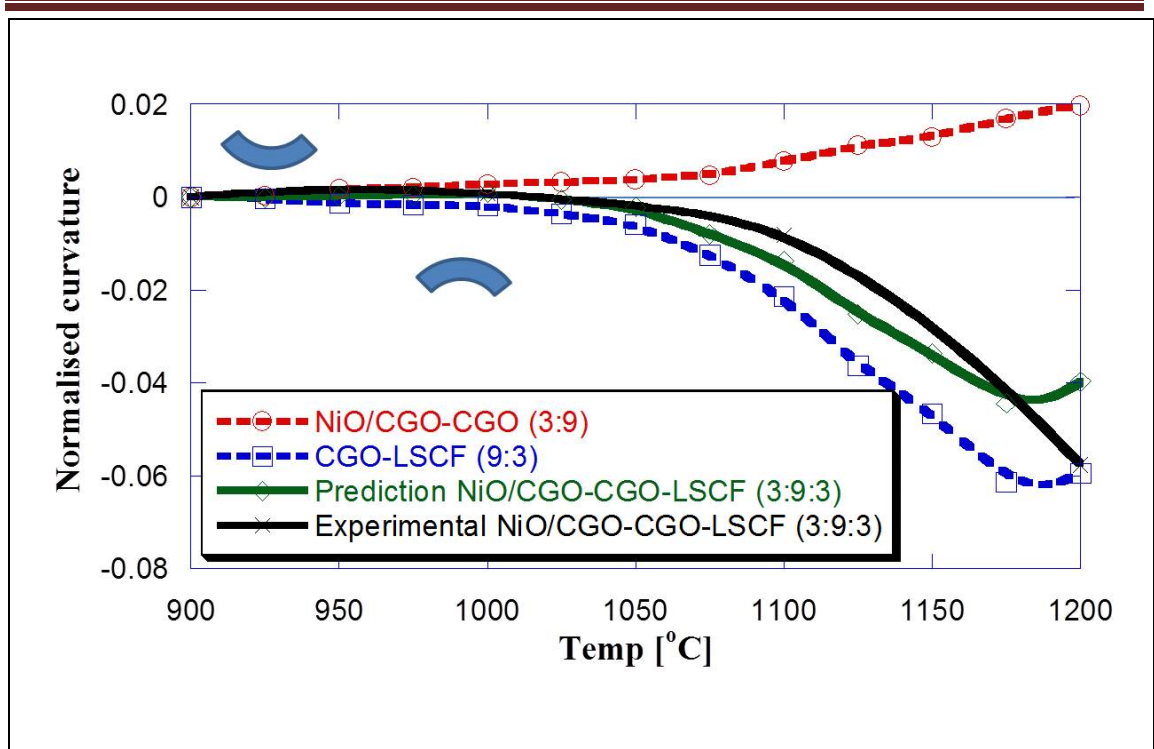
Figure 6.7 Curvature prediction calculated from bi-layer structures and experimental results of the triple-layer structure, consisting of NiO/CGO-CGO-LSCF with 1:3:9 layers

Case VII – Thickness ratio (3:3:9)

Even though there were no severe curvatures of the bi-layer structures due to increased thickness during co-sintering, the experimental result showed different curvature patterns as compared to the prediction of bi-layer structures, as shown in Figure 6.8. Unlike the structure in Figure 6.7, there was no relatively dominant layer of the structure during co-sintering, so curvature did not tend towards any particular layer. Furthermore, enhanced stiffness from the 15 layers used for the structure inhibited extensive curvature. For these reasons, the activity for curvature evolution of the triple-layer structure was weak and did not match up with the prediction.
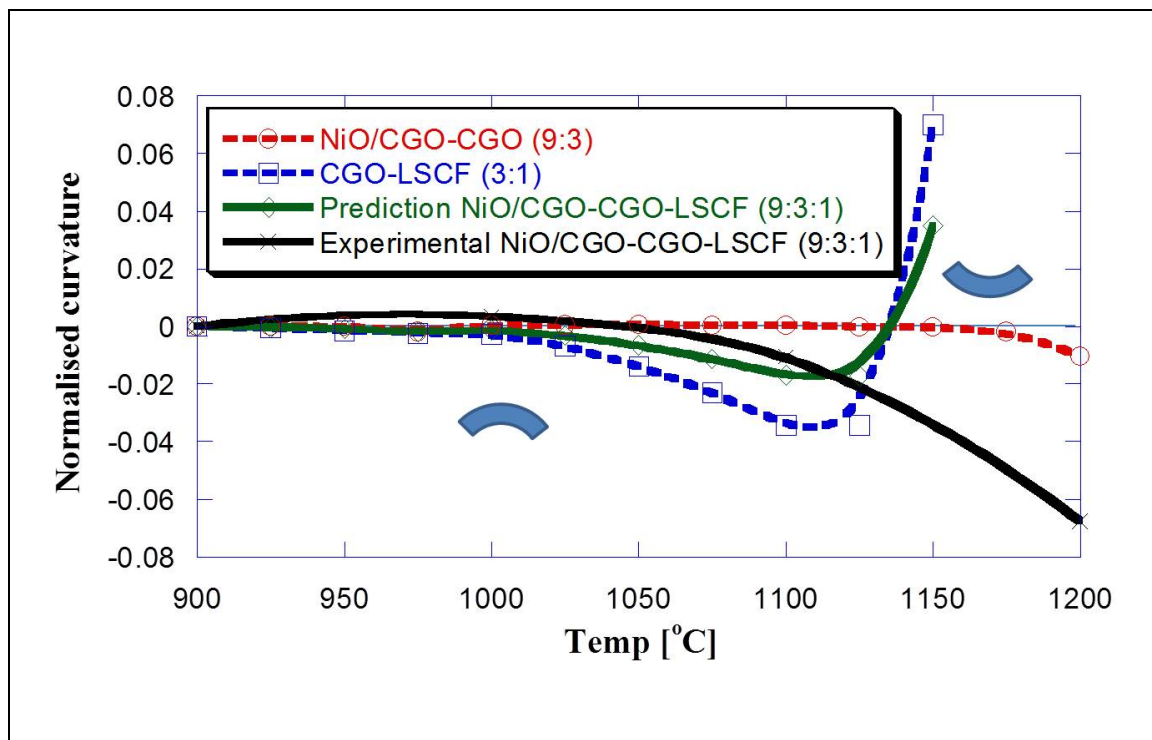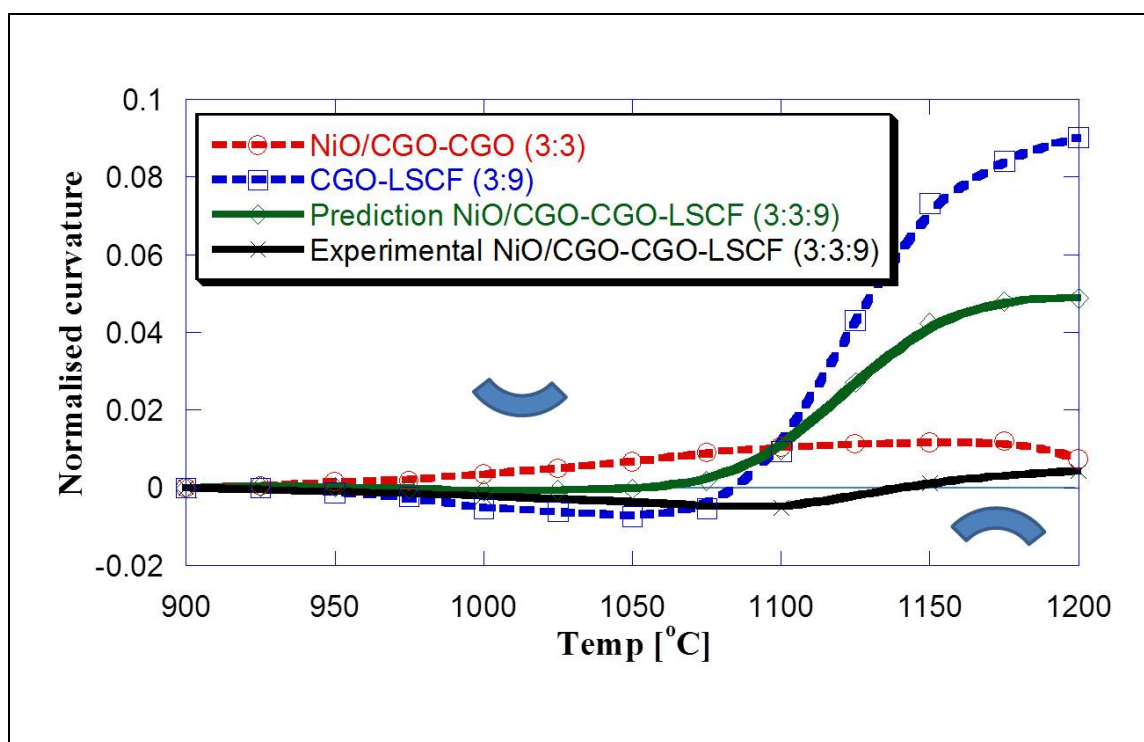

Figure 6.8 Curvature prediction calculated from bi-layer structures and experimental results of the triple-layer structure, consisting of NiO/CGO-CGO-LSCF with 3:3:9 layers

Case VIII – Thickness ratio (9:3:9)

The curvature evolution of NiO/CGO | CGO | LSCF with 9:3:9 layers is shown in Figure 6.9. The structure consisted of 21 layers and was the thickest structure among the samples. The structure was 3 times thicker as compared to the result in Figure 6.6. Due to increased thickness, there was no severe curvature evolution of the prediction from the bi-layer structures during co-sintering. However, the experimental observation of the triple-layer structure was not in agreement with the prediction. The increased thickness of the structure leads the curvature behaviour to be moved to a high temperature. The stresses for curvature evolution in bi-layer structures compensated each other in the triple-layer structure and did not significantly affect the curvature evolution of the structure up to 1200°C.
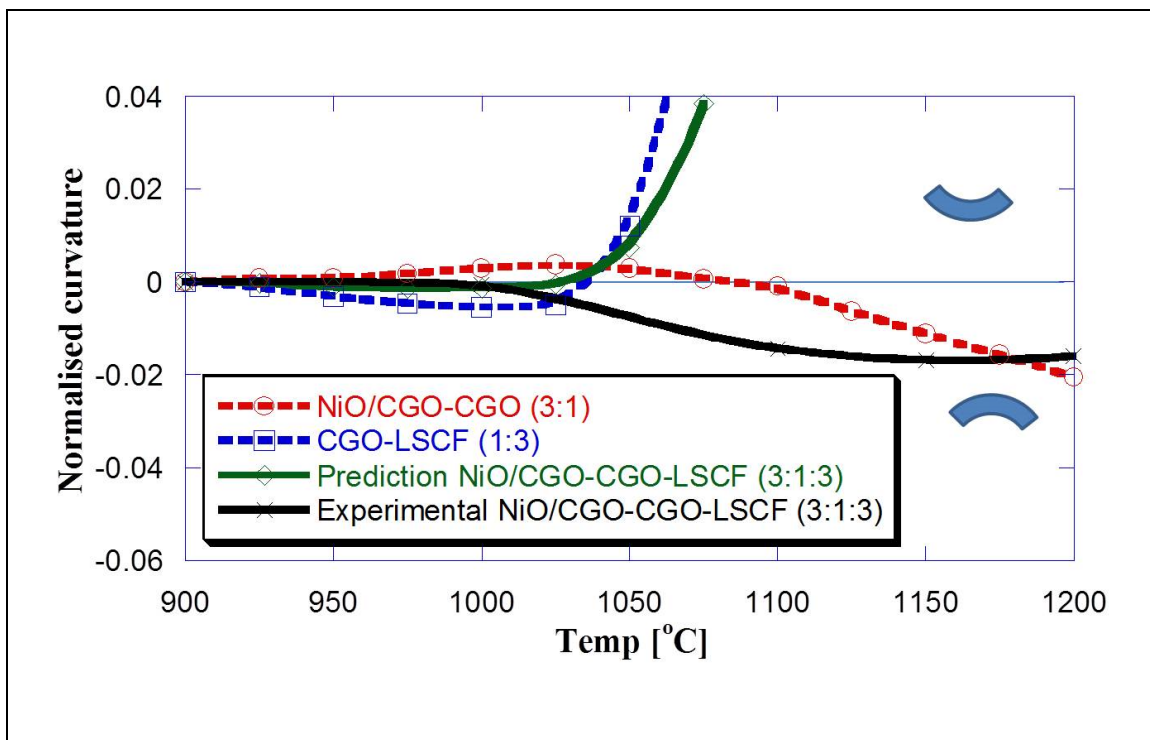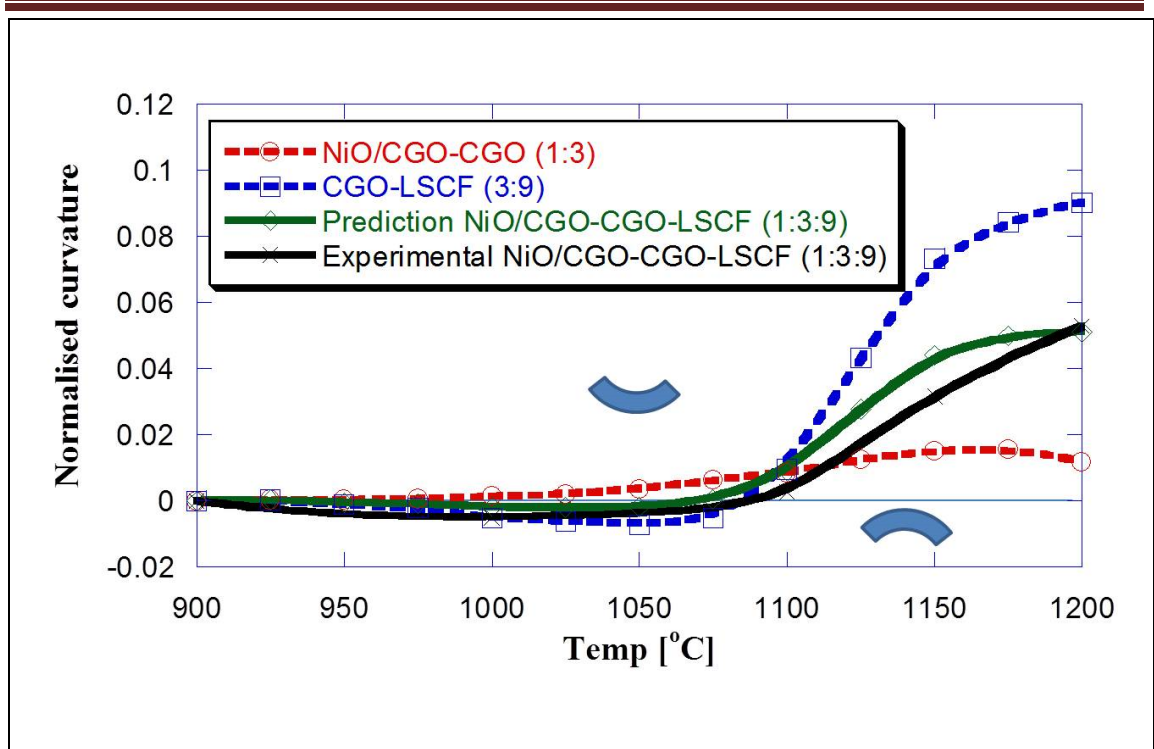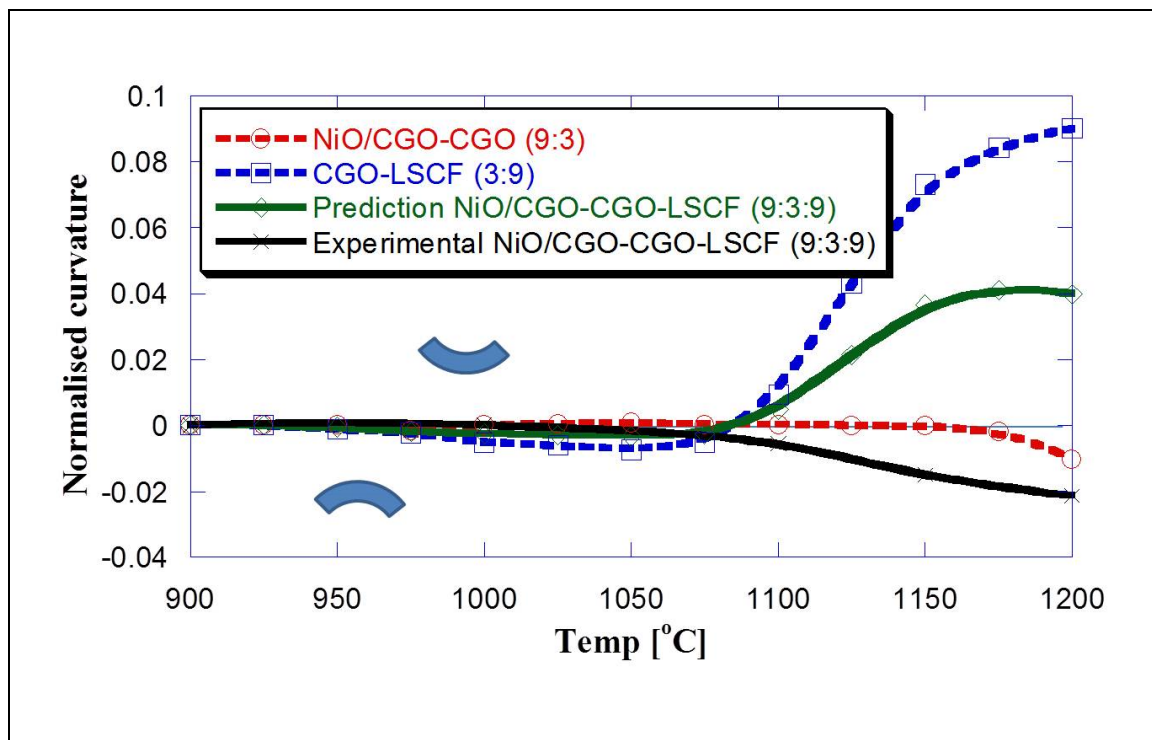

Figure 6.9 Curvature prediction calculated from bi-layer structures and experimental results of the triple-layer structure, consisting of NiO/CGO-CGO-LSCF with 9:3:9 layers

Various curvature behaviours of the triple-layer structures related to thickness (ratio) parameters during co-sintering were investigated through in-situ monitoring of curvature evolutions in bi- and triple-layer structures. Among them, potential structures were decided for a zero-deflection condition. Figure 6.10 shows two curvature graphs corresponding to the prediction, expected to show moderate stress distribution for a minimum of microstructural deformation during co-sintering. In other words, the curvature evolution of the triple-layer structure followed along the curvature prediction calculated by the sum of the curvatures of the bi-layer structures, which leads to a reduction in stress variation of the structures, resulting in elimination of cracking during co-sintering. During the cooling process, the shape of the triple-layer structures could develop curvature towards the LSCF layers, due to the higher thermal expansion coefficient of the LSCF. Among various conditions, the triple-layer structure with 1:3:9 layers (for anode, electrolyte and cathode respectively) was selected for zero-deflection condition in order to fabricate a wavy triple-layer structure during co-sintering. The negative curvature towards LSCF layer was dominant till around 1100°C where the LSCF layer shrank faster than CGO and NiO/CGO. The curvature was then changed to the NiO/CGO layer with increasing temperature due to the overwhelming sintering kinetics of NiO/CGO and CGO. Although there remained curvature evolution towards NiO/CGO layer at the final temperature of the co-sintering process, it could be compensated by higher thermal expansion coefficient of LSCF during the cooling process. This experimental condition was applied to fabricate wavy structures from initially flat structures. On the other hand, the curvature of the structure with 3:9:3 layers was forced to curve towards the LSCF layers at the end of the co-sintering process.
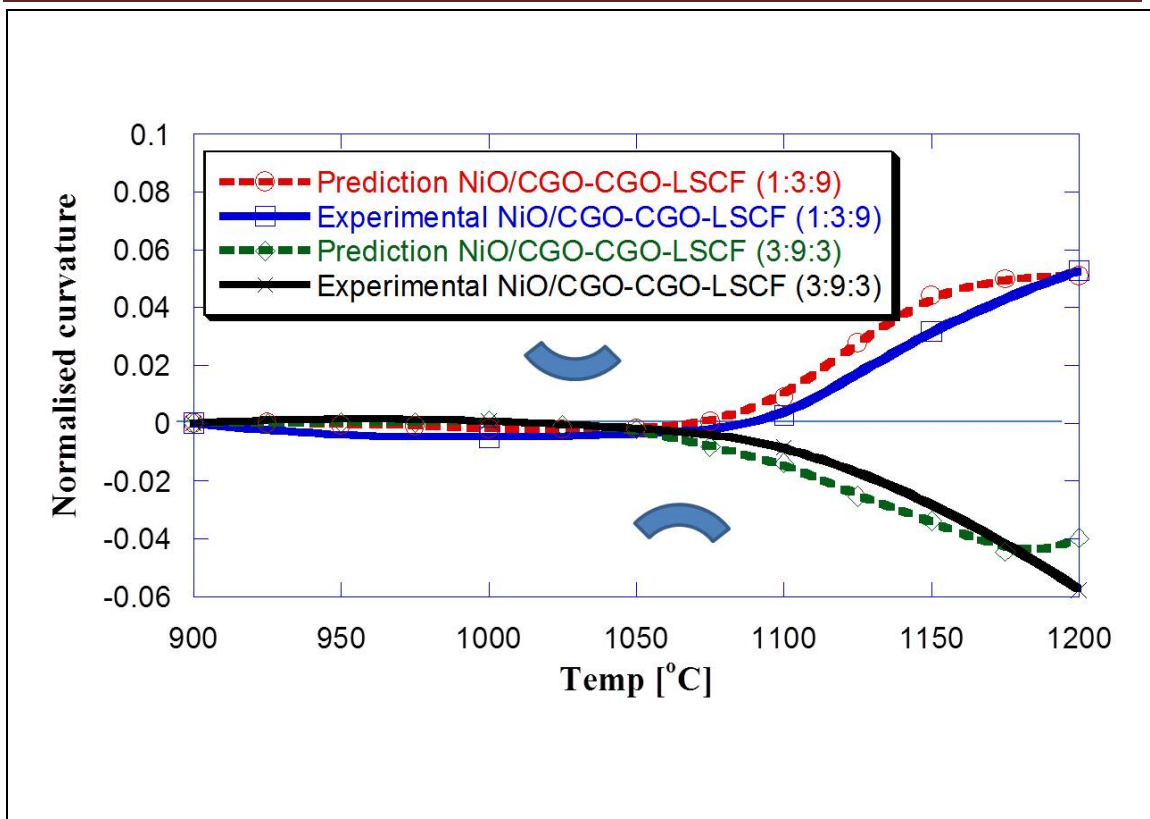
Figure 6.10 Curvature evolutions for zero-deflection of triple-layer structures

XRD analysis was used for confirmation of third phase formation at interfaces of the triple-layer structure during co-sintering, as shown in Figure 6.11. Since the formation of third phase materials increases unidentified impurity that can degrade electrochemical performance and mechanical property, it is necessary to evaluate third phase formation of materials during co-sintering [14, 15]. In-situ XRD analysis could not be applied for the measurement of third phase materials at interfaces in triple-layer structures, due to the limitations of X-ray penetration. Instead, powder mixtures were used to determine if third phase formation between reference materials had occurred during co-sintering. The results were shown as reference materials in Figure 6.11 (a) for anode, (b) for electrolyte, and (c) for cathode. These data were compared to the result of mixture materials shown in Figure 6.11 (d) for reactions at the interface between anode and electrolyte layers, and (e) for reactions at the interface between electrolyte and cathode layers. As the sintering process was carried out in atmospheric conditions, the materials remained as an oxide form after the completion of the process. Compared with reference peaks and mixture peaks, it is demonstrated that the result shows no

existence of third phase formation of materials at interfaces in the triple-layer structure during the co-sintering process. This was attributed to particle size difference between CGO (d_{50}: 0.3 μm) and LSCF (d_{50}:1.0 μm) and co-sintering temperature (less than a temperature for fully dense structures), affecting a smaller portion of the activated grain boundary. This shows that the materials used for the triple-layer structure were stable during the co-sintering process.
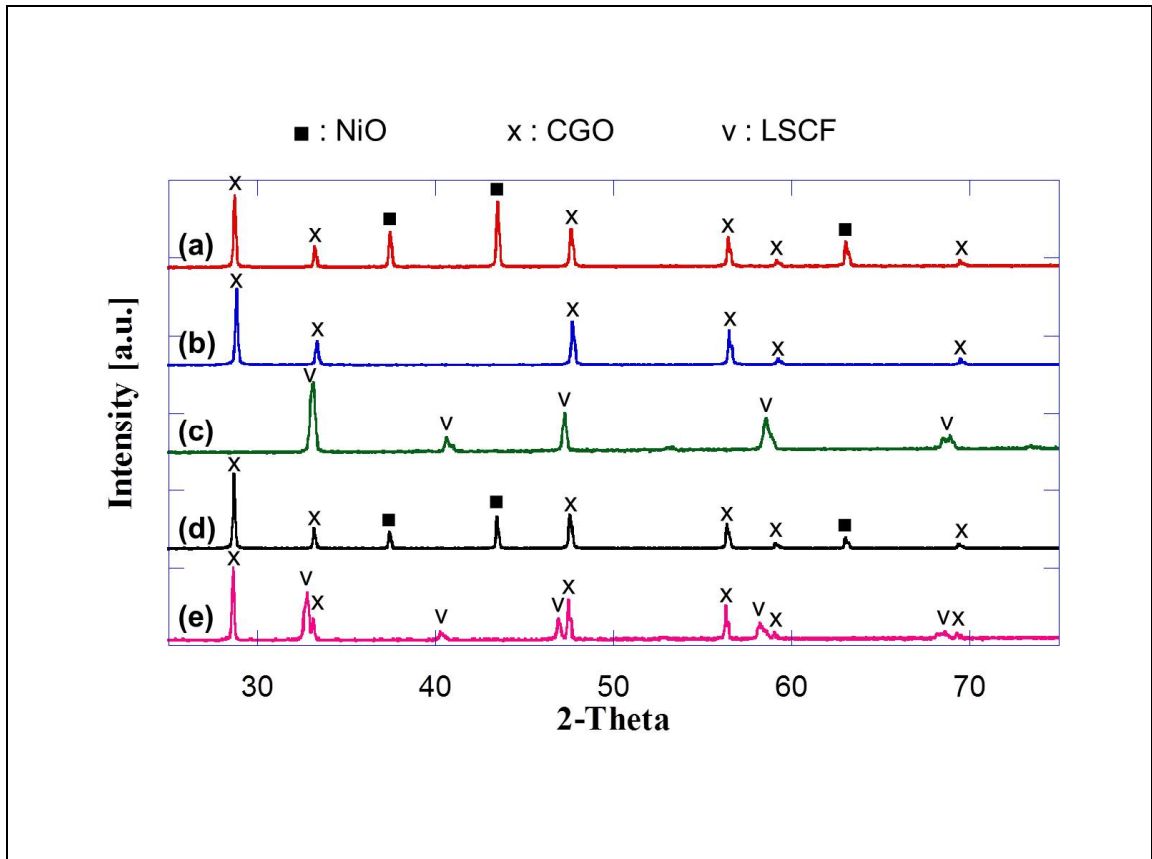
Figure 6.11 XRD results of materials used for the triple-layer structure for (a) NiO/CGO; (b) CGO; (c) LSCF; (d) mixture of NiO/CGO and CGO; and (e) mixture of CGO and LSCF

6.2 Discussion

Curvature Evolution of Triple-layer Structures

During the co-sintering of the triple-layer structures, the layers were rigidly assembled and the mismatch in stresses between layers occurred based on differences in the elastic-viscous material properties including thermal expansion, shrinkage rate and uniaxial viscosity. As discussed in Chapter 5, the curvature behaviour of the triple-layer structures was mainly affected by the behaviour of the electrolyte-cathode bi-layer structure and the presence of a relatively thin layer among three component layers. When comparing curvature evolutions in bi- and triple-layer structures, the curvatures of triple-layer structures were not matched up with the prediction derived from the curvatures of the bi-layer structures. One of the influential factors for this may be the pressure condition for the fabrication of triple-layer structures. Since the same pressure condition was applied to all structures, a relatively higher pressure was applied to the thicker structures, contributing to higher initial density. Li et al. [16] suggest that the higher compaction pressure, the larger the curvature of the sintered structure. In addition, it was noted that the structures compacted under high pressure conditions displayed a bubbling phenomenon, resulting from decreased gaseous diffusivity during binder decomposition. Higher compaction pressure may increase contact probability of particles as well as the stiffness of the structure against macro-deformation during co-sintering [17, 18]. These factors could influence the different shrinkage behaviour of each material in triple-layer structures, contributing to different curvature evolutions during co-sintering. In consideration of the characteristics of the tape-casting layer, non-homogenous particle size distribution in the thickness direction may lead the triple-layer structures to have different curvature developments as increasing temperature [19, 20]. When the tape-casting method was used for a single layer, particle sedimentation during drying could lead the top side of a single layer to have smaller particles than the lower side. This was related to the shrinkage occurring at a slower rate at the top side than at the lower side during sintering. Different sized particle compositions in the thickness direction may affect

mismatch stress distribution for the determination of curvature development during the co-sintering of the triple-layer structure.

Zero-deflection condition during the co-sintering of the triple-layer structure

The shrinkage behaviour of a tape-casting layer is mainly determined by a variety of valuables such as initial density, thickness, particle size and distribution. Once these tape-casting layers are assembled to create a multilayer structure, the shrinkage behaviour of the structure is comprehensive, with the layers affecting each other during co-sintering. In case the shrinkage stress of one layer in a triple-layer structure is significantly greater with respect to the other layers and beyond critical point during co-sintering, the structure may be induced to warp or crack. Through in-situ observation, the curvatures of several structures were monitored and two cases were chosen for a zero-deflection condition. Since both cases were closely matched to the prediction calculated from the average of the bi-layer curvature evolutions, it is possible to consider that the moderate stress distribution in the triple-layer structure occurred during curvature development to inhibit severe defects such as abnormal microstructure and cracking [21]. The in-situ monitoring was only carried out to measure the curvature of the structures up to 1200°C , excepting the cooling process. In order to assure the final shape of the structure at room temperature, these structures should be investigated for curvature change from different thermal expansion coefficients among materials during the cooling process [22]. Since the thermal expansion coefficient of the LSCF is generally known to be higher than that of the other materials, the shrinkage of the cathode layer is expected to increase, followed by a curving towards the LSCF layers. Considering this shrinkage effect in the triple-layer structure during the cooling process, the structure with the 1:3:9 layers appears to be in good agreement with a zero-deflection condition. On the other hand, the structure with the 3:9:3 layers is expected to be curved further towards the LSCF layer, resulting in the accelerated warping of the structure. Regarding the shrinkage process by thermal expansion of the materials, the stiffness of the structure may affect the curvature change. Although a thicker structure is beneficial for

the reduction of curvature evolution due to increased stiffness during the cooling process, it may compromise the structure by facilitating deviant or undesired curvature, as well as cracking, during co-sintering.

Third phase formation at interfaces of the triple-layer structure

During the co-sintering of the triple-layer structure, the XRD result showed that the formation of third phase material had not occurred at the interfaces of the structure. On the basis of the final density of the materials, it could be suggested that the main mechanism that causes bonding is diffusion during co-sintering. In order to produce third phase material, a rearrangement of the material for new connection after disconnection of the existent bonding should be required. This process can easily occur under the condition that the sintering temperature is lower than the melting point of one material among the material components. In case the differences of sintering temperature between materials are larger during the co-sintering process, third phase formation may occur [23]. In this respect, the absence of third phase formation at the interfaces of the triple-layer structure may be attributed to reduced differences of sintering temperatures between materials, resulting from the use of a smaller sized CGO and a coarse particle sized LSCF for the adjustment of their sinterability during the co-sintering process. As the atoms are not compatible in a mixed lattice under the condition that the co-sintering temperature of the triple-layer structures is less than a temperature for third phase formation, it may be difficult to produce third phase material at the interface of the triple-layer structure during the co-sintering process.

6.3 Summary

The triple-layer structures were investigated for curvature evolutions during co-sintering through an in-situ monitoring method. It is emphasised that the process for determination of curvature evolution in triple layer structures incurred greater complications and complexity than for the corresponding bi-layer cases. As the sintering behaviour of CGO layer in the triple-layer structures was influenced by both NiO/CGO and LSCF layers simultaneously, the mechanism to determine curvature evolution in triple-layer structures became more complicated. It can be demonstrated that curvature behaviour, for which thinner layer is dominant for curvature evolution in bi-layer structures, is identical to curvature evolution of triple-layer structures during the co-sintering process. As the stiffness of triple-layer structures against curvature evolution was higher than bi-layer structures, there was no drastic change of curvature evolution during the co-sintering process. From the experimental observations, the prediction of the triple-layer structures was feasible in the condition that there was no severe curvature evolution during the co-sintering process of the bi-layer structures. In addition, the stiffness of the structures should be regarded as one of the influential factors affecting curvature evolution of thicker structures, resulting in retardation of curvature change. It was shown that the thicker the structure, the higher temperature required for the changing point of curvature direction. Some curvature predictions of triple-layer structures calculated from bi-layer structures were not consistent with the experimental observations of the structures. This was due to different conditions such as thickness, stiffness, initial density and microstructural status. Two of the cases showed good agreement between the prediction and the experimental results, regarding stable condition for stress variation occurring by dimensional change from the bi-layer to the triple-layer structure. For fabrication of a zero-deflection structure, the shrinkage behaviour from thermal expansion of materials during the cooling process should be considered. After completing the whole process, the analysis of XRD was carried out to investigate the formation of third phase materials at the interfaces of the triple-layer structure. As there was no confirmed existence of third phase material at the interfaces, the materials used for the triple-layer structure could be considered demonstrably stable and the

suitable candidate materials for the fabrication of a triple-layer structure using the co-sintering process for SC-SOFC applications.

References

[1] OLEVSKY, E., MOLLA, T.T., FRANDSEN, H.L., BJØRK, R., ESPOSITO, V., NI, D.W., ILYINA, A. and PRYDS, N., 2013. Sintering of Multilayered Porous Structures: Part I-Constitutive Models. Journal of the American Ceramic Society, 96(8), pp. 2657-2665.

[2] LIU, X., 2014. Sintering, camber development of layer composites and a new method to eliminate or decrease camber. Bulletin of Materials Science, 37(1), pp. 117-122.

[3] COSTA, R., HAFSAOUI, J., DE OLIVEIRA, ANA PAULA ALMEIDA, GROSJEAN, A., CARUEL, M., CHESNAUD, A. and THOREL, A., 2009. Tape casting of proton conducting ceramic material. Journal of Applied Electrochemistry, 39(4), pp. 485-495.

[4] LARGILLER, G., BOUVARD, D., CARRY, C., GABRIEL, A., MÜLLER, J. and STAAB, T., 2012. Deformation and cracking during sintering of bimaterial components processed from ceramic and metal powder mixes. Part I: Experimental investigation. Mechanics of Materials, 53, pp. 123-131.

[5] YE, G., JU, F., LIN, C., GOPALAN, S., PAL, U. and SECCOMBE, D.A., 2005. Low-cost single step co-firing technique for SOFC manufacturing. SOFC IX, PV, 7, pp. 451-459.

[6] SØRENSEN, B.F., SARRAUTE, S., JØRGENSEN, O. and HORSEWELL, A., 1998. Thermally induced delamination of multilayers. Acta materialia, 46(8), pp. 2603-2615.

[7] LU, J., HNG, H.H., SONG, X., ZHANG, T. and MA, J., 2011. Cosintering of a bimodal pore distribution layered structure: constitutive models and experiments. Journal of the American Ceramic Society, 94(5), pp. 1528-1535.

[8] OLLAGNIER, J., GUILLON, O. and RÖDEL, J., 2010. Constrained sintering of a glass ceramic composite: I. Asymmetric laminate. Journal of the American Ceramic Society, 93(1), pp. 74-81.

[9] MÜLLER, A.C., HERBSTRITT, D. and IVERS-TIFFÉE, E., 2002. Development of a multilayer anode for solid oxide fuel cells. Solid State Ionics, 152, pp. 537-542.

[10] YAN, Z., GUILLON, O., WANG, S., MARTIN, C.L., LEE, C. and BOUVARD, D., 2012. Synchrotron x-ray nano-tomography characterization of the sintering of multilayered systems. Applied Physics Letters, 100(26), pp. 263107.

[11] OLLAGNIER, J., GUILLON, O. and RÖDEL, J., 2007. Effect of anisotropic microstructure on the viscous properties of an LTCC material. Journal of the American Ceramic Society, 90(12), pp. 3846-3851.

[12] HO, S., HILLMAN, C., LANGE, F. and SUO, Z., 1995. Surface cracking in layers under biaxial, residual compressive stress. Journal of the American Ceramic Society, 78(9), pp. 2353-2359.

[13] MOON, H., KANG, D., PARK, H. and HYUN, S., 2011. Stress and camber analysis of anode-supported electrolytes by tape-casting and co-firing techniques. International Journal of Hydrogen Energy, 36(17), pp. 10991-10997.

[14] GUI, Z., WANG, Y. and LI, L., 2004. Study on the interdiffusion in base-metal-electrode MLCCs. Ceramics International, 30(7), pp. 1275-1278.

[15] ZUNIC, M., BRANKOVIC, G., FOSCHINI, C.R., CILENSE, M., LONGO, E. and VARELA, J.A., 2013. Influence of the indium concentration on microstructural and electrical properties of proton conducting $NiO–BaCe_{0.9-x}In_x Y_{0.1}O_{3-\delta}$ cermet anodes for IT-SOFC application. Journal of Alloys and Compounds, 563, pp. 254-260.

[16] LI, W. and LANNUTTI, J.J., 2005. Curvature evolution in LTCC tapes and laminates. Components and Packaging Technologies, IEEE Transactions on, 28(1), pp. 149-156.

[17] MALZBENDER, J., 2010. Curvature and stresses for bi-layer functional ceramic materials. Journal of the European Ceramic Society, 30(16), pp. 3407-3413.

[18] TEOCOLI, F., BRODERSEN, K., FOGHMOES, S.P.V., RAMOUSSE, S. and ESPOSITO, V., 2014. Effects of co-sintering in self-standing CGO/YSZ and CGO/ScYSZ dense bi-layers. Journal of Materials Science, 49(15), pp. 5324-5333.

[19] PARK, H., MOON, H., PARK, S., LEE, J., YOON, D., HYUN, S. and KIM, D., 2010. Performance improvement of anode-supported electrolytes for planar solid oxide fuel cells via a tape-casting/lamination/co-firing technique. Journal of Power Sources, 195(9), pp. 2463-2469.

[20] KULAWIK, J. and SZWAGIERCZAK, D., 2014. Properties of multilayer NTC perovskite thermistors prepared by tape casting, lamination and cofiring. Key Engineering Materials, 605, pp. 507-510.

[21] SØRENSEN, B.F. and HORSEWELL, A., 2001. Crack growth along interfaces in porous ceramic layers. Journal of the American Ceramic Society, 84(9), pp. 2051-2059.

[22] PRIMDAHL, S., SØRENSEN, B.F. and MOGENSEN, M., 2000. Effect of Nickel Oxide/Yttria-Stabilized Zirconia Anode Precursor Sintering Temperature on the Properties of Solid Oxide Fuel Cells. Journal of the American Ceramic Society, 83(3), pp. 489-494.

[23] CHICK, L.A., LIU, J., STEVENSON, J.W., ARMSTRONG, T.R., MCCREADY, D.E., MAUPIN, G.D., COFFEY, G.W. and COYLE, C.A., 1997. Phase Transitions and Transient Liquid-Phase Sintering in Calcium-Substituted Lanthanum Chromite. Journal of the American Ceramic Society, 80(8), pp. 2109-2120.

Chapter 7

Fabrication of a Wavy type Porous Triple-layer SC-SOFC

7.1 Results

Curvature evolution of a Wavy SC-SOFC

A fabrication of wavy type SC-SOFC was carried out utilising the previously suggested co-sintering condition for a zero-deflection structure. Figure 7.1 shows the wavy type SC-SOFC; a planar green triple-layer structure is laid on supporting rods at room temperature, Figure 7.1 (a). The structure could be deformed as pre-curved structures at 80°C, Figure 7.1 (b), by structural flexibility due to binder softening. An optical image of the co-sintered wavy type SC-SOFC is shown in Figure 7.1 (c). This pre-shaped structure was heated up to 1200°C followed by a cooling process rate of 3°C min^{-1}. Although the curvature of the wavy structure evolved during co-sintering as with curvature monitoring of the planar structures, the shape of the structure at the final temperature of co-sintering was confirmed, via experimental observation, to maintain its initial wavy shape. After the cooling process, the final shape of the structure was slightly curved towards the NiO/CGO layer, as shown in Figure 7.1 (c). Compared with curvature evolution in co-sintering of the planar triple-layer structure, different stress distribution near alumina rods in the wavy structure can be mainly attributed to curvature evolution during co-sintering. Especially, the deformation of the structure on the rods during debinding process leaded non-uniformity of micro structural condition at the early of the co-sintering process. In addition, when fabricating the multi-layer structure via the hot pressing method, anisotropy might have been induced into the structure during the process.

Microstructure of layers in the wavy type SC-SOFC was examined using SEM, shown in Figure 7.2. It shows the results of the triple-layer structures; (a) ~ (c) for wavy structure, (d) for planar structure, (e) wavy structure at interface between the anode and the electrolyte layer, and (f) wavy structure at the interface between the electrolyte and the cathode layer. It is shown that all layers have porous structure with %TD of 0.7 and the structure has a 175± 2µm total thickness (16 µm for anode, 37 µm for electrolyte, and 122 µm for cathode). The sintered condition at interfaces indicated that a good connection between layers had been preserved. Figure 7.2 (e) showed that CGO particles in the electrolyte layer was sintered to fusion with the CGO particles of the anode layer, enabling an enhancement of the effective electrochemical reaction area in the anode layer for an electrochemical reaction in the methane-air mixture during operation. In addition, pore size of LSCF is larger than others. As it is well known that sintering temperature of cathode material is lower than that of anode or electrolyte material, LSCF with coarse green particle was used to match the final porosity of each material after co-sintering. Besides, images are evidently showing the similarity between two cells' microstructure in general, like average component thicknesses, average porosities etc. Interestingly, there are small level of differences in microstructure of wavy cell, i.e. anode layer thickness and anode porosities between Figure 7.2 (a) ~ (c), where images were taken from the convex area, flat area and concave area respectively. These subtle differences were generated during the co-sintering process (anode layer was compressed in Figure 7.2 (a) whilst the same layer was under tensile stress in (c)), and so can contribute to the local variation of gas flow and fuel to oxygen ratios.
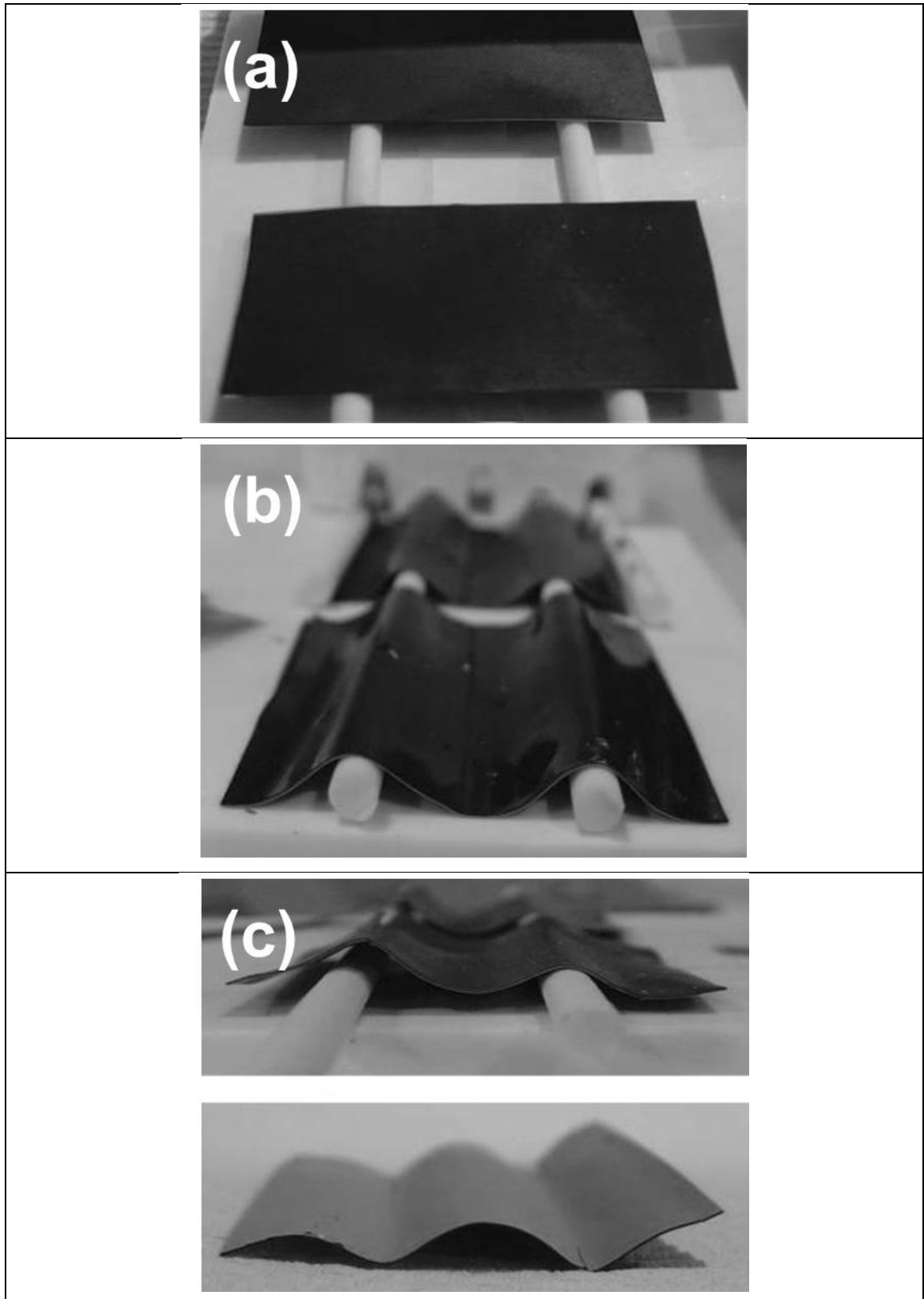
Figure 7.1 Wavy SC-SOFC images; (a) at room temperature before the co-sintering process, (b) at 80°C during co-sintering, and (c) at room temperature after the co-sintering process
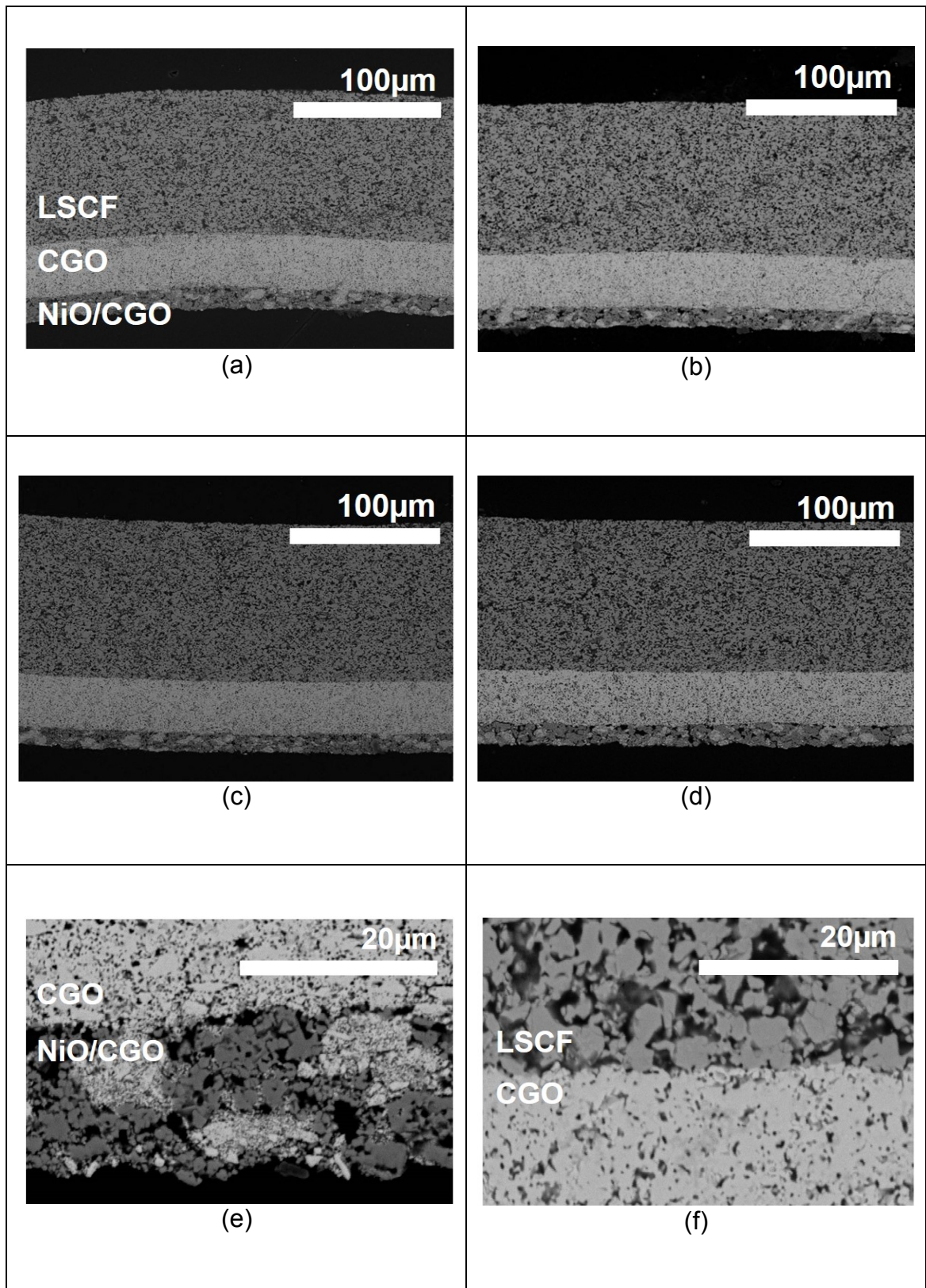
Figure 7.2 Cross-sectional image of wavy SC-SOFC; (a) ~ (c) for the wavy structure, (d) for the planar structure, and (e, f) for SEM images of wavy structure at the interfaces

Performance Test

The polarisation curve was investigated at 600°C, shown in Figure 7.3. The OCV and maximum power density of the wavy SC-SOFC were measured as 0.39 V and 9.7 mW cm^{-2} under the condition of methane-air mixture (CH$_4$:O$_2$ = 1:1), whereas the planar SC-SOFC generated 0.15V and 1.8mW cm^{-2}. It is well known that performance of SC-SOFC is sensitive to the operational conditions, particularly to temperature and to the fuel to air ratio, and considering that, performance of the planar SC-SOFC seems reasonable [1-3]. The 2.6 times higher OCV and the 5.4 times higher maximum power density from the wavy SC-SOFC over the planar SC-SOFC were apparently attributed that the wavy cell has 7.1% higher effective cell area for a given area defined by the cell perimeter (geometric projected area). In addition, the performance difference can be explained that the cell shapes influenced gas flow through the wavy cell. A wavy shape could lead to an increase in gas flow, enhancing the effective gas diffusion.
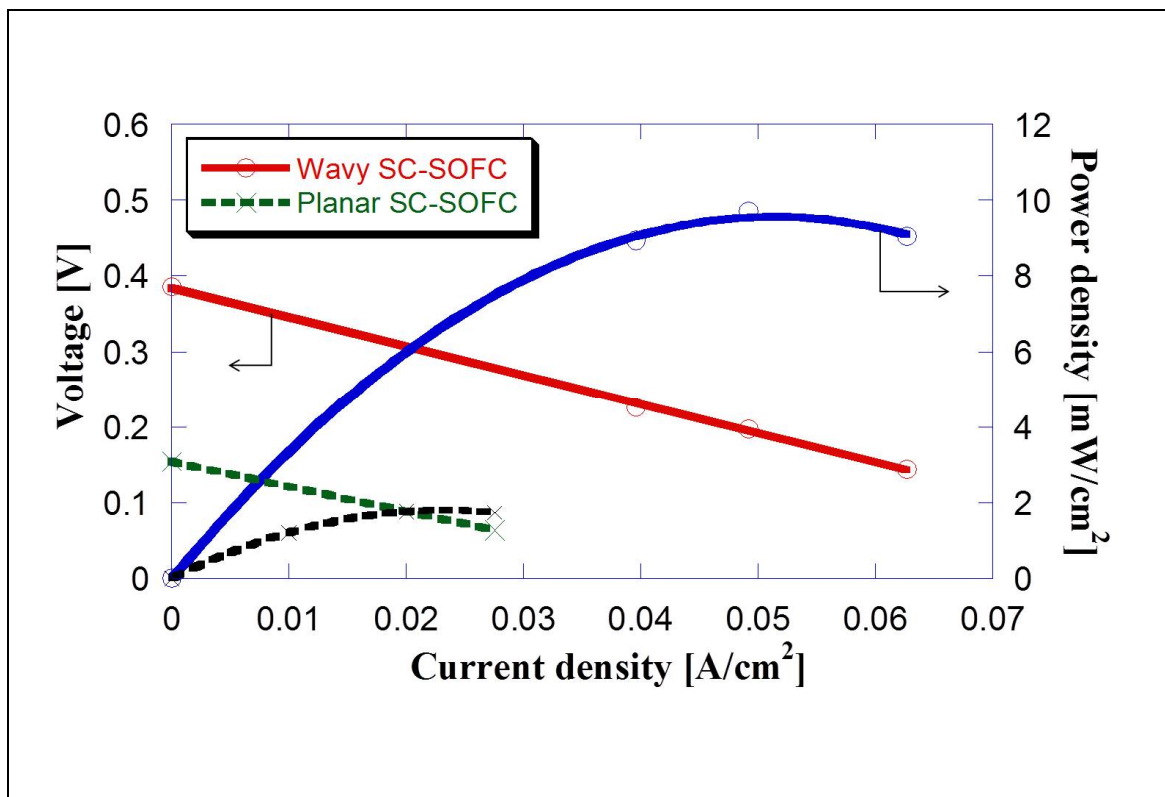
Figure 7.3 Performance comparisons with the wavy and planar cell

Some researchers have investigated the local transport characteristics inside curved SOFCs, such as the gas concentration distribution, the over potential distribution, and the current density distribution, showing a different pattern with that of a planar SOFC [4-6]. This was attributed to the cell shapes influencing gas flow. It is suggested that a wavy shape could lead to an increase in gas flow, enhancing the effective gas diffusion. The vortex of the gas flow from wavy shape may increase transportation rate between the reactant and product gases, delivering increased utilisation rate of TPBs. Thereby enhanced transportation rate of gases due to different microscopic structures at the interfaces of the wavy cell may help provide higher performance. Furthermore, compared to the planar cells, the wavy cell should have different pore shape, orientation and interconnectivity influenced by the induced stress developed on each component during co-sintering, particularly at around the point of centraflexure where stress concentration could have occurred to elevate such microstructural differences. The level of influence caused by different microstructure to the higher performance output is being investigated further to identify the inter-relationships between microstructure and performance.

Table 7.1 shows various results of SC-SOFCs depending on parameters such as materials used, temperature, gas flow rate, and structural property. The parameters affecting cell performance are examined further under the discussion section. Although the performance of the wavy cell was higher than that of the planar cell in this study, the performance of both cells were relatively low value compared to the data of other references. To verify the reliability of the performance test for future study, the chamber diameter of test rig, greater than sample size, should be reduced to increase fuel utilisation during cell operation. In addition, as this fabrication process was aimed to make a wavy stack cell as a flow-through type SC-SOFC, a cell housing for a wavy SC-SOFC stack should be needed to prevent gas flow from bypassing the structure.

Table 7.1 Properties of SC-SOFCs

	Ref. [1]	Ref. [2]	Ref. [7]	this study
Anode	NiO/CGO	NiO/CGO	NiO/CGO	NiO/CGO
Electrolyte	CGO	CGO	CGO	CGO
Cathode	CGO-LSCF	CGO-LSCF	CGO-BSCF	LSCF
Operation temp. [°C]	625 - 675	600	625	600
Gas ratio of methane to oxygen	0.67 – 2.0	2.0	1.0	1.0
Gas flow rate [lpm]	0.5	0.5	0.1	0.6
Electrolyte porosity	Dense	Dense	Porous	Porous
Max. Power density [mW/cm^2]	7.5 ~ 17	260	7	9.7

7.2 Discussion

Fabrication of the wavy triple-layer structure via co-sintering

The curvature evolution of a planar triple-layer structure for wavy dimension during a co-sintering process was demonstrated in Chapter 6. In order to fabricate a wavy triple-layer structure, the temperature was firstly increased to 80°C, which was then maintained for 1 hour to utilise the material's flexibility to form a wavy shape during debinding. As the softening of the binder increased assembling force at the interfaces of the structure, there was no delamination during this process [8-11]. The pre-shaped wavy structure has retained its shape till the completion of the co-sintering process, since the zero-deflection condition suggested in previously chapter has been applied.

Influential factors for the determination of the OCV

The OCV of SC-SOFCs is subject to many experimental conditions, such as used materials, fuel to oxygen ratio, total flow, microstructure and operating temperature for partial oxidation of methane [12, 13]. The authors of the quoted references concluded that the geometry configurations led to very different performance parameters of the cells (OCV and power density) as a function of fuel to oxygen ratio and total flow, most likely because they produce different gas compositions at the electrodes. The conclusion supports our OCV differences. In their study, the demonstrated OCV showed a range of output from 0.35V to 0.75V as the gas flow rate changes. Besides, the cell orientation to the gas flow (either parallel or perpendicular) influences the local gas flow within the cell, and that influences the OCV as well; which was attributed to different oxygen partial pressure and turbulence that increases mixing of the gases on both sides of the cell. Likewise, the gas flow condition on the wavy cell is different from that of the planar cell, contributing to the variable OCV even tested under the same gas flow condition. It has been stated that the OCV difference is subjected to the permeability of porous electrolyte which gases diffuse through during operation, so that lower oxygen partial pressure from

oxygen consumption at the cathode side leads to a decrease in the OCV [14]. Given the reason, a porous electrolyte layer allows local gas flow changes that may result the changes in OCV as the flow and the reverse flow of mixture (product gases and reactants) are allowed between the two electrodes throughout the electrolyte layer; as this varies the local oxygen partial pressure. After completing electrochemical reaction on the wavy cell, different partial pressure of each H_2 and O_2 will lead to development of variable flow rates depend on the locations, followed by variation of gas residual time to electrodes. Since the OCV is defined as the ratio of partial pressure of oxygen at the cathode to that at the anode, OCV is therefore decreased due to reduced oxygen partial pressure on the cathode side [15, 16]. Also, the locally variable flow rate will incline to a development locally variable fuel to oxygen ratios, contributing to the different level of OCV. Furthermore, the exothermic reaction on the anode gave rise to temperature increment of anode that will accelerate the level of variation to fuel flow rates and to gas mixing ratios throughout the cell. These variable factors are brought up as the gas mixture flow rate changes to turbulence from laminate flow. Therefore, these behaviours and local condition accelerate turbulence flow affecting electrochemical reaction on the wavy cell, compared to the planar cell.

In addition, it is noticed that the OCV of SC-SOFCs particularly depends on the microstructure [13]. During the co-sintering process, sintering induced stresses are maximised at the interfaces [2, 17,18]. Such stresses are elevated even to a higher level in the wavy cells than in the planar cells, due to the geometry, hence higher level of influence to the wavy cell microstructure, so the OCV differences can be further explained. With the advantage of turbulence flow, this causes improved mass and diffusional transport, result in the increase of the fuel utilisation in the wavy cell. Also, changing the arrangement of the connecting particles within the porous media during the co-sintering process could provide different flow resistance. In summary, the wavy cell's higher OCV over the planar cell's OCV is explained due to the possible changes of local fuel to oxygen ratios, local flow rate, and microstructure on the interfaces.

Furthermore, enlarged cell area with wavy shape leaded different temperature gradient and locally mixture ratio along the cell length, contributing to cathode activity towards methane oxidation and heat contribution.

Experimentally, the area of current collector mesh covered on the electrodes of planar cell was significantly larger than that of the wavy cell, so it decreased the effective electrochemical reaction area.

Porous electrolyte

As SC-SOFCs are fundamentally operated based on the different catalytic selectivity of the anode and the cathode layers in a gas mixture condition, each layer should be active only for electrochemical reaction in various gas compositions. Ideally, the anode layer should be more active for partial oxidation of methane gas and electro-catalytic reaction with hydrogen, while the cathode layer should be active for electro-catalytic reaction with oxygen. During this process, gas compositions in a SC-SOFC with a porous electrolyte structure may cause unstable electrochemical reactions at both sides. Sun et al. [19] demonstrated that a cell with a dense electrolyte layer showed higher performance than one with a porous electrolyte layer under the same conditions. This was attributed to unstable gas compositions resulting from the gas diffusion of hydrogen and carbon monoxide, which were transported from the anode to the cathode through the porous electrolyte, after the partial oxidation of methane gas in the presence of the Ni catalyst.

Reduction of NiO

Prior to the cell test, a NiO reduction process should be carried out to activate catalytic reaction in the anode layer. In the case of a conventional SOFC, the reduction process is achieved under the mixture of hydrogen and nitrogen [20, 21]. As the whole structure is exposed to the same atmosphere in SC-SOFC, the cathode layer can be affected by the reducing gas, resulting in degradation of the cell. Alternatively, the mixture of methane and nitrogen could be applied for reduction of NiO in SC-SOFCs [22, 23]. However, during the process with use of methane, carbon deposition from methane cracking may occur in the anode layer, contributing to degradation of the cell. As the sintering temperature for the wavy SC-SOFC was lower than the point for dense

structure, the structure had porous layers with low stiffness. It was shown that the strength of the cell could be vulnerable to additional stress leading to cracks propagating through the structure. To eliminate negative effects during the reduction process, Rembelski et al. [24] suggested a two-step reduction process. By changing the gas condition before carbon deposition occurs, the NiO reduction process can be completed without the aforementioned issues.

Volume shrinkage of the anode layer during NiO reduction is one of the negative effects and relates to cell performance and mechanical stability. It is known that a circa 40% volume reduction occurs during the process from NiO to Ni particles in the anode layer. This may induce extra curvature evolution and local tensile stress to the electrolyte and cathode layers, leading to cracking in the structure [25]. In addition, the rearrangement of Ni particles may cause microstructural damage of the anode layer, contributing to the degradation of the cell [26, 27].

In the reduction process of a wavy triple-layer structure without a current collector grid, partial cracking was occasionally identified due to low stiffness induced by volume shrinkage of the anode layer. In the case where the current collector was coated on both sides of the structure, cracking did not occur during the reduction process. The grid of the current collector may lead to increased mechanical strength of the structure.

Thickness of the anode and cathode layers

In order to meet the requirement for a zero-deflection condition during the co-sintering process, a thin anode layer was applied in the fabrication of the wavy SC-SOFC. It is known that the thickness of the anode layer plays a significant role for cell stability under the gas mixture condition, and several hundred micrometres should be required to maintain a reasonably stable condition [28]. This is because a thin anode layer is very sensitive to the presence of oxygen under a single chamber condition. In the condition, the thin anode layer can be easily reoxidised with significant microstructure damage contributing to irreversible cell degradation. In the case of the cathode layer, a relatively thicker cathode layer was applied for the wavy SC-SOFC. It is noted

that an increase in cathode thickness causes a rapid decrease of cell performance resulting from the increase of the cathode ohmic resistance, the temperature drop at the cathode side from endothermic reaction and an increase in the difficulty of gas diffusion contributing to mass transport losses.

7.3 Summary

The structure investigated using a planar triple-structure for zero-deflection condition was applied to fabricate a wavy shape structure during co-sintering. At 80°C, a planar structure laid on supporting rods could be deformed into a wavy structure due to binder softening leading to structural flexibility. During the co-sintering of the wavy triple-layer structure, curvature behaviour was similar to that of the planar structure. Through in-situ monitoring, the final shape of the structure was validated to conform to a wavy shape at 1200°C. After finishing the whole fabrication process, the structure maintained its initial wavy shape, having curved slightly towards the anode layer due to different thermal expansion coefficients between layers. SEM images showed that the sintered wavy structure had three porous layers and each was well adjoined throughout the two interfaces.

During the reduction process of the wavy SC-SOFC, the grid of the current collector helps the structure to enhance mechanical strength against volume shrinkage. In the performance comparison between wavy and planar structures, it was shown that the power density of the wavy structure was higher than that of the planar structure. This was attributed to an increase of the effective electrochemical reaction sites from the curved dimension for a given chamber diameter. The ratio of materials in the wavy triple-layer structure should be modified to increase cell performance and stability. The use of a flow through design necessitating electrolyte porosity, in combination with a thin anode layer and a thick cathode layer, has enforced penalties such as accelerated irreversible degradation, and a low probability of the useful electrochemical reactions under a mixed gas environment. Given these drawbacks, it is suggested that an anode supported wavy type SC-SOFC would enhance microstructural stability under redox conditions, and mitigate irreversible degradation of the cell.

References

[1] REMBELSKI, D., VIRICELLE, J., COMBEMALE, L. and RIEU, M., 2012. Characterization and Comparison of Different Cathode Materials for SC-SOFC: LSM, BSCF, SSC, and LSCF. Fuel Cells, 12(2), pp. 256-264.

[2] SUN, L., RIEU, M., VIRICELLE, J., PIJOLAT, C. and ZHAO, H., 2014. Fabrication and characterization of anode-supported single chamber solid oxide fuel cell based on La0.6 Sr0.4 Co0.2 Fe0.8 O3− δ – Ce0.9 Gd0.1 O1.95 composite cathode. International Journal of Hydrogen Energy, 39(2), pp. 1014-1022.

[3] HWANG, J., CHEN, C. and LAI, D., 2005. Computational analysis of species transport and electrochemical characteristics of a MOLB-type SOFC. Journal of Power Sources, 140(2), pp. 235-242.

[4] STYGAR, M., BRYLEWSKI, T. and RĘKAS, M., 2012. Effects of changes in MOLB-type SOFC cell geometry on temperature distribution and heat transfer rate in interconnects. International Journal of Heat and Mass Transfer, 55(15–16), pp. 4421-4426.

[5] RAMIREZ-MINGUELA, J. and RANGEL-HERNANDEZ, V., Numerical analysis in a MOLB-type SOFC considering different operating conditions. Dynamics, 2(2), pp. 2.

[6] YAKABE, H., OGIWARA, T., HISHINUMA, M. and YASUDA, I., 2001. 3-D model calculation for planar SOFC. Journal of Power Sources, 102(1–2), pp. 144-154.

[7] GUO, Y., BESSAA, M., AGUADO, S., STEIL, M.C., REMBELSKI, D., RIEU, M., VIRICELLE, J., BENAMEUR, N., GUIZARD, C. and TARDIVAT, C., 2013. An all porous solid oxide fuel cell (SOFC): a bridging technology between dual and single chamber SOFCs. Energy & Environmental Science, 6(7), pp. 2119-2123.

[8] BÖHNLEIN-MAUß, J., SIGMUND, W., WEGNER, G., MEYER, W.H., HEßEL, F., SEITZ, K. and ROOSEN, A., 1992. The function of polymers in the tape casting of alumina. Advanced Materials, 4(2), pp. 73-81.

[9] GEFFROY, P., CHARTIER, T. and SILVAIN, J., 2007. Preparation by tape casting and hot pressing of copper carbon composites films. Journal of the European Ceramic Society, 27(1), pp. 291-299.

[10] FENG, J., FAN, Y., QI, H. and XU, N., 2007. Co-sintering synthesis of tubular bi-layer α-alumina membrane. Journal of Membrane Science, 288(1), pp. 20-27.

[11] HILLMAN, C., SUO, Z. and LANGE, F.F., 1996. Cracking of laminates subjected to biaxial tensile stresses. Journal of the American Ceramic Society, 79(8), pp. 2127-2133.

[12] STEFAN, I.C., JACOBSON, C.P., VISCO, S.J. and DE JONGHE, L.C., 2004. Single chamber fuel cells: Flow geometry, rate, and composition considerations. *Electrochemical and solid-state letters,* **7**(7), pp. A198-A200.

[13] BUERGLER, B.E., GRUNDY, A.N. and GAUCKLER, L.J., 2006. Thermodynamic equilibrium of single-chamber SOFC relevant methane–air mixtures. *Journal of the Electrochemical Society,* **153**(7), pp. A1378-A1385.

[14] SUZUKI, T., JASINSKI, P., PETROVSKY, V., ANDERSON, H.U. and DOGAN, F., 2005. Performance of a porous electrolyte in single-chamber SOFCs. *Journal of the Electrochemical Society,* **152**(3), pp. A527-A531.

[15] AKHTAR, N., DECENT, S., LOGHIN, D. and KENDALL, K., 2009. Mixed-reactant, micro-tubular solid oxide fuel cells: An experimental study. Journal of Power Sources, 193(1), pp. 39-48.

[16] AKHTAR, N. and KENDALL, K., 2011. Micro-tubular, solid oxide fuel cell stack operated under single-chamber conditions. International Journal of Hydrogen Energy, 36(20), pp. 13083-13088.

[17] ATKINSON, A., KIM, J., RUDKIN, R., TAUB, S. and WANG, X., 2011. Stress induced by constrained sintering of 3YSZ films measured by substrate creep. *Journal of the American Ceramic Society,* **94**(3), pp. 717-724.

[18] KIM, J., RUDKIN, R.A., WANG, X. and ATKINSON, A., 2011. Constrained sintering kinetics of 3YSZ films. *Journal of the European Ceramic Society,* **31**(13), pp. 2231-2239.

[19] WANG, X., KIM, J. and ATKINSON, A., 2012. Constrained sintering of 8mol% Y 2 O 3 stabilised zirconia films. *Journal of the European Ceramic Society,* **32**(16), pp. 4121-4128.

[20] DRESCHER, I., LEHNERT, W. and MEUSINGER, J., 1998. Structural properties of SOFC anodes and reactivity. Electrochimica Acta, 43(19), pp. 3059-3068.

[21] RADOVIC, M. and LARA-CURZIO, E., 2004. Elastic Properties of Nickel-Based Anodes for Solid Oxide Fuel Cells as a Function of the Fraction of Reduced NiO. Journal of the American Ceramic Society, 87(12), pp. 2242-2246.

[22] ZHANG, C., ZHENG, Y., RAN, R., SHAO, Z., JIN, W., XU, N. and AHN, J., 2008. Initialization of a methane-fueled single-chamber solid-oxide fuel cell with NiO SDC anode and BSCF SDC cathode. Journal of Power Sources, 179(2), pp. 640-648.

[23] MOREL, B., ROBERGE, R., SAVOIE, S., NAPPORN, T. and MEUNIER, M., 2007. Catalytic activity and performance of LSM cathode materials in single chamber SOFC. Applied Catalysis A: General, 323, pp. 181-187.

[24] REMBELSKI, D., RIEU, M., COMBEMALE, L. and VIRICELLE, J., 2013. In situ reduction and evaluation of anode supported single chamber solid oxide fuel cells. Journal of Power Sources, 242, pp. 811-816.

[25] FAES, A., FRANDSEN, H.L., GOLDSTEIN, D.R., PIHLATIE, M. and KAISER, A., 2010. Curvature and strength of Ni-YSZ solid oxide half-cells after redox treatments. Journal of Fuel Cell Science and Technology, 7(5), pp. 051011.

[26] BUERGLER, B., OCHSNER, M., VUILLEMIN, S. and GAUCKLER, L., 2007. From macro-to micro-single chamber solid oxide fuel cells. Journal of Power Sources, 171(2), pp. 310-320.

[27] KLEMENSØ, T., APPEL, C. and MOGENSEN, M., 2006. In situ observations of microstructural changes in SOFC anodes during redox cycling. Electrochemical and solid-state letters, 9(9), pp. A403-A407.

[28] WANG, Z., LÜ, Z., CHEN, K., WEI, B., ZHU, X., HUANG, X. and SU, W., 2013. Redox Tolerance of Thin and Thick Ni/YSZ Anodes of Electrolyte-Supported Single-Chamber Solid Oxide Fuel Cells under Methane Oxidation Conditions. Fuel Cells, 13(6), pp. 1109-1115.

Chapter 8

Conclusions and Future Works

8.1 Wavy type porous SC-SOFC

It has been suggested that a wavy type SC-SOFC can cope with the performance and stability issues, as the cell will naturally form increased effective electrochemical reaction area in order to enhance its overall efficiency. The advantages of the wavy cell are: mechanical robustness derived from the shape which can absorb a level of shock, and (ii) improvement of the active cell area contributing to higher performance, compared with planar type SC-SOFCs under the same operation condition. Furthermore, as the cell design is of a porous structure with the gases flowing through, the cell has more potential reaction sites for a given projected area.

The study of the fabrication of a wavy SC-SOFC was investigated via curvature monitoring of bi-layer and triple-layer structures during the co-sintering process. The in-situ monitoring allowed the researcher to discern remarkable differences of the curvature evolution in the response to dimensional conditions such as thicknesses and thickness ratios. The curvature evolution of the structures was significantly influenced by the in-plane stresses derived from the shrinkage behaviour of each component, indicating different densification mechanisms during the co-sintering of the multilayer structure. As the in-plane stress in the interface of electrolyte and cathode layer was much higher than that of anode and electrolyte layer, the dimensional condition of electrolyte and cathode layer was a dominant function to decide the final curvature of the triple-layer structure during co-sintering. In order to form a wavy shape from the planar structure, a zero-deflection condition was chosen at the final sintering temperature. The planar triple-layer structure on the supporting rods could be changed into a wavy shape during debinding process, and the curvature evolution of wavy structure during co-sintering was consistent

with a zero-deflection structure at final temperature. The dimensional condition for the zero-deflection structure was successfully applied to the fabrication of a wavy SC-SOFC and the performance was compared to the planar SC-SOFC under the condition of the same diameter chamber. The conclusions obtained are further elaborated in the succeeding sub chapters.

1) Sintering behaviour of a tape-casting layer

For the development of a wavy SC-SOFC operating at 600°C, materials were selected as NiO/CGO for anode, CGO for electrolyte and LSCF for cathode. Free and vertical sintering processes of each tape-casted material were carried out up to 1200°C with in-situ shrinkage measurement. The results showed that the shrinkage behaviour of the structure in the vertical sintering was significantly reduced compared to the free sintering, and this was due to the effect of the materials' own weight/gravitational force. The cathode with coarse particles helped to retard the sintering process, so as to balance the final density of each material. The density range of 61%TD ~ 64%TD was calculated as a final density of each material by the shrinkage analysis of free sintering and this was in good agreement with the results of the SEM analysis and the Archimedes method. Uniaxial viscosities were measured by a difference in shrinkage rate between free and vertical sintering in order to investigate the sintering behaviour of each material during the densification process. The viscosity of the CGO layer at a specific density was measured to be slightly higher than that of the NiO/CGO layer, resulting from the fact that NiO particles inhibited the sintering process of the CGO particles during sintering. As the cathode material with coarse particles had lower sinterability than the material with smaller particles at the same temperature, the viscosity of the cathode material with coarse particles was shown to be lower than that of the anode and electrolyte layers at the same temperature.

2) In-situ monitoring of curvature evolution during co-sintering

The curvature evolution of bi- and triple-layer structures was investigated as functions of total thickness and thickness ratios by in-situ monitoring during co-sintering. The difference in uniaxial viscosity of the constituent layers, as well as the stiffness of the overall structure, acted as the main factors for influencing curvature evolution of the structure. The curvature patterns of the bi-layer structures with the same thickness ratio were slightly different as compared to Cai's model, and the results showed the curvature behaviour of the thicker bi-layer structure had shifted to a higher temperature. This was attributed to different shrinkage behaviour of each layer in the thicker structures, as well as an increase in stiffness against curvature evolution. In the condition of same total thickness with different thickness ratios, it was observed that the shrinkage of the thinner layer played a significant role in deciding the curvature evolution of the structures. Similar trends were noted in curvature monitoring of the triple-layer structures, but the interactions occurring between layers was of greater complexity, resulting in curvature evolution during co-sintering. The electrolyte layer in particular was influenced by the shrinkage behaviour of the anode and cathode layers at the same time during co-sintering. In the cases without severe curvature evolution, the curvature evolution of the triple-layer structure could be feasibly predicted based on bi-layer curvature patterns, showing good agreement between the prediction and the experimental observation. In order to detect the presence of third phase formations during the co-sintering process, XRD analysis was performed and confirmed that there was no third phase material during co-sintering.

3) Discrepancy between theoretical and experimental curvature rate

The theoretical model used for curvature predictions of bi-layer structures was a function of thickness ratio, viscosity ratio, and strain rate difference. As discussed in Chapter 5, the difference of strain rate between layers in the structure acted as a critical factor to differentiate curvature behaviours. This result implies that the balance of strain rate in materials leads to reduce undesired curvature behaviours of a multi-layer structure during co-

sintering. Therefore, the properties of materials which have different sintering behaviours at the same temperature should be modified by adjusting initial particle size and green density. In case of a thin layer leading severe curvature developments of bi-layer structures, strain rate should be reduced by the use of large particle size or high initial density to maintain the same thickness. Thereby, the effect of a thin layer during the co-sintering of bi-layer structures can be mitigated for elimination of undesired curvatures. As proven through experimental observations, the use of thicker layer helps to reduce mismatched stresses at the interface, leading to decrease curvatures during co-sintering.

Although the trend of curvature rate between theoretical and experimental research was similar, there were some discrepancies. It was attributed to factors such as residual stress, especially for the thin layer, the effect of gravity, and stiffness. These factors were not considered in the theoretical model. These should be further investigated to validate the use of theoretical model for the prediction of curvature evolution during co-sintering.

4) Fabrication and evaluation of a wavy SC-SOFC

The study has investigated the fabrication process of a higher output wavy type SC-SOFCs, using a triple layer structure, based on a careful study of the co-sintering fabrication process. The performance of these fuel cells has been compared with that of a planar SC-SOFC. The different shrinkage behaviour between layers during co-sintering results in curvature evolution in the multi-layer structure. This evolution was monitored experimentally using an optical method. This in-situ monitoring of curvature evolution of bi-layer structures enabled the authors to predict the curvature of a triple-layer structure during co-sintering with the aim of fabricating zero-deflection structure and this was verified by experimental results. Utilising the outcome from the optical observation study, wavy and planar SC-SOFCs are fabricated via single and co-sintering process. As far as the authors are aware the work presented here is the only successful demonstration of fabricating a wavy SC-SOFC via a single sintering process. During the co-sintering process, it was shown that the wavy type SC-SOFC was well-fabricated without severe warping after the co-

sintering process. In addition, this study successfully addresses the prediction of the macro-scale response of wavy cells and shows curvature prediction of a triple-layer structure is feasible based on the bi-layer curvature results. In the comparison for performance, the OCV and maximum power density of the wavy SC-SOFC were 0.39V and 9.7 mW cm^{-2} at 600°C, 2.6 times higher OCV and 5.4 times higher maximum power density than the planar SC-SOFC. The wavy dimension influences the increase of the effective cell area in the unit diameter, and enhances the effective gas diffusion paths that both are contributing to higher performance over the planar type cell. It is believed that the higher output is also attributed by the different microstructure of components caused by the induced stress during co-sintering. The higher output of wavy SC-SOFC over planar SC-SOFCs is well agreed with literature results reported, and the comparison of performance shows that curvature of SC-SOFC can significantly influence the output, and so it is expected that different curvature, probably with an even higher effective cell area for a given projected area, may deliver even higher output over the samples used in this study.

8.2 Recommendations for Future Work

The curvature evolution of the bi- and triple-layer structures during co-sintering was investigated by in-situ monitoring and by comparison to the theoretical model. A clear difference was observed and these results were utilised to suggest a fabrication method for a wavy SC-SOFC. It would be interesting to apply this technique to investigate novel designs of SOFCs with a curved shape and curvature evolution derived from differences in thermal behaviour between layers of the cell. There are issues to be investigated further, as below.

Prediction of curvature evolutions

Each factor in the theoretical model should be modified to match curvature observations measured experimentally. When mismatched stresses occur at the interfaces of a multi-layer structure during co-sintering, it should be considered how each factor was affected and changed by the stresses. In addition, the effect of stiffness and gravity that is contributing to curvature evolution during co-sintering should be reflected in the model.

Properties of fabricated wavy structures

Although in-situ monitoring of macro-scale deformation is available for deciding the final curvature shape, micro-scale structural analysis during co-sintering is not clearly investigated in this study. After the co-sintering of the wavy type SC-SOFCs, the characteristics of the structures should be closely examined. As the structures are fully porous, the condition of pores is very important resulting from the status of particles during sintering, thereby influencing the gas flow path and mechanical strength and contributing to electrochemical reactions of the cell. An interesting progression of research would be an extension of the study on gas flow behaviour at the curved surface for increasing electrochemical activity, which would have practical implications on the novel design of curved SOFCs.

Advanced test rig for validation of the cell performance

The performance comparison between the planar and wavy cell should be investigated in the condition with advanced test rig. As mentioned previously, the chamber size may have been larger than ideal, giving rise to the situation where mixture gases might not fully participate in the electrochemical reaction through the cells. To increase fuel utilisation during operation, it is necessary to match the chamber cross section closely to the cell planar size. Alternatively, the development of cell housing should be undertaken to fix the cell with gas inlet line. As the fabrication process of the wavy cell was initially aimed for the use of flow-through type stacks, the development of bespoke wavy cell housing (along with matching interconnectors) should be investigated further.